

POLITECNICO DI TORINO

Department of Mechanical and Aerospace Engineering
Class LM-33 (DM270)

Master's Degree Thesis
in Automotive Engineering

Additive Manufacturing for Automotive Applications: The Case Study of Tesla®'s Model 3 Dual Motor Rear Subframe



Supervisors

Prof. ELEONORA ATZENI
Prof. ALESSANDRO SALMI

Candidate

EUGENIO GIOACCHINI

Academic Year 2021 - 2022

Acknowledgments

As with any effort that results in the production of a thesis, on the cover there should not only be my name, but also the names of all those who provided assistance, support, encouragement and guidance, who have given me so much of their time and without whom I would not have succeeded.

There are so many people I would like to thank. Firstly, I want to thank my supervisors at Politecnico di Torino, Prof. Eleonora Atzeni and Prof. Alessandro Salmi for their tireless help and support throughout this project.

I must thank everyone who stood by me for all this time, in particular my beautiful parents, Daniela and Roberto, that gave me endless support, love and encouragement, I owe them everything. I also want to thank every single member of my family, my grandparents, cousins, aunts and uncles for always making me feel loved and special.

I want to thank two people that supported me and gave me immense strength. Maria, my only one, and Giulio, my brother from another mother. I love you more than words can say and more than you can imagine.

I must thank all my friends, without whom I would not be the person I am today. Aharon, Alessandro C., Alessandro S., Anna, Daniele, Edoardo, Filippo, Francesco C., Francesco D. M., George, Giammarco, Marco, Martina, Mattia, Michelangelo, Michele, Nicola M., Nicola T., Pier Paolo, Tonino and Vittorio. You really don't know how grateful I am to have met you.

My beautiful partners in crime Valentina, Lorenzo and Andrea. I love you and I wish you all the best in life.

My "mesci" Lorenzo, Rocco and Gregorio, my first Turin family.

My counselors Elisa, Gaia, Anna Laura, Alice Z. and Alice F.

All my outstanding teammates at Squadra Corse PoliTo that gave me the opportunity to race with the best car I could have possibly imagined, I'm sure the future will be bright for every one of you guys.

Finally, I want to thank and dedicate this final project to my beloved Nonna Palmina and my beautiful Zia Pamela since without them my life would not be so unique and special.

I feel blessed to have met such beautiful people and pure souls in my life.

Forever yours,

Eugenio

*"Let us be grateful for the people that make us happy;
they are the charming gardeners who make our souls blossom."*

Abstract

During last decades, Additive Manufacturing has established in the industrial context as a key enabling technology for industries of tomorrow. Automotive companies have already implemented this technology in some strategic departments in order to exploit its high potential for future applications.

The proposed study is aiming to provide design, feasibility and static analyses of a specific structural automotive component, that is the Tesla®'s Model 3 Dual Motor rear subframe built with Additive Manufacturing technologies.

The component will be developed in Siemens® NX environment and exported in Altair® Inspire software. The analysis will be focused on the identification for suitable materials and enabling technologies, on the design optimization and on the behaviour of the component under operative conditions using FEM analyses for the design validation.

Once each component made up of different materials has been successfully validated, a specific material will be selected (SS 316L in this case) and the printing simulation will be considered. At the end of this step, a new static validation will be performed in order to assess the thermal and mechanical stresses experienced by the part in the final manufacturing stage.

As a final consideration, a cost breakdown analysis and a comparison between traditional and AM processes will be presented, taking into account the main differences between each process and between different materials used in the additive technology.

Table of Contents

List of Figures	5
List of Tables	8
1. Additive Manufacturing (AM)	9
1.1 AM Materials	12
1.2 AM Technologies & Costs	15
2. Design for Additive Manufacturing (DfAM)	23
2.1 Generative Design & Topology Optimization.....	26
2.2 Part Consolidation.....	28
3. AM for Automotive Applications & Examples	29
4. Component Selection	37
5. Load Cases	44
5.1 Maximum Acceleration	44
5.2 Braking in Capsize Limits	46
5.3 Sharp Cornering	48
5.4 Passage Over a Road Bump	50
6. Topology Optimization	51
7. FEM Analysis & Results	64
8. AM Machine Choice & Building Process	78
9. Cost Evaluation	85
10. Discussion	90
Bibliography	95

List of Figures

Figure 1. AM Historical Development.....	9
Figure 2. Steps of Digital Fabrication.....	10
Figure 3. Direct Slicing vs. Adaptive Slicing.....	11
Figure 4. Transition Temperatures (Amorphous vs. Semi-crystalline).....	12
Figure 5. Polymers Mechanical Performances.....	13
Figure 6. Metal Powder Defects.....	14
Figure 7. Process Classification for Polymers.....	15
Figure 8. SLA Process.....	16
Figure 9. DLP Process.....	16
Figure 10. FDM Process & Feeding System.....	17
Figure 11. SLS Process.....	17
Figure 12. L-PBF Process.....	18
Figure 13. EBM Process.....	19
Figure 14. DED Process.....	20
Figure 15. AM Costs & Gains Comparison.....	22
Figure 16. Angled & Downward-facing Structures.....	24
Figure 17. Horizontal Holes.....	24
Figure 18. Cross-Section Orientation with respect to Re-Coater Blade Motion.....	25
Figure 19. DfAM Guidelines for SLS.....	25
Figure 20. BMW® i8 Roadster 3D-printed Roof Bracket.....	32
Figure 21. Porsche® GT2 RS 3D-printed Pistons.....	32
Figure 22. Porsche® Taycan 3D-printed Electric Drive Housing.....	33
Figure 23. Bugatti® Chiron 3D-printed Brake Caliper.....	33
Figure 24. Bugatti® Chiron Pur Sport 3D-printed Exhaust.....	34
Figure 25. Toyota® LQ 3D-printed Outer Mirror.....	34
Figure 26. Stellantis® 3D-printed Wheel Carrier.....	35
Figure 27. Fraunhofer® IPT 3D-printed Door Hinge.....	35
Figure 28. F1 Car 3D-printed Front Wing (Scalmalloy).....	36
Figure 29. Alpine® F1 Team 3D-printed Heat Accumulator.....	36
Figure 30. Double Wishbone Strut vs. Multi-link Strut.....	37
Figure 31. Rear Suspension Assembly (Top View).....	38
Figure 32. Rear Suspension Assembly (Front View).....	38
Figure 33. Tesla® Model 3 Chassis US8424960 ^[19]	39
Figure 34. Rear Subframe Technical Drawing (Top View).....	40
Figure 35. Rear Subframe Technical Drawing (Front View).....	40
Figure 36. Rear Subframe Technical Drawing (Lateral View).....	40
Figure 37. Tesla® Model 3 Rear Subframe (Top View).....	41
Figure 38. Tesla® Model 3 Rear Subframe (Isometric View).....	41
Figure 39. Vehicle Lateral Free-Body Diagram.....	44
Figure 40. Vehicle Rear Free-Body Diagram.....	48
Figure 41. Rear Axle Free Body Diagram.....	50
Figure 42. Rear Subframe 3D CAD Model on Altair® inspire.....	51
Figure 43. Partition Areas in the Design Space.....	52
Figure 44. Constraints Locations.....	52

Figure 45. Connectors between Flanges	53
Figure 46. Force Distribution for the Acceleration/Deceleration Load Cases	54
Figure 47. Force Distribution for the Left & Right Sharp Cornering Load Case.....	55
Figure 48. Final Load Scenario (All Load Cases Combined)	55
Figure 49. Subframe Design Space with Applied Loads.....	57
Figure 50. Rear Subframe Topology Optimization with SS 316L (Front View).....	57
Figure 51. Rear Subframe Topology Optimization with SS 316L (Top View).....	58
Figure 52. Rear Subframe Topology Optimization with SS 316L (Bottom View)	58
Figure 53. PolyNURBS Curve with SS 316L (Front View)	59
Figure 54. PolyNURBS Curve with SS 316L (Bottom View).....	59
Figure 55. Detail of the Optimized Part with SS 316L (Top Side)	60
Figure 56. Detail of the Optimized Part with SS 316L (Bottom Side)	60
Figure 57. Rear Subframe Topology Optimization with Ti6Al4V (Front View).....	61
Figure 58. Rear Subframe Topology Optimization with Ti6Al4V (Top View).....	61
Figure 59. Rear Subframe Topology Optimization with Ti6Al4V (Bottom View)	62
Figure 60. PolyNURBS Curve with Ti6Al4V (Front View)	62
Figure 61. PolyNURBS Curve with Ti6Al4V (Bottom View).....	63
Figure 62. Detail of the Optimized Part with Ti6Al4V (Top Side)	63
Figure 63. Von Mises Stress for the Result Envelope (Original Component)	64
Figure 64. Original Result Envelope Von Mises Stress (Top Scale 50 MPa).....	65
Figure 65. Safety Factor Distribution (Original Component).....	65
Figure 66. Displacements Distribution for the Result Envelope (Original Component) ..	66
Figure 67. Displacement Direction in the Original Component (Magnified Scale).....	66
Figure 68. Original Result Envelope Displacements (Top Scale $3.901 \cdot 10^{-2}$ mm)	67
Figure 69. Von Mises Stress Distribution with SS 316L (Optimized Component)	69
Figure 70. Von Mises Stress Distribution with SS 316L (Top Scale 50 MPa).....	70
Figure 71. Safety Factor Distribution with SS 316L (Optimized Component)	70
Figure 72. Displacement Distribution with SS 316L (Optimized Component).....	71
Figure 73. Displacement Direction with SS 316L (Magnified Scale).....	71
Figure 74. Displacement Distribution with SS 316L (Top Scale $3.883 \cdot 10^{-1}$ mm).....	72
Figure 75. Von Mises Stress Distribution with Ti6Al4V (Optimized Component)	73
Figure 76. Von Mises Stress Distribution with Ti6Al4V (Top Scale 50 MPa)	74
Figure 77. Safety Factor Distribution with Ti6Al4V (Optimized Component).....	74
Figure 78. Displacement Distribution with Ti6Al4V (Optimized Component).....	75
Figure 79. Displacement Direction with Ti6Al4V (Magnified Scale).....	75
Figure 80. Displacement Distribution with Ti6Al4V (Top Scale $1.810 \cdot 10^{-1}$ mm).....	76
Figure 81. Laser XLINE 2000R Configuration (by General Electrics®).....	78
Figure 82. Lateral Subframe Section Selected for 3D Printing.....	79
Figure 83. AM Machine Setting in Altair®.....	80
Figure 84. Part Positioning Inside the 3D Printer	80
Figure 85. Component Orientation Optimization.....	81
Figure 86. Light Support Structures for the Lateral Sections.....	81
Figure 87. Von Mises Stresses in L-PBF (Lateral Section Right Side)	82
Figure 88. Von Mises Stresses in L-PBF (Lateral Section Left Side).....	82
Figure 89. Displacements in L-PBF (Lateral Section Right Side).....	83

Figure 90. Displacements in L-PBF (Lateral Section Left Side) 83
Figure 91. Cost Comparison (Forming vs. L-PBF) 88
Figure 92. Tesla®'s Model 3 Dual Motor Weight Distribution 92
Figure 93. Energy Cost Variation (2016 - 2022)^[21] 93
Figure 94. WTT & TTW Emissions 94

List of Tables

<i>Table 1. EOS® M400-4 Cost & Specifications</i>	21
<i>Table 2. Arcam® Q20 Plus Cost & Specifications</i>	21
<i>Table 3. OPTOMECH® LENS 850-R Cost & Specifications</i>	21
<i>Table 4. AISI 1025 Chemical Composition</i>	42
<i>Table 5. AISI 1025 Mechanical Properties</i>	42
<i>Table 6. SS 316L Chemical Composition</i>	42
<i>Table 7. SS 316L Mechanical Properties</i>	43
<i>Table 8. Ti6Al4V Chemical Composition</i>	56
<i>Table 9. Ti6Al4V Mechanical Properties</i>	56
<i>Table 10. FEM Analysis Results (Original Component)</i>	67
<i>Table 11. FEM Analysis Results with SS 316L (Optimized Component)</i>	72
<i>Table 12. FEM Analysis Results with Ti6Al4V (Optimized Component)</i>	76
<i>Table 13. Laser XLINE 2000R Features</i>	78
<i>Table 14. Optimized Parts Cost Comparison for each Material</i>	87
<i>Table 15. Forming vs. L-PBF Process</i>	88

1. Additive Manufacturing (AM)

Additive Manufacturing (AM) is an innovative layer-by-layer production technology that allows to build a specific product or component directly by adding material where it is needed, without melting or subtracting it from an initial rough shape. In particular, AM can be considered as the dual of subtractive manufacturing and it allows to provide near net shapes that improve the material utilization by decreasing the scrap material rate and speeding up the production process.

The basic concept of AM is that a model, initially generated using a three-dimensional Computer Aided Design (3D CAD) system, can be directly fabricated without the need for specific tools. This specific feature allows to highly decrease the production time since once the part is ready to be printed, it can be directly sent to the 3D printing software that immediately starts the building process. Moreover, since there is no need for specific tools to be built, it is possible to carry out the process in few hours and to decrease the initial investment costs with respect to traditional processes.

In its early stages, AM was mainly exploited for rapid prototyping (RP) purposes, since it allowed to rapidly produce cheap conceptual, functional and technical prototypes that were mainly used for testing operations. Starting from early 2000s, AM has also been implemented for rapid tooling, casting and pre-series (RT, RC and RM) productions, but still far from high-volume applications. Nowadays, the technology is also used for end-usable products.

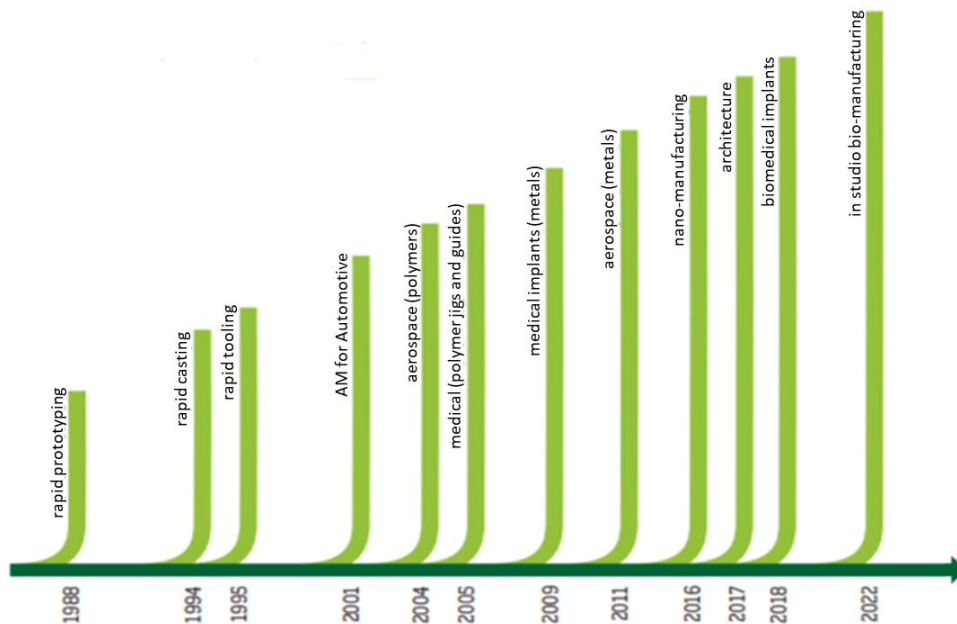


Figure 1. AM Historical Development

Although AM will not replace conventional production methods, it is still expected to revolutionize many areas following an exponential growth, also because this specific technology will make it possible to overcome typical constraints common for traditional processes, allowing the designers to achieve higher operational freedom and to obtain more complex shapes.

The main flowchart to follow when dealing with additive technologies is made up of several steps that are carried out in specific digital environments. First of all the part is designed in a 3D CAD environment and, once the designer is satisfied with the final outcome, it is subjected to a process called polygonization where a mesh is created and a tessellated model is obtained (STL file). After these operations are completed, the file is sent to the AM machine software where part orientation, support generation and slicing are performed. The final step is made directly in the AM machine, where the parts are progressively made layer-by-layer. At the end of the process the resulting parts are then subjected to post-processing operations such as cleaning, support removal and finishing.

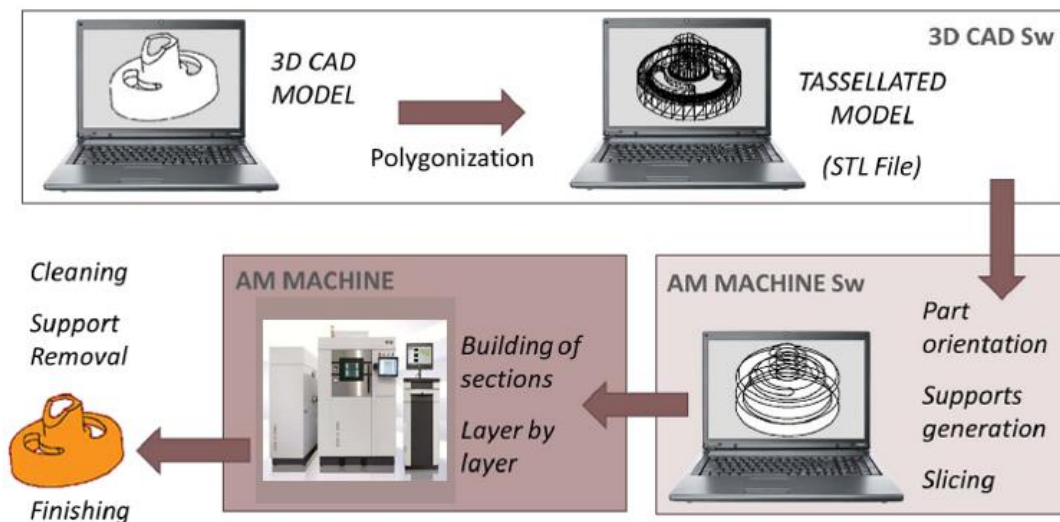


Figure 2. Steps of Digital Fabrication

When dealing with the STL file, it is fundamental to make sure that the model fully describes the part external geometry and features. The defined format has become a specific standard for AM technology and, nowadays, nearly all the printing machines are able to accept the format (that is obtained by every 3D CAD system). The STL format uses triangularization in order to describe the surface to be built by means of triangles.

Once the correct file is sent to the AM machine software, it is very important to consider all the possible part orientations. In particular, when dealing with part orientation, it is very important to consider the part's end-use scenario since layers should be manufactured following the load direction in order to improve its response to mechanical stresses, even if a trade-off between improvements in mechanical performances and building time should be considered.

Another important factor to take into account is related to supports, that also depends on part orientation. Generally, supports are calculated and added to the part by the system software and they can be made using the same material as the part or different materials. These structures are then mechanically removed or dissolved away depending on the used material. In order to decrease the scrap material rate, supports can be provided by hollow structures.

Their location is also important since it influences the amount of post-processing operations that have to be performed and the final surface finishing. Another important role assigned to supports is to provide a thermal sink function since, depending on their disposition, they are able to transfer heat more or less efficiently from the newly built layer to the platform, influencing the magnitude of residual stresses in the part due to the high building chamber temperatures.

The final operation performed by the AM machine software is called slicing and it is performed once the previous two steps are completed. In this specific phase, the STL model of the part to be built is sliced by a series of parallel planes each one at a distance Δs from the other. The higher the distance between planes and the higher the slice thickness. Generally, for simple shapes, the value of Δs remains constant throughout the whole part (direct slicing), while for more complex shapes, the value of Δs is adjusted according to the geometry (adaptive slicing). It is very important to properly set the thickness of each layer since it directly influences the final part quality, in particular the slicing operation introduces in the part surface a stair-stepping trend that can be more or less evident depending on the layer thickness. As can be expected, the lower the layer thickness, the more accurate the final part shape and the longer the building time and vice-versa.

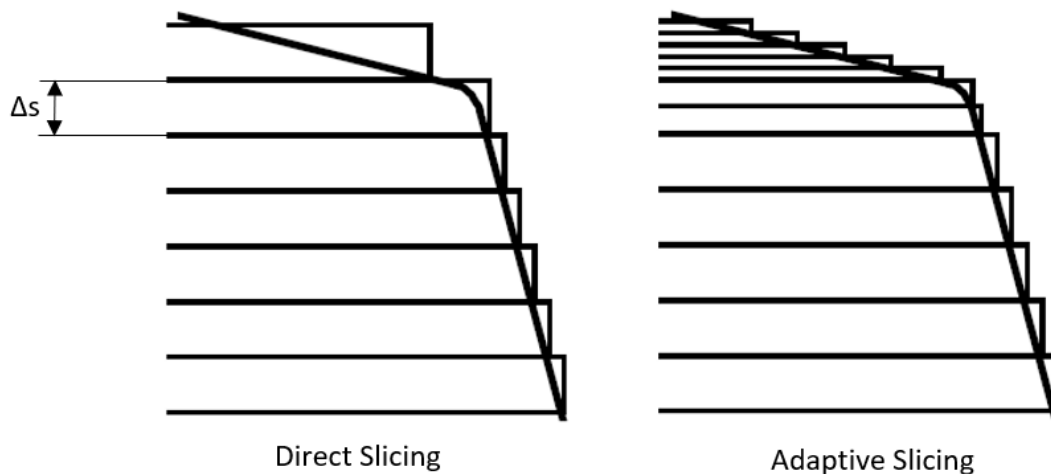


Figure 3. Direct Slicing vs. Adaptive Slicing

Following the previous flowchart, once the slicing process is completed, the AM machine proceeds in building the part. The process is fully automated and the operator only needs to provide the correct process parameters (such as material constraints, energy source, layer thickness and timing) as inputs. The whole building process can then be carried out without supervision, even if superficial monitoring of the machine is still requested mainly to avoid errors during the building stages (material/power shortages or software glitches).

Once the part has been completed, it can be manually removed from the platform by the operator and, as final step, it is subjected to post-processing operations such as surface finishing (to improve its aesthetics) or heat treatments (to improve its mechanical performances).

1.1 AM Materials

According to the final part operating scenario, different materials can be used. In particular, it is possible to distinguish between polymeric, metallic and composites materials, that also influence the chosen technology to carry out the process.

Generally, the used polymers are liquid resin-based materials, powders or solid filaments that are fed in the AM machine to produce the required part. Therefore, the material classification follows the traditional standard, where it is possible to distinguish thermoplastics, thermos-settings and elastomers. Sometimes they can also be coupled together in order to obtain composites with the aim to enhance the mechanical properties and performances of the final product.

Thermo-setting materials are characterized by a high level of cross-linking, with the presence of covalent bonds between each single monomer that establish a three-dimensional network. Due to the presence of strong bonds between each single element, a high amount of energy to break them is required, for this reason once they are solidified, they cannot be melted again since the required temperature will overcome the degradation one. These materials show a very high elastic module with consequent high mechanical performances, but they are not able to sustain plastic deformations.

Thermo-plastic materials are made up of linear chains with the presence of lateral branches that influence their behaviour. According to their micro-structure, it is possible to distinguish between amorphous and semi-crystalline polymers. When dealing with amorphous materials, chains are chaotically disposed, while for semi-crystalline materials there are chain folded regions connected by amorphous portions. This means that, for amorphous micro-structures the transition temperature between solid and liquid states is fixed and, for semi-crystalline ones, the transition between the two states happens within a specific temperature interval. These materials show good mechanical performances, lower than the ones of thermos-settings, but they are able to sustain both elastic and plastic deformations.

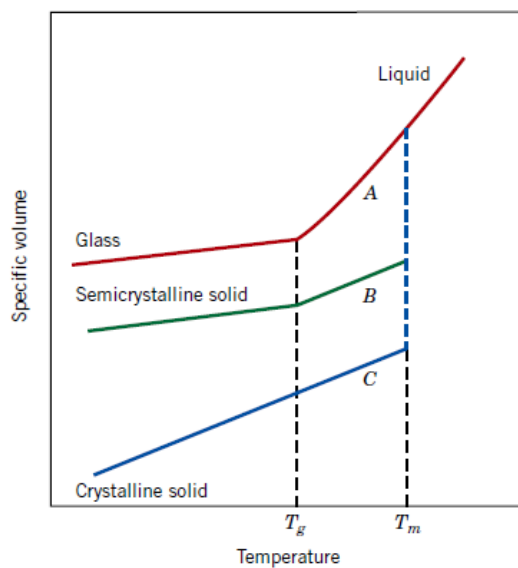


Figure 4. Transition Temperatures (Amorphous vs. Semi-crystalline)

Considering elastomers, they are characterized by a low level of cross-linking and due to their extremely low glass temperature, they are already in a rubber-like state at room temperature. These materials are able to sustain high deformations thanks to the presence of sulfur bridges established during the vulcanization process that are able to recollect the micro-structure to the original configuration when the applied load is no longer present. The original state is not reached immediately, but after a certain amount of time due to energy dissipations that take place in the material, following an hysteresis cycle. Thanks to this specific behaviour, elastomers are generally used in applications where high energy absorption and crashworthiness are required. However, these materials provide low mechanical performances since they can sustain low stresses and elastic deformations only.

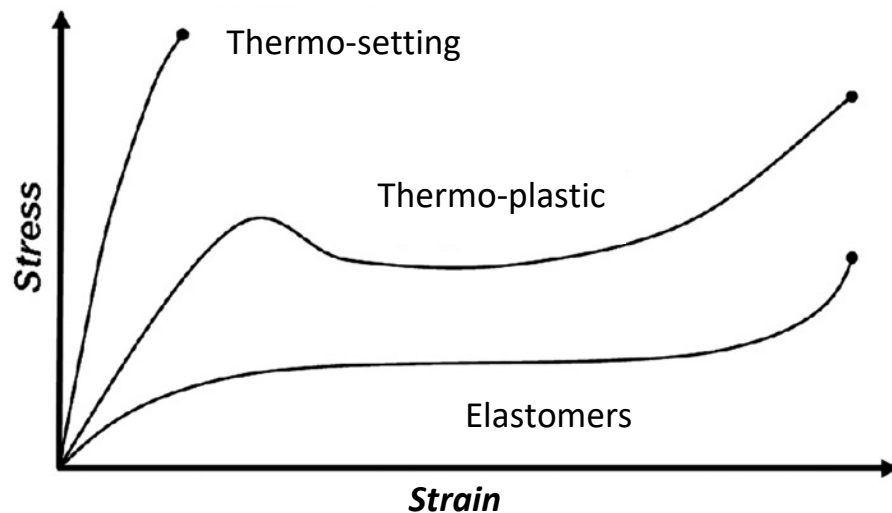


Figure 5. Polymers Mechanical Performances

When dealing with metallic materials, they are generally used in AM processes as powders. Similarly to technologies using liquid-based resins, the final part is produced by selectively melting the metal powder layer-by-layer. These materials are characterized by the presence of metallic bonds that are established by considering electrons (e^-) moving around nuclei of metal atoms that can be considered as a cloud of positively charged ions (+).

When operating with metal powders, some of the most important elements to consider is their morphology and chemical composition since they can influence the final part quality. Depending on the powder size, it is possible to distinguish between:

- **Fine - Very fine (15 ÷ 80 μm)** → processed by L-PBF (Laser Powder Bed Fusion)
- **Medium - Coarse (50 ÷ 100 μm)** → processed by EBM (Electron Beam Melting)
- **Coarse (50 ÷ 150 μm)** → processed by DED (Direct Energy Deposition)

Metal powders properties are highly influenced by the used atomization method and the manufacturing process conditions. In particular, in order to produce the required powder, it is possible to consider different methods, such as:

- **Water Atomization** → liquid metal poured in a tundish from above and atomized thanks to the presence of symmetrically positioned water jets. This technique provides irregular particles that need to undergo through post-processing.
- **Gas Atomization** → metal ingots melted in a VIM (Vacuum Induction Furnace) and introduced in the atomization chamber from above. The atomizing medium is generally an inert gas (N₂ or Ar) and this technique provides more spherical particles.
- **Plasma Atomization** → uses metal wires or powders as feedstock directly introduced in the atomization chamber, where they are simultaneously melted and atomized by means of co-axial plasma torches and gas jets. This technique provides the most regular particles.

Powders can be characterized by defects that influence the final part integrity and quality. Some of the main defects that can be found are related to porosities, morphology, contaminations and roughness. Other analyses should be done also to evaluate the powder density and humidity since they directly influence the material flowability and final part porosity, respectively.

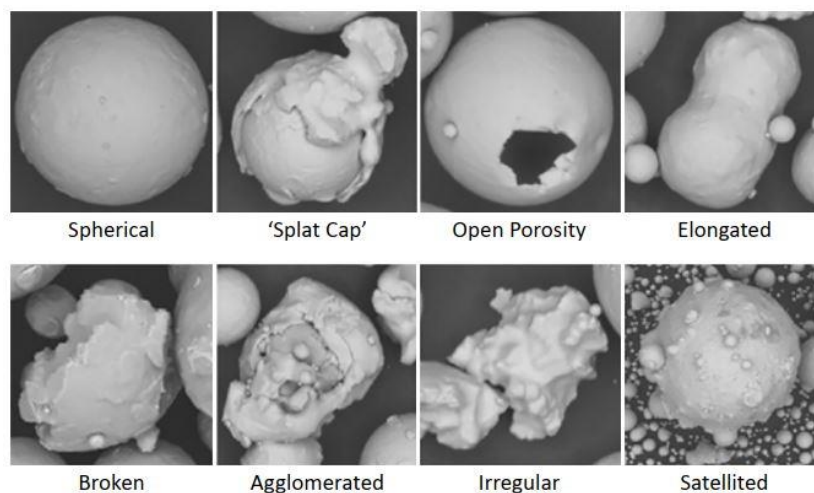


Figure 6. Metal Powder Defects

Considering the main metallic materials that can be used in AM processes, they are:

- **Al-Alloys** → AlSi10Mg, AlSi7Mg
- **Ni Super-Alloys** → Inconel 625, Inconel 718, Hastelloy X
- **Stainless Steels** → AISI 316L, 17-4 PH, 15-5 PH
- **Ti-Alloys** → Ti6Al4V
- **TiAl-Alloys & Composites** → Inconel 625+TiC, Inconel 625+TiB₂, Inconel 718+W

Composites are used in order to increase the material hardness, mechanical properties and wear resistance. Also in this case, according to the used material, due to the different composition and thermal/mechanical properties, the used process can vary.

1.2 AM Technologies & Costs

As already said, depending on the used materials, it is possible to identify different types of AM technologies to build a part. In particular, the main distinction is made between polymers and metals since in the first case there are processes that use liquid-based resins, polymeric powders or filaments, while in the second case there are processes mainly carried out using powders.

Considering polymeric materials, the main technologies to be implemented are:

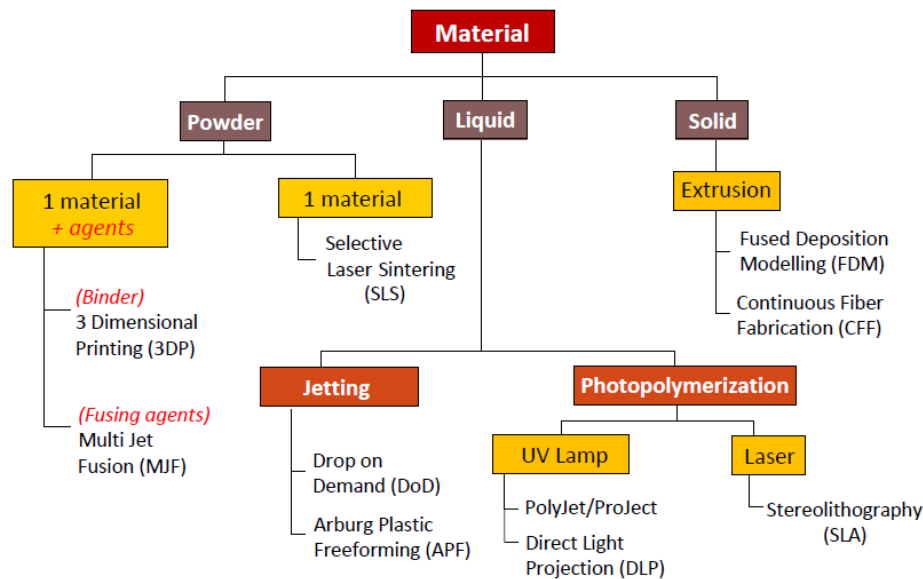


Figure 7. Process Classification for Polymers

Considering SLA, it is carried out with liquid resins (thermo-setting) that are sensitive to UV laser radiations. In particular, the process working principle is based on photopolymerization, that allow to produce near net shape by selectively applying the radiation to the desired section and start the polymer curing mechanism. The most common photopolymers can be classified as:

- **Acrylic** → used for aesthetic models' production
- **Epoxy** → with high viscosity and ensuring the best performances in terms of precision and mechanical properties
- **Vinyl** → to be used whenever there are humidity problems

The part being built rests on a platform that is dipped inside a vat filled with liquid material that slides downwards as soon as a new layer is built. In order to allow parts production with this technology, polymers have to provide high reactivity to radiation, low activation energy, stable viscosity, low shrinkage and good mechanical performances after polymerization. Low material shrinkage is fundamental since when resins photopolymerize, they tend to shrink due to volume contractions, leading to curl distortions. SLA allows to reach good part accuracy and surface finish combined with moderate mechanical performances.

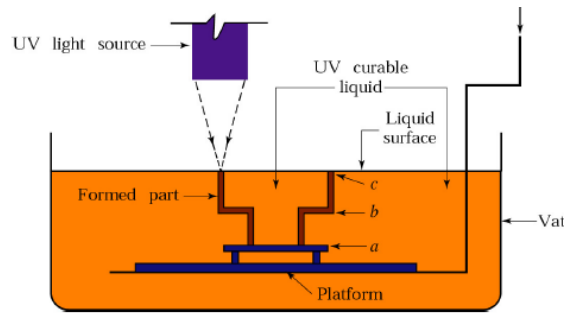


Figure 8. SLA Process

Similarly to SLA, the DLP technology exploits the photopolymerization principle in order to produce parts starting from liquid resins. In this case the process uses UV light to selectively activate the polymer curing process. The main difference is that now the UV source is not placed over the resin vat, but under it so that the platform is moving upwards with the part being built layer-by-layer secured to it by means of supports made up of the same material as the final part and that needs to be mechanically removed. Also in this case, there will be good performances in terms of surface finish and accuracy with a wide range of thermo-setting photopolymers that can be used in the process.

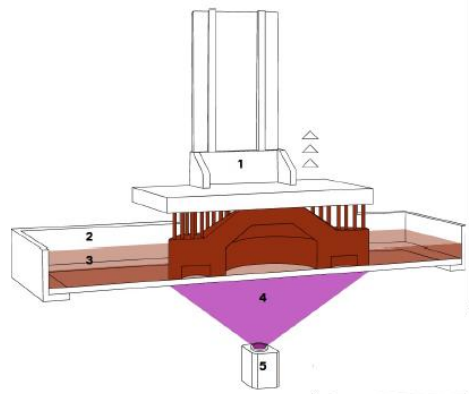


Figure 9. DLP Process

Considering processes exploiting solid polymers, it is possible to analyse FDM, that ensures material deposition by extrusion of polymeric filaments or pellets. Also in this case, it will be possible to use different materials for part and supports, that can be soluble in water. This technology uses a filament of polymeric material that is softened, melted, and forced to pass through a nozzle of reduced diameter that allow to deposit the material layer-by-layer on the platform. The filament is rolled around support spools and the passage through the nozzle is ensured by a specific feeding system (made up of a stepper motor and a set of gears that pinch and press the material through a guiding tube connected to the nozzle).

Industrial machines are generally characterized by two extruders, one used to deposit the building material and one to deploy the soluble support material. Also in this case the process allows to obtain good performances in terms of dimensional tolerances and surface roughness with absence of post-processing operations to remove the supports.

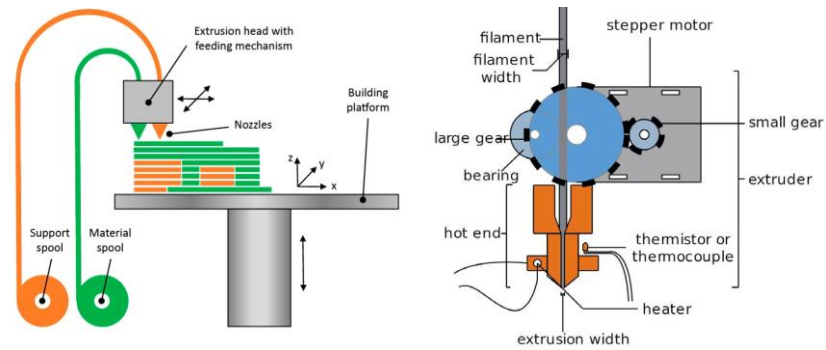


Figure 10. FDM Process & Feeding System

Considering processes exploiting polymeric powders, it is possible to take into account SLS. This process is based on powder bed fusion (PBF) techniques that allow to selectively melt powders layer-by-layer thanks to the use of CO₂ laser beams guided by scanning mirrors. The part building process takes place in an enclosed chamber filled with an inert gas in order to avoid oxidation and degradation of the powdered material. The powder bed is also kept at high temperatures by means of heaters in order to avoid thermal gradients that can introduce residual stresses and curling in the final part.

After each layer is completed, the platform is lowered by one layer thickness and a new powder layer is spread and levelled by means of a re-coater. In particular, the layer thickness is determined by the laser focus, the higher the focus, the narrower the invested powder bed portion and thinner the layer. Once the part is completed the process ends and a cool-down period is usually observed in order to allow the component uniform cooling. This technology does not require supports, allows to perform 3D nesting to optimize the material utilization and the only required post-processing operations are mainly related to dust cleaning.

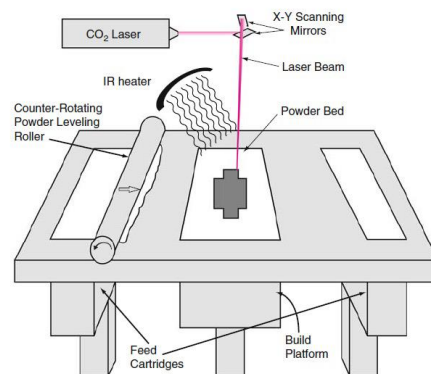


Figure 11. SLS Process

Considering AM technologies for metallic materials, as already said, the majority of the processes exploit metal powders and the main applications can be found in L-PBF (Laser Powder Bed Fusion), EBM (Electron Beam Melting) and DED (Direct Energy deposition).

Considering L-PBF, it exploits the same working principle as SLS used for polymers. In particular, this technology uses a laser beam to selectively melt fine metal powders layer-by-layer and build fully-dense parts. The laser is initially sent horizontally and it is deviated

by means of a scanning mirror that makes it perpendicular to the powder bed. The resulting beam then passes through a set of F - θ - lenses in order to improve its direction and focus. Also in this case the platform is covered by a powder layer by means of a re-coater and it is lowered after each irradiation by a distance equal to the layer thickness. The whole process is carried out inside a chamber filled with inert gas in order to wash away oxygen and smoke and avoid oxidation of the newly built layer that is still at high temperature. Due to the high temperatures reached during the process, once the part is completed it is subjected (together with the platform) to thermal treatments in order to perform residual stresses relieving before being completely removed from the chamber. Depending on the part geometry and orientation, it is possible to perform 3D nesting operations and consider whether to adopt supports or not.

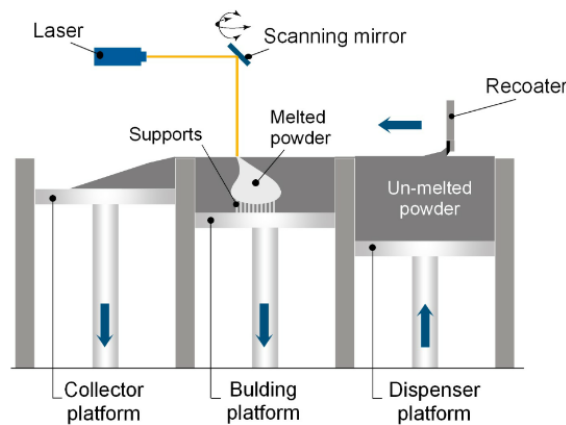


Figure 12. L-PBF Process

Considering EBM, it is a similar process to L-PBF, but instead of using a laser beam, it uses an electron beam emitted by a heated filament ($> 2500\text{ }^{\circ}\text{C}$) or by a crystal (more expensive). The beam is accelerated through the anode and passes through three different coils (lenses) that are able to control the beam by means of magnetic fields that allow to adjust its focus (astigmatism and focus lenses) and its deflection (deflection lens). The whole process is carried out inside a chamber in high vacuum conditions in order to avoid powder oxidation, even if helium can be used as substitute in order to avoid scatterings coming from the interaction between electrons and air. Also in this case, the powder is selectively melted layer-by-layer thanks to heat generated from the dissipation of the beam kinetic energy. Due to the extremely high temperatures reached during the material melting operations, sintering between one layer and the other is present and the re-coater spreads new powder layers in three steps in order to provide a surface as regular as possible. Moreover, each layer is heated in order not to have temperature gradients (and decrease residual stresses in the final part) and to avoid negative charges in the particles that will result in beam repulsions.

The first layer is directly printed on the platform so that a connection through earth is performed to dissipate the residual charges of the following layers due to their interaction with the beam. Generally, due to the high process temperatures, as soon as the completed parts cools down, it can experience shrinkage. This means that when designing the part, some over-material has to be taken into account in order to provide near net shape final parts.

Moreover, post-processing and heat treatments are also required to remove partially sintered powder and decrease residual stresses, respectively. EBM allows to perform 3D nesting and this technology is mainly used to manufacture parts made up of materials characterized by high melting temperatures, such as Ti and Co.

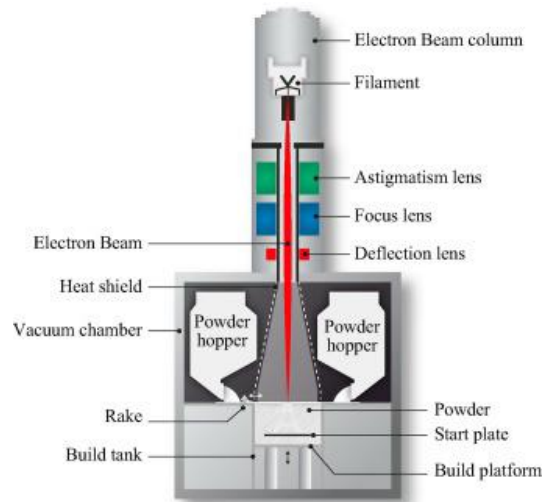


Figure 13. EBM Process

The last process to be analysed is DED, allowing the creation of parts by melting and depositing material from powder or wire feedstock on selected areas layer-by-layer. This process exploits energy deposition by means of a beam that is used to heat and melt the material being deposited and can also be used to repair already existing damaged components.

The process working principle is based on the presence of a laser beam focused on a specific substrate region that heats it and creates a melt pool. Once the melt pool is created, the powder is introduced inside it (by means of a dedicated nozzle) causing its increase in size. This means that, during the part manufacturing, the powder remains in the solid state until it interacts with the laser beam. The whole process is protected by a stream of inert gas (Ar) directed only on the melt pool in order to protect it from oxidation. As a consequence, as soon as the laser moves away from the melt pool, the material solidifies and a raised track is obtained. Since the material can still be at high temperature, it is very important to carefully set the laser speed in order to allow the material solidification when the inert gas is still protecting it.

The layer thickness and the laser-powder interaction depend on the standoff distance and powder particle velocity, while the temperature distribution in the layer depends on the laser power, travel speed and powder feed rate. Due to the high temperatures reached by the energy source, large temperature gradients and residual stresses will be present in the final part, leading to defects such as delamination, cracks and distortions. For this reason, heat treatments and post processing operations are required.

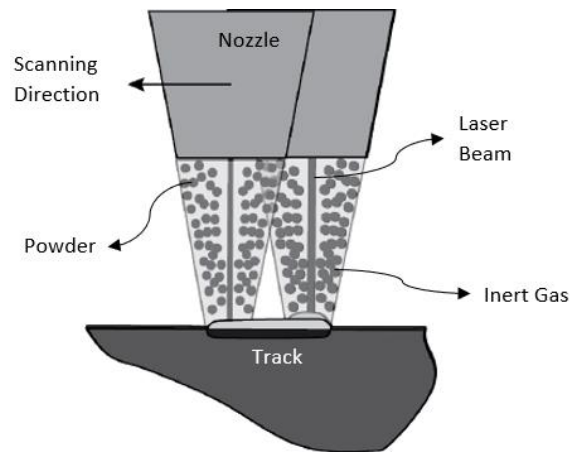


Figure 14. DED Process

Considering the three previous processes, it is possible to provide a cost breakdown based on the energy and consumable expenditures. In particular, the analysis will take in charge all the different initial investments, power and energy requirements, inert gas and powder volumes according to the chamber dimensions. Different machine variants are present in the market and, it is evident that, according to the specific productivity targets that have to be met, different costs have to be sustained. To this extent, in order to provide a more representative comparison between all the previously presented technologies, machines with similar production capabilities will be addressed.

Taking into account L-PBF systems, several manufacturers (such as EOS® and General Electrics®), are present in the market with different options. Considering some of the most popular machines adopted by majority of companies, they are the EOS® M 290, EOS® M 400 and EOS® M 400-4, each one characterized by different dimensions, energy expenditures and production rates (with the EOS® M 290 being the smallest among the three).

With regards to EBM systems, some of the main manufactures are Arcam® and Stratasys®, providing machine portfolios ranging from medical to aerospace applications. In particular, one of the most popular system adopted both for automotive and aerospace components is the Arcam® EBM Q20 Plus, mainly involved in structural parts and engine components productions. An alternative to this machine could be the Arcam® EBM A2X, designed to manufacture components made up of materials requiring high process temperatures (e.g. TiAl, Hastelloy X or Inconel).

Finally, for what concerns DED processes, the main manufacturers able to develop suitable systems are OPTOMECH® and DMG MORI®. Specifically, some of the most popular machines are the ones belonging to the OPTOMECH® LENS Classic System Series (such as the 450, MR-7 and 850-R), characterized by hermetically sealed chambers and atmosphere control in order to meet industry's most demanding metal fabrication, part restoration and surface modification requirements.

Among all the systems presented before, the chosen machines in order to carry on a satisfactory cost and energy expenditure analysis will be the ones most likely to be used in an industrial large scale production scenario.

Said that, the reference models will be the EOS® M400-4, the Arcam® Q20 Plus and the OPTOMECC® LENS 850-R. The main costs and specifications for each one of these machines are:

- **EOS® M400-4**

Table 1. EOS® M400-4 Cost & Specifications

Purchasing Cost	<i>> 1.000.000 €</i>
Building Volume	<i>400 x 400 x 400 mm</i>
Laser Type	<i>4 x Yb-fibre lasers</i>
Laser Power Requirement	<i>4 x 400 W</i>
Precision Optics	<i>4 x F-θ-lenses</i>
Power Supply	<i>3 x 50 A</i>
Power Consumption	<i>max 45 kW (typical 22 kW)</i>
Inert Gas Supply	<i>20 m³/h (7000 hPa)</i>

- **Arcam® Q20 Plus**

Table 2. Arcam® Q20 Plus Cost & Specifications

Purchasing Cost	<i>> 250.000 €</i>
Building Volume	<i>350 x 380 mm (Φ/H)</i>
Beam Type	<i>Single crystalline</i>
Beam Power Requirement	<i>3000 W</i>
Vacuum Base Pressure	<i>5 x 10⁻⁴ mbar</i>
Power Supply	<i>3 x 400 V</i>
Inert Gas Supply (Building)	<i>0,24 m³/h</i>
Inert Gas Supply (Cooling)	<i>6 ÷ 9 m³/build</i>

- **OPTOMECC® LENS 850-R**

Table 3. OPTOMECC® LENS 850-R Cost & Specifications

Purchasing Cost	<i>> 700.000 €</i>
Building Volume	<i>900 x 1500 x 900 mm</i>
Laser Type	<i>1 x fibre laser</i>
Laser Power Requirement	<i>1 ÷ 4 kW</i>
Motion Control	<i>5 – axes standard (full CNC control)</i>
Inert Gas Supply (Building)	<i>0,4 m³/h</i>

In particular, it is possible to consider different costs and gains when adopting AM:

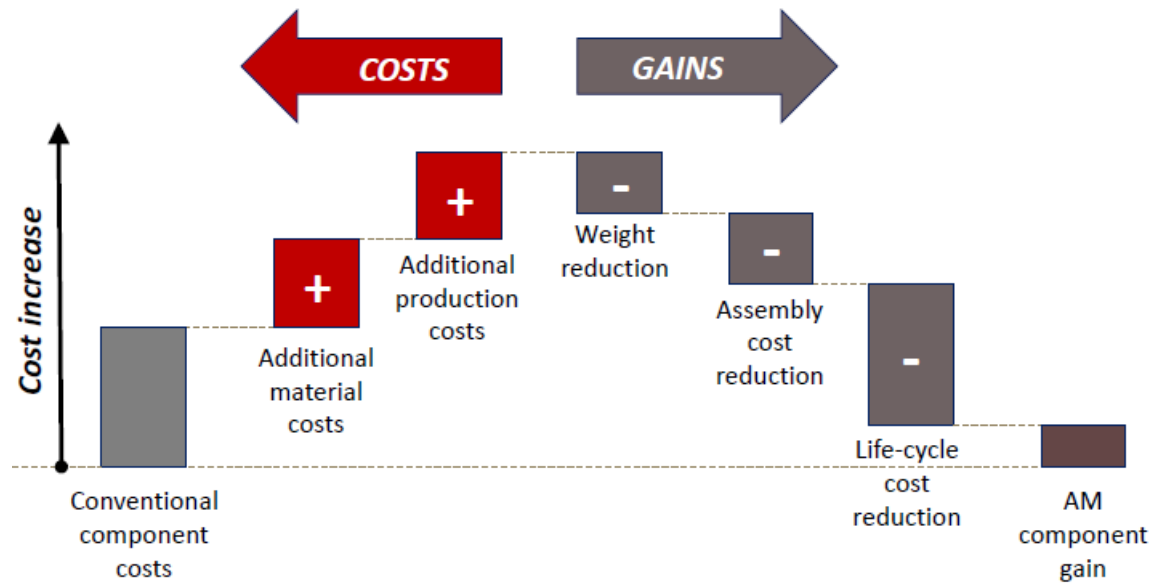


Figure 15. AM Costs & Gains Comparison

From the figure above, it is evident how the additional costs are well balanced by the obtained gains.

The increased costs are deriving from additional material costs and additional production costs since materials are more expensive due to the atomization process that have to sustain to make them suitable to be processed by AM and production results more expensive than traditional one due to increased amounts of required energy and more expensive equipment (especially for L-PBF and EBM).

The gains, instead, are deriving from an improved material utilization that allows to use material only where needed, resulting in weight savings. Moreover, thanks to part consolidation, it is possible to sensibly decrease the number of needed components to be assembled, decreasing the assembly costs. The possibility to improve material utilization and decrease components also allow to improve the structural performances of the final product, which will be mechanically stronger due to lower redundancies (in used materials and assembly points) that can initiate cracks under fatigue loads.

Considering all these elements, the overall evaluation for a specific component developed by means of AM will result in improvements related to life-cycle cost reductions and in a longer component life, meaning that also the LCA will be subjected to improvements depending on the component dimension and on how much the technology capabilities have been exploited in building the part.

2. Design for Additive Manufacturing (DfAM)

When dealing with any product, the designer has the great responsibility to ensure that a product will comply with the customers and quality requirements. In order to do this, it is fundamental that, during the early concept phase, great care and attention is devoted to any possible manufacturing problem.

It is possible to consider a dedicated approach between design and manufacturing stages, which allows to consider the optimal design first and then to apply the geometric simplifications required to improve the material utilization and make it more complex. This step is particularly important because whenever AM is considered, it is necessary to provide a design for functionality. In particular, comparing additive with traditional processes, if the component is well designed under a structural point of view, it is possible to gain some advantages in terms of costs and material utilization that will make it possible to obtain complexity for free.

In order to deploy DfAM principles, designers must have a high knowledge of the component and of the manufacturing process, since the manufacturing constraints and the final operating scenario greatly influence the design choices. In particular, this design phase allows to build parts with unlimited complexity, breaking the tooling constraints that allows to maximize the product performances through synthesis of shapes, sizes, structures and material composition. All the advantages are related to the fact that, through DfAM, is possible to add material only where needed, even if the properties of the components are also influenced by the material internal characteristics and microstructure.^[1]

To manufacture the initial design, interpretation and adaption for AM is often needed. In order to do this, design rules aiming at describing what could be manufactured using AM and what are the main limitations, are taken into consideration. The design verification is similar to the design process for other manufacturing techniques and it includes CAE analyses for the verification of structural, thermal, aerodynamic and other properties.^[2]

DfAM principles take into account the final assembly of the product and improves the effectiveness of the mechanical response when the part is subjected to loads. It is important to properly set the building direction in order to avoid the possibility of anisotropy (where the components properties are affected by the load direction). Thanks to the possibility to develop the component using 3D CAD software, it is possible to save considerable amounts of development time and costs.^[3]

There are diverse types of DfAM principles that can be followed according to the considered technology. For example, when dealing with DMLS (Direct Metal Laser Sintering), it is necessary to take into account specific guidelines for angled and downward facing surfaces, since the powder in the building chamber does not provide any support to the part as it is built. For this reason, if the surface has a too acute angle with respect to the platform, it will need supporting structures, which can negatively impact on the surface quality. In order to avoid the presence of supports, it is possible to consider some minimum angles depending on the used material. In particular, Aluminum and Inconel are characterized by 45° minimum angles, while Stainless Steel, Titanium and Cobalt Chrome materials are characterized by 30° minimum angles.

Considering downward-facing structures, they will always require support structures, which can be either filling the hole left by the downward facing surface or presenting an offset so that it can be easily removed.

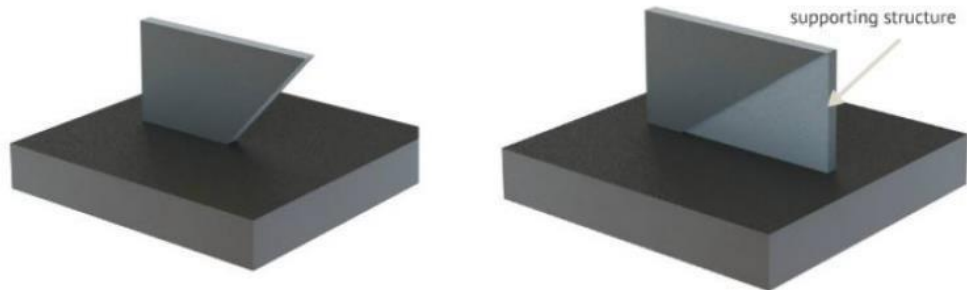


Figure 16. Angled & Downward-facing Structures

High attention should also be given to horizontal holes since their shapes and dimensions can affect the presence or the absence of supports. Generally, holes that are smaller than 6 mm in diameter or that are characterized by an arched upper area do not require any supporting structure, while holes with larger circular dimensions are presenting supports or rougher surfaces that may need post-machining operations.

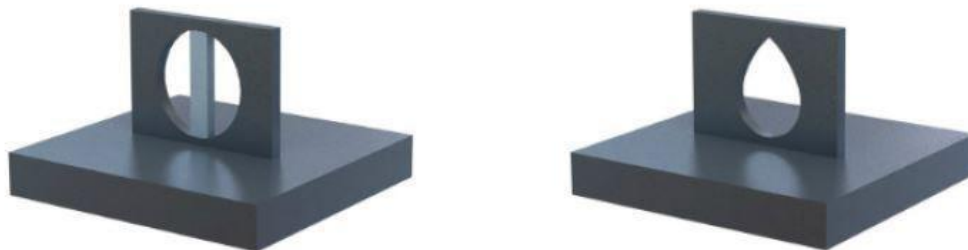


Figure 17. Horizontal Holes

Attention should also be paid to the building directions and cross-section areas since they should be placed accordingly to the re-coater blade direction. This is due to the fact that as the re-coater blade passes over the part to deposit another powder layer, it could touch the layer below, sometimes exerting some shear forces causing the part to bend.

Generally, the orientation of the part should be perpendicular or at least with a certain angle with respect to the blade in order to avoid this phenomenon. The ideal case is given by an open U-shape with the lead rounded edges offering high resistance to the force exerted by the re-coater. The worst-case geometry is given by a section parallel to the blade. If there are space constraints causing the impossibility to place the component perpendicularly to the blade, there should be at least a 5° angle of inclination with respect to the blade direction and the section should provide rounded edges. It is also advisable to consider a ratio between section height and area lower than 8:1 to avoid too slender components that can be bent by the blade.



Figure 18. Cross-Section Orientation with respect to Re-Coater Blade Motion

For what concerns DfAM guidelines for SLS (Selective Laser Sintering) processes, there are some constraints mainly related to the high temperatures experienced during the printing operations. In particular, it is necessary to take into account about 3.5% of over-material to counteract the effects of shrinkage and to add ribs to large flat surfaces in order to avoid warping. Other constraints are affecting the wall thickness (that should be at least of 0.8 mm) and the hole dimensions (that should be larger than 1.5 mm). Since SLS is conducted using powders, it is also necessary to consider the presence of escape holes or hollow structures to remove loose and unsintered powder, but also to save weight and costs. This type of holes must have a minimum diameter of 3.5 mm.

Other important guidelines are related to the tolerances of matching components that can also be moving one with respect to the other (like spur gears). In this case the maximum values are generally ranging between ± 0.3 mm and ± 0.5 mm. Other considerations can also be made for what concerns text and engraved details to ensure correct visibility and readability of specific features on the parts.

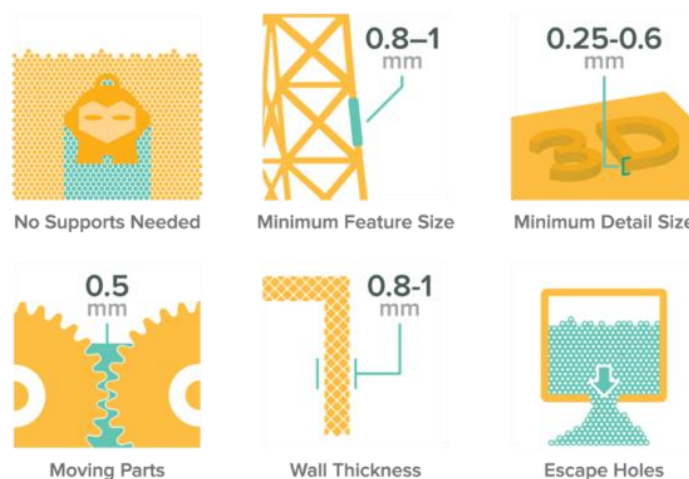


Figure 19. DfAM Guidelines for SLS

2.1 Generative Design & Topology Optimization

According to the different quality and performance requirements provided by the customer, it is possible to provide several alternatives for what concerns process parameters and part orientations. Once the most suitable configuration has been found following a trade-off between building time, costs and performances, it is possible to deploy Generative Design (GD) and Topology Optimization (TO) techniques. The two phases are following different approaches, since GD is mainly used in order to explore all the possible design opportunities, while TO is useful in order to optimize material utilization once the desired design has been found.

When dealing with Generative Design, it can be implemented in CAD environment during the early design stages in order to explore the majority of the design possibilities. The main objective of this approach is to assist human designers to explore a larger range of design possibilities than what is usually possible for the class of problems outlined by design constraints. However, it is still a designer-driven process.^[4]

The current aim of GD is to create new design processes that are producing spatially novel, yet efficient and buildable, design through exploitation of current computing and manufacturing capabilities. This technique is applicable to both parametric and procedural designs and it can be composed of the following components (that can be changed by the designer according to the outcomes):

1. A design scheme → **Configuration**
2. A mean of creating variations → **Variation**
3. A mean of selecting desirable outcomes → **Decision-Making Response**

The GD method is applicable by following several steps^[5]:

1. **Creating the Generic Model** → objects with same geometry but different constraints
2. **Setting the Initial Envelope** → exploring the widest possible interval of solutions
3. **Generating Designs** → filtering all the designs too similar to other ones
4. **Filtering Phenotypes** → developing the accurate envelope by setting the exact constraints
5. **Selection & Fine Tuning** → exploring the proposed designs with a higher level of detail

GD is a category of technologies that suggests design options (or optimizes an existing design) to meet criteria defined by the user. Designers specify the part constraints and objectives in a GD software that proceeds in proposing an optimized part design which is optimized for weight, natural frequency and stiffness.

Taking into account TO techniques, they are generally exploited once the final design (obtained through GD approaches) has been selected. In this process, it is possible to re-design the component considering a better material utilization that allows to improve the mechanical properties of the component and to save weight and costs. In particular, a specific CAD software is used in order to rigorously evaluate the loads acting on the part in its final application.

TO gives solutions on how to place material within a prescribed design domain in order to obtain the best structural performances. The process is based on repeated analysis and design update steps, mostly guided by gradient computation. The general optimization problem is related to the finding of a solution to a cost function. The variable to be controlled is the material distribution (density) and the solution of the problem can be defined as the material distribution that minimizes an objective function subjected to a volume constraint.

The problem solution can give back two values at any point of the design domain defined in the space. In particular, the solution can be 0 (void) or 1 (solid material) and the TO problem can be tackled in two ways^[6]:

1. **Shape Optimization Problem** → Lagrangian (boundary following mesh)
2. **Density Optimization Problem** → Eulerian (fixed mesh)

The need for TO relies on the requirement for structural integrity. This integrity can be achieved by strategically select materials, manufacturing methods and component geometry. The selection of component geometry directly influences its reliability. Successful geometric designs result in efficient material utilization with light-weight structures that achieve their purpose with minimal structurally redundant material.

TO can be applied to all the components manufactured following sub-optimal designs (technically redundant material) and that can create limitations to the component manufacturing and assembly. These methods address the problem by providing a rapid understanding of structurally efficient material distributions so that the component could be optimized in terms of material utilization, weight, available design time and performances.^[7]

Thanks to Topology Optimization, the part design could be optimized in terms of weight minimization, static/dynamic performance maximization, optimal thermal behavior, integration of different functions and parts count minimization. In summary, it is a technology optimizing the material layout within a given design space with the aim to optimize a part property while respecting a set of constraints.

To provide effective design outcomes, it is desirable that structural optimization methods are systematic and independent on the designer's intuition and that allow the identification of effective geometric connectivity for complex loading scenarios. By means of TO applied to GD, it is possible to build complex components that can't be manufactured with traditional methods due to manufacturing constraints. However, the outcome of TO is often a trade-off between shape complexity and AM manufacturability.^[5]

2.2 Part Consolidation

Part consolidation plays a particularly important role when dealing with AM processes, especially during the design phase carried out following DfAM principles. Part consolidation is generally used for components made up of several parts that need to be joined together, so that they could be produced as a single part, even if multiple elements are present.^[8]

Part consolidation is also important because it allows to optimize the part geometry, to improve the material utilization and mechanical properties by analyzing the component considering the loads acting on it and the main sections involved in the real-life application. Another important aspect of part consolidation regards the introduction of lattice structures that can be homogeneous or heterogeneous. In both cases, these elements are used in order to optimize the design space coming from the part consolidation in terms of thickness, weight and structural performances.^[9]

Generally, this process is performed in 3D CAD environments, where it is possible to develop a component re-design by applying specific loads and constraints to the part and deploy topology optimization by exploiting integrated tools in the software. TO is fundamental in order to re-design all the components provided as 3D drawings that are generally built following guidelines applied to traditional processes. In this way it will be possible to manufacture more complex structures without the need of traditional manufacturing stages, with the re-designed components that will benefit from this operation by having improved performances.^[10]

When dealing with part consolidation, other than considering the part optimization taking into account material utilization and performances, it could also be possible to provide other evaluations that will allow to obtain a cost-effective design (e.g. the energy consumption and the life cycle gains of the specific part).

Some of the biggest drawbacks of part consolidation are related to the fact that the procedure is highly dependent on the designers' skills and experience. Moreover, it is necessary to have a high clarity on the final part destination of use in order to obtain the best possible design both in terms of optimization and performances, but also in terms of safety. Another important limitation of this technique is that the procedure is not well standardized, so there is no clarity on how to decrease the number of elements present in a component that is undergoing through optimization in the design phase.^[9]

Considering the main aspects to consider in part consolidation, generally the main focus is on the part optimization and on the possibility to achieve a cost-effective design that is also simpler to achieve with AM processes. This means that the performance improvements are considered only as a consequence of the design process since it is not the primary aim of this phase.

3. AM for Automotive Applications & Examples

The automotive sector is covering an important role in the world's economy and it is also seen as a breeding ground for new technologies, including AM. In order to adapt to the new trends and requests coming from new customers and regulations, as well as new economic scenarios, vehicles have undergone through a continuous evolution process.

Nowadays, the automotive sector is a complex environment that links together the production chain and the supply chain, which are extremely sensitive to changes in the market trends. For this reason, the major efforts are pointing towards a lean approach, which allows to obtain a supply chain that is as more flexible as possible. The lean manufacturing is based on a JIT (Just In Time) logic that allows to provide the customer with the desired product, in the exact quantity and in the right time. This trend has a high potential when AM is considered, since this technology allows to establish an "on-demand" production system that is pulled by the customer thanks to the lower lead times.

In particular, when dealing with the JIT approach, the main focus is related to the elimination (or the decrease) of the major sources of wastes, such as:

- **MURI** → excessive production
- **MURA** → demand fluctuations
- **MUDA** → non value-added activities (time consuming)

The lean manufacturing allows to pursue the zero-waste objective and the continuous improvement goal, which allows to obtain the highest possible service level with the highest possible quality. In order to achieve these targets, it is necessary to balance as much as possible the supply chain, levelling the production in order to avoid products' surplus and fluctuations due to seasonality. To do this, it is fundamental to consider mapping procedures that allow to distinguish value-added activities from non-value-added activities. Generally, the non-value-added activities are the ones that are not adding value to the final product, but they are time consuming, so they are the first ones to be addressed when deploying a lean approach.

Nowadays, the major AM applications in the automotive sector are mainly related to mass customization and rapid prototyping phases, due to the technology high costs, but major efforts are being performed in order to make this technology fundamental in product innovations and high-volume direct manufacturing. Some applications can also be seen in high segments vehicles, where the costs related to AM deployment have a minor impact on the vehicle final cost.

AM in automotive industry gives the possibility to innovate components and to operate with lower constraints, therefore it will be possible to achieve more complex and lighter elements (lattices) that can also be built by using multiple materials in shorter times. Moreover, it also deploys the possibility to achieve mass-customization. The technology can also be used to modify the supply chain, eliminating the need for new tooling and massively decrease the amount of stock material to be kept in warehouse. Moreover, thanks to the lower weight of the components, there would be beneficial effects also in terms of material handling costs.^[11]

The use of AM technologies can also decrease the expenses related to the need for procured parts coming from suppliers, by enabling the OEM to internally develop the components. This will have beneficial effects on the R&D process and on the company know-how. Additive manufacturing can also be used for providing specific components for vehicles no longer in the market (especially historical ones), allowing to enter a new market share that is growing in popularity and that nowadays is mainly covered by retailers, rather than carmakers.^[12]

AM used to fabricate automotive components is also important in order to decrease the overall vehicle emissions thanks to the high weight savings that can be performed. This will be translated into decreased life-cycle environmental impacts, which are larger as the larger is the number of parts that can be printed by means of AM. Components light-weighting is also a key factor to decrease energy consumption.^[13]

Some limitations can be mainly related to the low number of available materials and, therefore, to the high costs of the already present ones. Moreover, it is also important to improve the product quality and to reduce the post-processing operations, which are costly both in terms of money and in terms of time. Another important key issue is related to the limited size of the components that can be manufactured, mainly related to the restriction in terms of building chamber of the actual machines.^[14]

When dealing with development and manufacturing operations related to high performance automotive components, it is fundamental to apply the DfAM principles. In particular, these principles are relevant when dealing with topology optimization and performance analysis of the parts to be produced (both performed in a virtual environment). Generally, the overall results are very accurate and allow to effectively evaluate results very similar to the ones that can be achieved in real testing conditions, saving development costs and time.^[15]

Profitability in the automotive industry is driven by volume. Given these enormous volumes, the low production speed of AM is a significant impediment to its wider adoption for direct part manufacturing. This has made high-speed AM an important area of research. Despite of this, AM offers a versatile set of technologies that can support automotive companies as they pursue performance, growth, and innovation. However, traditional production processes, especially for low segment vehicles, will still hold a dominant position in future years.^[16]

Summing up, the main advantages of AM applied to the automotive sector are^[17]:

- Parts designs can be implemented in faster times and with lower costs and this can be applied to tools, spare parts or end-use parts, with even higher savings.
- Speed and flexibility allow carmakers to perform modifications faster than competitors and enter the market in a shorter time, gaining a strategical advantage.
- AM can be deployed in order to support an on demand production system that is suitable both for series production and for spare parts needed for vehicles that are no longer in production (this also allows to provide benefits in terms of supply chain with lower inventory levels).
- AM allows designers to deploy more complex shapes that can be built at once without additional components thanks to part consolidation.

- AM also allows to obtain optimized shapes that also provide a more effective use of the material by adding it only where it is actually needed, translating everything into weight savings that can have massive effects in the environmental impact of a vehicle during its LCA (thanks to lower consumptions that is translated in lower emissions).

Considering the main disadvantages^[18]:

- AM is generally expensive to deploy for medium-small industries since the entry costs are remarkably high (in particular for what concerns the capitalization cost for the initial machine purchasing).
- Other high costs are generally sustained in order to produce the components both in terms of energy utilization and mainly in terms of powder production (with metal powders that are generally much more expensive than raw steel).
- Other limitations are provided by the fact that nowadays the available materials that can be used for AM processes are not so high in number, so car-makers are left with very few options that are still expensive.
- AM is still considered as a niche process due to its slow build rates and to its difficulty in deploying effective scale operations in order to be suitable for mass-production.
- Additional costs are also to be accounted for post-processing operations such as heat treatments and surface finishing that are labour intensive processes necessary to reduce residual stresses in the parts and to improve the surface quality after the manufacturing process.

Up to now, the main AM applications that can be found in the automotive sector are pertaining to structural components for high-segment and racing vehicles, even if some other examples can be analysed for common vehicles (only for mass customization purposes). Other important fields of application for the considered technology include the spare parts market both for vehicles still in production and historical vehicles no longer in production (resto-mod).

Considering high-segment vehicles, some applications can be found in the 2018 BMW® i8 Roadster model where, for the first time ever, a metal 3D-printed part is used in a production series vehicle. The developed component is a 3D-printed bracket that is 44% lighter than the baseline, attaches the convertible roof-cover and enables it to fold and unfold over the vehicle. 3D-printing improved the bracket's stiffness tenfold over an injection-molded version and it has proved its viability by being technically sensible and cost effective. The optimized bracket supports the roof-cover, which is many times heavier than the bracket itself, and successfully keeps displacements to a minimum to prevent the cover from collapsing during the opening process. The used material is AlSi10Mg and the chosen AM technology is L-PBF.



Figure 20. BMW® i8 Roadster 3D-printed Roof Bracket

Other examples are given by Porsche®, that developed 3D-printed components both for electric and ICE-based vehicles. In particular, they have developed 3D-printed pistons for their GT2 RS model, created with high precision Trumpf® TruPrint 3000 laser printer that builds the part layer-by-layer by selectively melting a powder layer (SLM) with an average thickness ranging between 0,02 mm and 0,1 mm. The used material is the M174+ (Al alloy) developed and provided by partner and part manufacturer MAHLE®. Each piston is composed of about 1200 layers of the fused alloy, taking about 12 hours to print. The components have to undergo through surface finish and heat treatments in order to meet the target performances, allowing to increase the total engine power by 30 HP.



Figure 21. Porsche® GT2 RS 3D-printed Pistons

Similarly to the Porsche GT2 RS 3D-printed pistons, the carmaker also developed a complete electric drive housing which also integrates a two-speed gearbox. This specific element is used on the front axle of the Porsche® Taycan and it is made up of an Al alloy provided as powder that is selectively melted to build the component layer-by-layer. The technology is LMF (Laser Metal Fusion) and, also in this case, the whole development was supported by MAHLE®. Lattices have been used in order to further reduce the component weight.



Figure 22. Porsche® Taycan 3D-printed Electric Drive Housing

Another example of AM technologies applied to high-segment vehicles is provided by Bugatti®, that developed the first 3D-printed brake caliper in the world. The caliper is a mono-block component able to host 8 pistons to slow the vehicle down. It has been built using Ti6Al4V thanks to its higher performances with respect to Al alloys, also because the caliper has to sustain very high temperatures and high forces (about 125 kg/mm²) deployed during braking. The used process is selective laser melting (SLM), and the component is still in its prototype stages.



Figure 23. Bugatti® Chiron 3D-printed Brake Caliper

Bugatti® also developed a large 3D-printed titanium exhaust pipe which is highly resistant to high temperatures and very light thanks to the benefits of the thin walls (0,5 mm) that 3D-printing can achieve. The weight savings amount to around 50 kg with respect to a traditional tail pipe system. This part was produced by APWORKS®, a German company that specializes in complex metal parts made via additive manufacturing. The chosen material is Ti6Al4V (due to its high temperature resistance) and the used technology is EBM.



Figure 24. Bugatti® Chiron Pur Sport 3D-printed Exhaust

Considering medium-low segment vehicles, the main AM applications are provided by Toyota®, GM® and Stellantis®. In particular, Toyota® developed AM components for their LQ model, identifying the vehicles outer mirrors as an opportunity to apply additive design and manufacturing technology since it offered the best optimized solution in terms of weight and aerodynamics for the mirror, reducing sound emissions and parts count and improving the overall crashworthiness. The recommended material is AlSi10Mg used with a selective laser melting AM technology (SLM) provided by DMG MORI®.



Figure 25. Toyota® LQ 3D-printed Outer Mirror

Stellantis® provided some examples of AM technologies applied to structural components, such as wheel carriers and door hinges, mainly used in Alfa Romeo®, Maserati® and Dodge® vehicles. Considering the wheel carrier, it allows to obtain a single assembly integrating together 12 components, with the use of AM processes that allows to reduce its weight by 36%. The developed part includes a wheel support, a heat shield, a hydraulic system and a brake caliper all together. The component shows a better material distribution and an overall increased fatigue resistance behaviour (thanks to decreased vibrations). The part is still in its prototyping stages and still needs to be implemented in real-life applications. The chosen material is AlSi10Mg used in a SLS process provided by German manufacturer Fraunhofer® IPT.

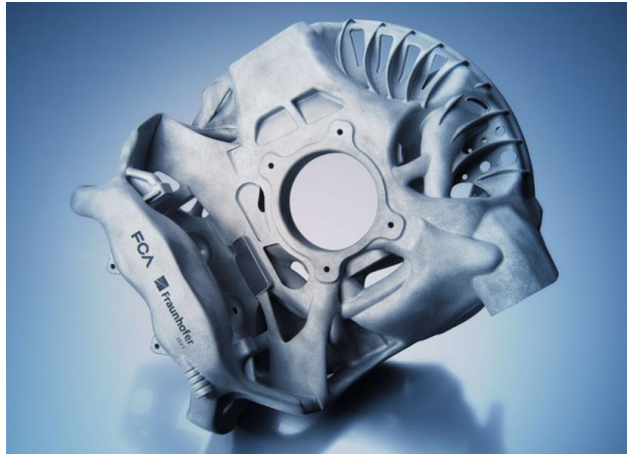


Figure 26. Stellantis® 3D-printed Wheel Carrier

The same manufacturer also uses AM technologies to build 3D-printed door hinges. The company has developed an optimized hinge in terms of geometry and performances by exploiting topology optimization applied to generative designs. The manufacturer took care of all the process parameters (such as part orientation and building speed) in order to maximize costs and weight savings gains and minimize post-processing. The chosen material for the hinge is AlSi10Mg and the used AM process is SLS. Thanks to the optimization, the company managed to save 35% of weight and 20% of costs.

The component is still a concept, and it has been developed in order to implement it in future automotive productions by also studying the feasibility of the process in mass-productions.



Figure 27. Fraunhofer® IPT 3D-printed Door Hinge

For what concerns racing applications, AM technologies are widely used both for prototyping and structural applications. For example, Selective Laser Sintering (SLS) and Stereolithography (SLA) are used primarily for the manufacturing of the aerodynamic parts required for testing new car designs. Current regulations require teams to perform all wind tunnel testing on a 60% scale model car, so SLS and SLA systems are used to create the required high-precision scale components. The used materials are usually AlSi10Mg or composites.

Recently, the FIA® had officially added the Scalmalloy to the list of approved materials to be used in AM for the Formula 1® championship. This material is made up by an Al-Sc-Mg alloy that provides high mechanical properties when used in AM processes. Thanks to its high resistance to stresses and its low weight and density, it can be used for multiple applications. Generally, it is mainly used in L-PBF processes in order to build aerodynamic elements such as the front wing, the air scoops, the wind channels on the car floor and the side mirrors. Moreover, it can also be used with DED processes to add aerodynamics features to already present surfaces made up of composite materials (such as carbon fibre).

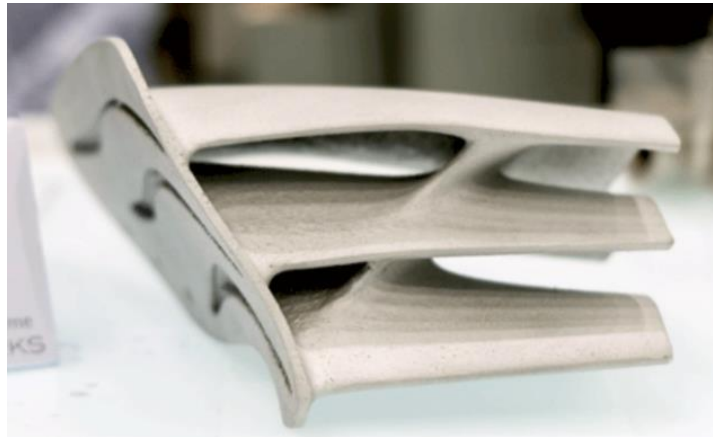


Figure 28. F1 Car 3D-printed Front Wing (Scalmalloy)

Among all the teams competing in the championship, Alpine® F1 Team is one of the most active in terms of AM technology exploitation. In particular, they use AM technologies in order to improve the energy and fluid management thanks to titanium 3D-printed hydraulic accumulators. The team has chosen the LaserForm Ti Gr23 (A) material in order to build the component. The AM technique allowed to maximize the length of the dampening coil while packaging complete functionality within a restricted space (possible thanks to adjacent wall sharing). The chosen process is DMP (Direct Metal Printing) that allowed to obtain smooth walls preventing pressure fluctuations of the fluid in the system, ensuring the best energy absorption and release in any operating condition.



Figure 29. Alpine® F1 Team 3D-printed Heat Accumulator

4. Component Selection

Once all the main features regarding AM technologies have been identified, it is possible to check their effective influence on a specific real-life application. In particular, in order to evaluate the main benefits and criticalities of these processes, the selected components are belonging to the Tesla® Model 3 rear suspension assembly, also hosting the rear electric motor (eAxle®).

The case study has been identified keeping in mind all the improvements that AM technologies can provide to the manufacturing process and the vehicle operational efficiency, thanks to a decreased weight, lower part count and higher mechanical properties that can result in improved autonomy and handling. Moreover, the Tesla® Model 3 can be considered as a high segment vehicle, making AM costs less impactful on the final purchasing price, even if some further evaluations are needed for the manufacturing volumes.

The vehicle chassis is hosting the battery pack and the inverters, placed between the front and rear suspension assemblies, where the two main electric motors are mounted. The rear suspension is following a multi-link configuration, while the front one follows a double wishbone strut. In particular, the assemblies are fulfilling two main requirements: improving vehicle handling and comfort and providing a support structure for the electric motors. The multi-link configuration in the rear vehicle end allows to obtain camber recovery by roll angle and longitudinal flexibility without undesirable toe angle variations. Moreover, in case of driving axles, it also allows to increase the wheels toe-in angle as a function of the traction force, enabling the so called *torque steering* and increasing the design freedom for the above mentioned axles.

Considering the two suspension struts:

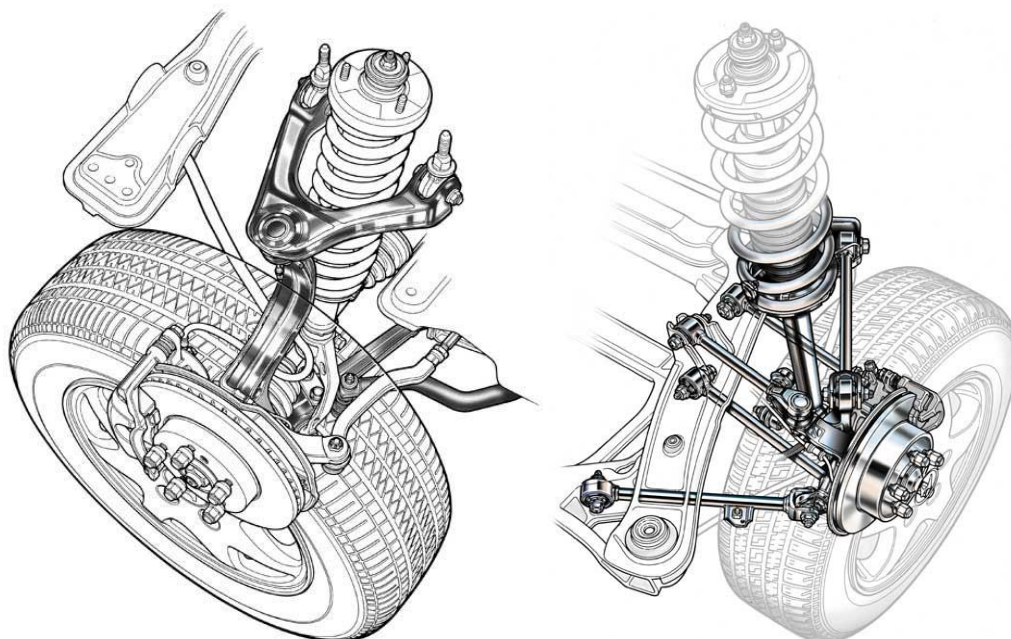


Figure 30. Double Wishbone Strut vs. Multi-link Strut

The rear suspension assembly is represented below:



Figure 31. Rear Suspension Assembly (Top View)

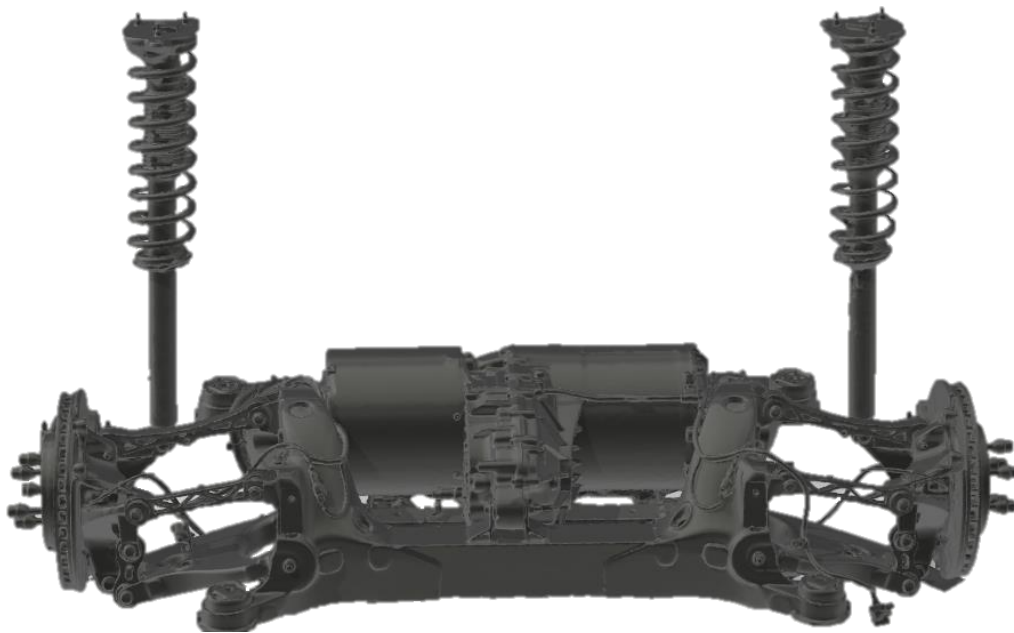


Figure 32. Rear Suspension Assembly (Front View)

From figures above, it is evident how the two multi-link configurations hosting the suspensions' springs and dampers are connected together by the middle frame that also provides a supporting structure for the electric motor. That specific connection element will represent the focus of the presented analysis. In particular, the main efforts will be pointed towards a correct topology optimization process, keeping in mind the most suitable material to be used in terms of mechanical properties and manufacturing costs, which could result in further LCA and efficiency improvements.

The initial steps are mainly related to the evaluation of the main dimensions and of the main loads acting on the frame. In particular, it will be possible to start from an approximation of the element providing the correct dimensions and, by means of a specialized software, to find a suitable generative design to be further optimized also keeping in mind all the loads acting on the frame.

The vehicle main dimensions are:

- **Length** → 4'694 mm
- **Width** → 1'849 mm
- **Height** → 1'443 mm

In order to evaluate the main suspension assembly dimensions, it is possible to consider a 1:30 scale representation provided in Tesla®'s open source patents^[19]:

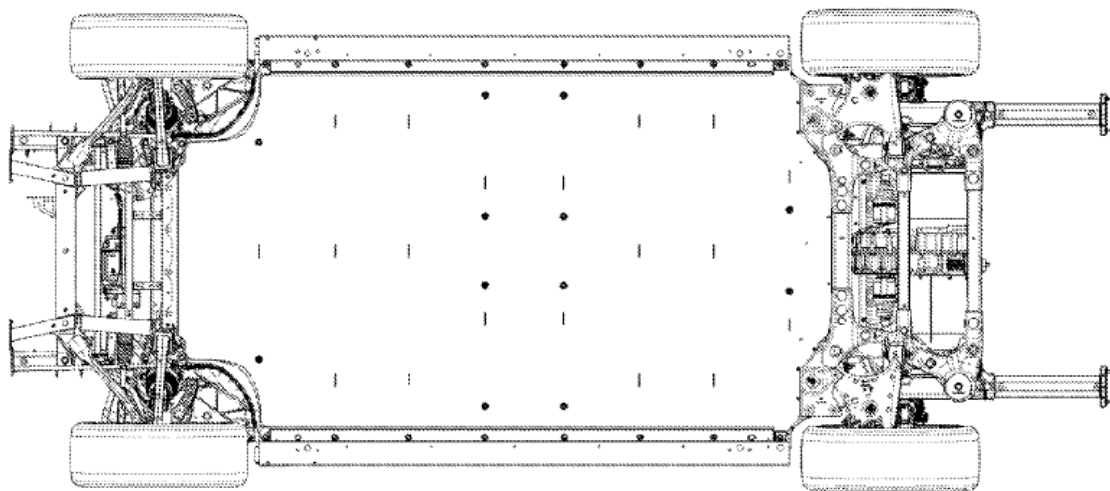


Figure 33. Tesla® Model 3 Chassis US8424960 [19]

From the technical drawing provided in *Figure 33*, it is possible to consider the main rear suspension assembly dimensions. In particular, it is only sufficient to evaluate what are the main positions for the attachment points to the frame in order to start the generative design process followed by the topology optimization one.

Once all the specific dimensions have been found, it is possible to proceed to the realization of the rear subframe CAD model that will be later implemented in Altair® Inspire environment to start the optimization process. As the previous figure highlights, the selected component is characterized by the presence of three horizontal beams where the electric motor is placed. This configuration is only present in the Dual Motor configuration, which provides an electric motor for each axle, making it possible to deploy an electric AWD vehicle with higher weight (1819 kg) and longer driving range (524 km) with respect to the standard version.

Considering the dimensions taken from the different patents' technical drawings and properly scaled to meet the real ones, the final technical draft used to build the 3D CAD model is the one represented in the drawing below.

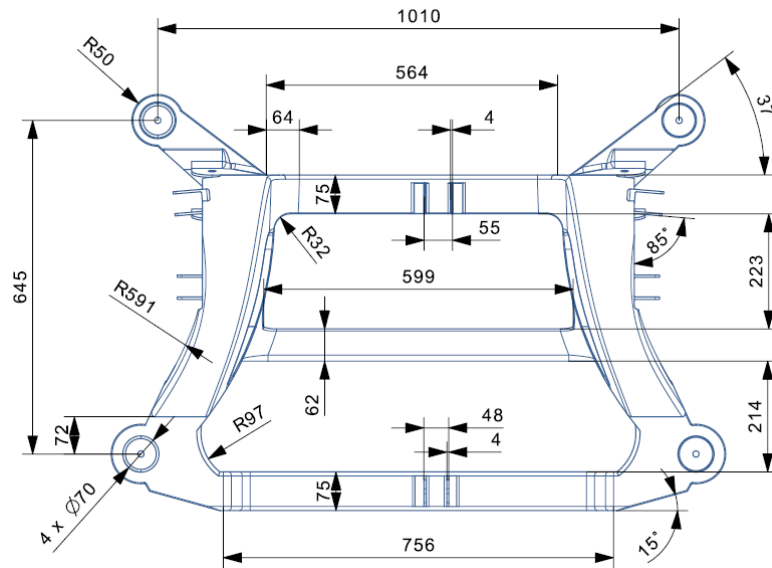


Figure 34. Rear Subframe Technical Drawing (Top View)

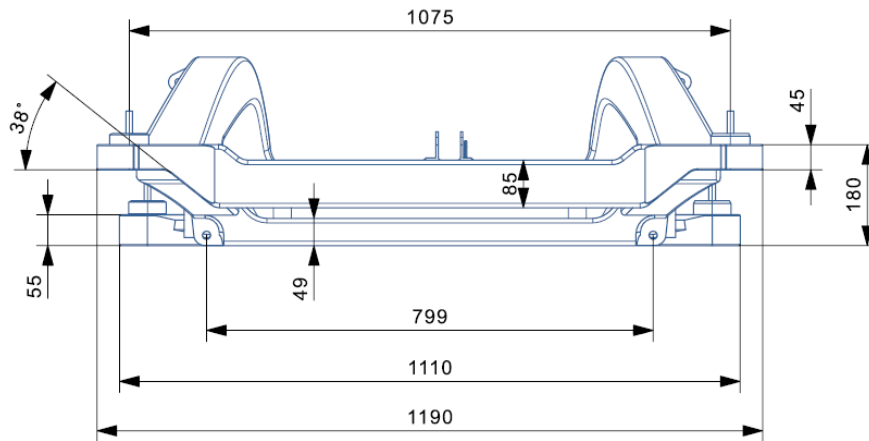


Figure 35. Rear Subframe Technical Drawing (Front View)

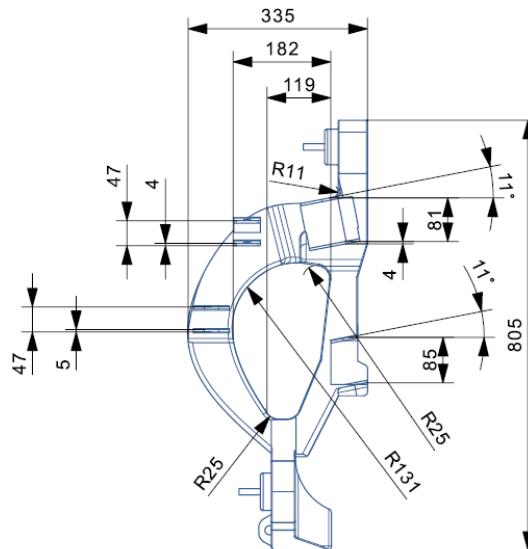


Figure 36. Rear Subframe Technical Drawing (Lateral View)

Once all the dimensions present in the technical drawing have been considered, the CAD model developed in Siemens® NX environment is the following one:

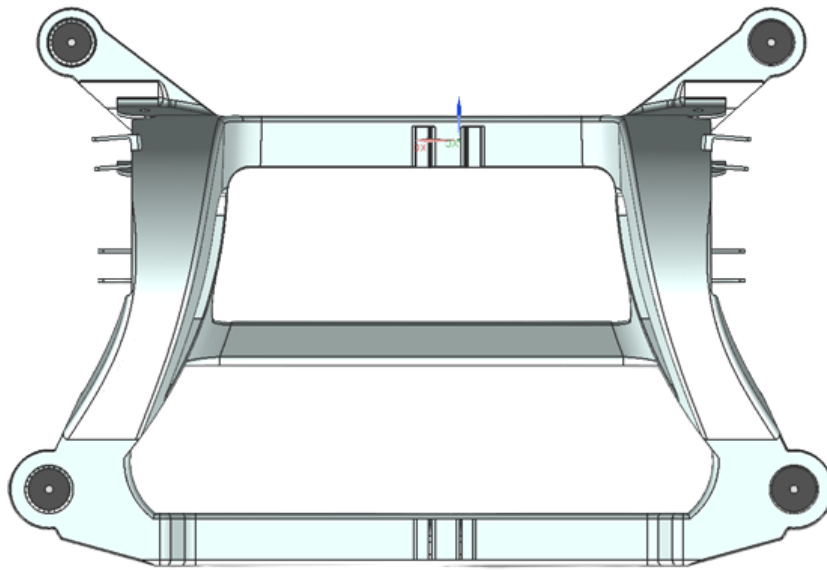


Figure 37. Tesla® Model 3 Rear Subframe (Top View)

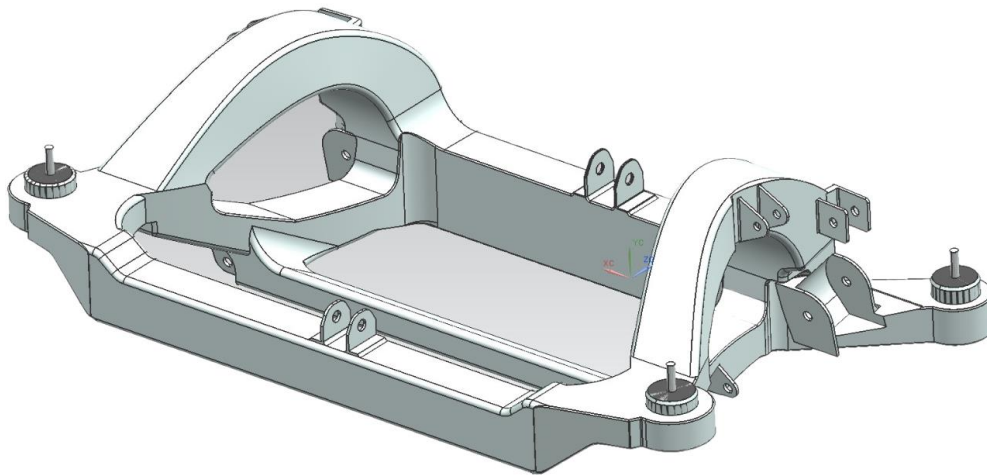


Figure 38. Tesla® Model 3 Rear Subframe (Isometric View)

From *Figure 38*, it is possible to better understand what the main geometrical features of the selected component are. The lateral sections are following a curved profile and they are generally thicker than all the other sections, mainly due to the fact that they will have to sustain the loads coming from the vertical, lateral and tangential forces and torsional moments coming from the multi-link suspension rods and the electric motor displacements.

The rear subframes used in all the Tesla® Model 3 models are made up of hollow tubes and brackets welded together and having a thickness of 1.2÷1.6 mm and 4÷5 mm, respectively. Moreover, the used materials are steels for structural applications such as ASTM A500 Grade A, corresponding to AISI 1025 (or AISI 1026) steels and the overall subframe weight is around 24 kg.

The AISI 1025 chemical composition is provided in the table below:

Table 4. AISI 1025 Chemical Composition

Element	Content [%]
Iron (Fe)	<i>99.03 ÷ 99.48</i>
Carbon (C)	<i>0.220 ÷ 0.280</i>
Manganese (Mn)	<i>0.30 ÷ 0.60</i>
Sulfur (S)	<i>≤ 0.050</i>
Phosphorous (P)	<i>≤ 0.040</i>

The mechanical properties are the following ones:

Table 5. AISI 1025 Mechanical Properties

Tensile Strength	<i>440 MPa</i>
Yield Strength	<i>370 MPa</i>
Shear Modulus	<i>80 GPa</i>
Elastic Modulus	<i>190 ÷ 210 GPa</i>
Poisson's Ratio	<i>0.27 ÷ 0.30</i>
Density	<i>7.858 g/cm³</i>
Elongation at Break	<i>15.00 %</i>
Thermal Expansion Coefficient (α)	<i>12.1 $\mu\text{m}/\text{m}\cdot^{\circ}\text{C}$</i>
Thermal Conductivity (λ)	<i>51.9 W/m·K</i>

The AISI 1025 is a particular steel used for machinery parts, structural components and tool/die applications. It provides good machinability and it is not present in powders, but it is sold in sheets, tubes or billets and, therefore, it cannot be used in AM applications. It is then important to refer to an equivalent material that is offering similar properties to AISI 1025 and that can be used in the additive manufacturing field. One material that can be selected is the SS 316L, a stainless steel referred as an iron-based Ni-Cr alloy which shows good mechanical properties and a good corrosion resistance up to 400 °C. Its chemical composition is the following one:

Table 6. SS 316L Chemical Composition

Element	Content [%]
Iron (Fe)	<i>68.47 ÷ 73.5</i>
Chromium (Cr)	<i>16.5 ÷ 18.5</i>
Nickel (Ni)	<i>10 ÷ 13</i>
Carbon (C)	<i>≤ 0.03</i>

Considering the SS 316L mechanical properties:

Table 7. SS 316L Mechanical Properties

Tensile Strength	<i>515 MPa</i>
Yield Strength	<i>205 MPa</i>
Yield Strength after L-PBF	<i>575 MPa</i>
Shear Modulus	<i>80 GPa</i>
Elastic Modulus	<i>195 GPa</i>
Poisson's Ratio	<i>0.27 ÷ 0.30</i>
Density	<i>8 g/cm³</i>
Elongation at Break	<i>15.00 %</i>
Thermal Expansion Coefficient (α)	<i>16 $\mu\text{m}/\text{m}\cdot^{\circ}\text{C}$</i>
Thermal Conductivity (λ)	<i>16.3 W/m·K</i>

From the analysis of the mechanical properties it is then reasonable to consider the SS 316L as a good substitute for AISI 1025 to be used in AM applications.

5. Load Cases

Before starting the topology optimization process in Altair® Inspire environment, it is necessary to evaluate which are the main loads acting on the vehicle rear subframe. In particular, four main scenarios have been selected and analysed, such as maximum acceleration, braking in capsized limits, sharp cornering and passage over a road bump.

5.1 Maximum Acceleration

In order to evaluate the main loads acting on the rear subframe during maximum acceleration conditions, the analysed scenario takes into account an acceleration phase performed on a quarter mile (400 m) drag strip. By knowing the initial speed and time, the covered distance and the time required to cover it (12.2 s) it is possible to evaluate the maximum vehicle acceleration \ddot{x} . In order to perform the different load calculations, it is necessary to apply the equation of motion:

$$s = v_0 \cdot t_0 + \frac{1}{2} \cdot \ddot{x} \cdot t_1^2$$

Where:

- $v_0 = 0$ km/h (initial speed)
- $t_0 = 0$ s (initial time)
- $s = 400$ m (total covered distance)
- $t_1 = 12.2$ s (time required to cover the quarter mile distance)

The final value for maximum acceleration is given by:

$$\ddot{x} = \frac{2 \cdot s}{t_1^2} \cong 5.37 \text{ m/s}^2$$

It is possible to notice that the maximum acceleration provided by the Tesla® Model 3 is much higher with respect to the one of traditional ICE-based vehicles, thanks to the presence of two electric motors enabling AWD mode and also thanks to the higher power density that electric motors can provide with respect to the one developed by ICEs (due to their higher efficiency).

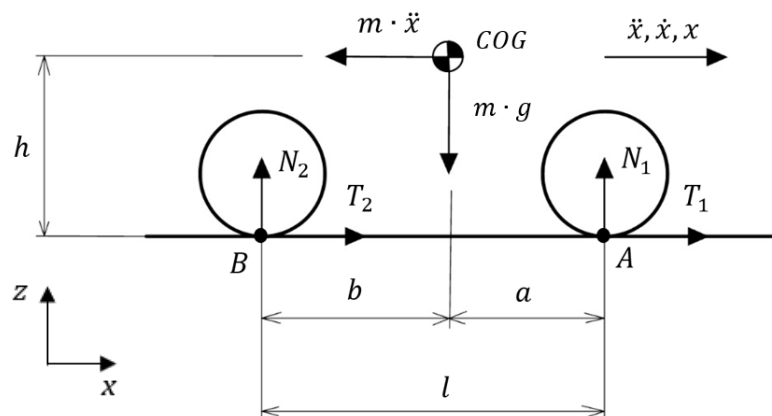


Figure 39. Vehicle Lateral Free-Body Diagram

Where:

- $l = 2875 \text{ mm}$ (wheelbase)
- $b = a = 1437.5 \text{ mm}$ (rear/front axle distance from Center Of Gravity, COG)
- $h = 200 \text{ mm}$ (COG height)
- $m = 2119 \text{ kg}$ (Tesla® Model 3 curb mass + 4 x 70 kg occupants + luggages)
- $\ddot{x} = 5.37 \text{ m/s}^2$ (maximum acceleration)
- $g = 9.81 \text{ m/s}^2$ (gravitational constant)
- $N_1, T_1 =$ normal/tangential forces between tire and ground (front axle)
- $N_2, T_2 =$ normal/tangential forces between tire and ground (rear axle)

The equilibrium equations for the system are the following ones:

$$\uparrow) N_1 + N_2 = m \cdot g$$

$$\rightarrow) T_1 + T_2 = m \cdot \ddot{x}$$

$$A) N_2 \cdot l = m \cdot g \cdot a + m \cdot \ddot{x} \cdot h$$

From Tesla®'s datasheets, it is possible to assume that there is a 50% - 50% weight distribution between front and rear axles, meaning that the COG will be exactly in the middle of the wheelbase and the normal components N_1 and N_2 acting respectively on the front and rear axles are equal. Moreover, due to the uniform distribution of weights between the axles and since the Dual Motor configuration provides an AWD vehicle, it is possible to consider the presence of both the tangential forces T_1 and T_2 (equal one to the other) because all the wheels are considered as driving wheels.

The different forces acting on the rear subframe will be:

$$N_2 = m \cdot \left(g \cdot \frac{a}{l} + \ddot{x} \cdot \frac{h}{l} \right) \cong 11185.3 \text{ N}$$

$$T_2 = T_1 = m \cdot \frac{\ddot{x}}{2} \cong 5689.5 \text{ N}$$

The remaining normal force acting on the rear axle will be given by:

$$N_1 = m \cdot g - N_2 \cong 9602.1 \text{ N}$$

Comparing the forces acting on the two axles, it is possible to affirm that the hypothesis where there is roughly a 50% - 50% weight distribution is still valid. More precisely, the distribution provides a 51% weight on the rear axle and 49% weight on the front one when dealing with acceleration manoeuvres, due to the vehicle "squatting" behaviour. All the loads found so far will be directly applied and distributed to each one of the four supports of the multi-link system rods.

5.2 Braking in Capsize Limits

The braking condition is very similar to the maximum acceleration one, with the only difference given by the fact that, instead of accelerating the vehicle, the driver is decelerating until locking the wheels. In particular, the experienced decelerations during this driving condition are generally higher than the ones provided in the previous case, so the applied loads will be consequently higher than the ones calculated above. These effects can be partially mitigated by the presence of regenerative braking and ABS (Antilock Braking Systems) since, thanks to these devices, the effects of tire locks will be sustained for a lower number of times and with a lower duration.

To perform the analysis of the load scenario, it is possible to consider the same vehicle free-body diagram present in *Figure 39* and perform the same calculations as before. The only difference in this case will be given by the acceleration sign and module. In particular, the maximum deceleration for a Tesla® Model 3 Dual Motor can be evaluated referring to experimental tests performed in 2018 by Auto Bild® Sportscars, where the vehicle is slowed down from 200 km/h to zero in about 6.7 seconds, covering a distance of 159.8 meters and providing maximum decelerations of -9.7 m/s^2 .

The obtained results will be the following ones:

$$N_2 = m \cdot \left(g \cdot \frac{a}{l} - |\ddot{x}| \cdot \frac{h}{l} \right) \cong 8963.8 \text{ N}$$

$$T_2 = T_1 = m \cdot \frac{|\ddot{x}|}{2} \cong 10277.2 \text{ N}$$

$$N_1 = m \cdot g - N_2 \cong 11823.6 \text{ N}$$

In particular, the tangential force experienced during emergency braking operations cannot be considered as directly applied to the multi-link supports, since they are characterized by a lever arm given by the length of the suspension system's rods that makes it possible to consider it as torque C_T . Following some calculations that are taking into account the technical drawings, the width of the car and the tire dimensions (with a standard 235/45 R18 98 Pirelli® P ZERO), it is possible to consider a lever arm t_L with an average length of about 230 mm that establishes a torque with an axis perpendicular with respect to the support axis. The final value for the torque to be considered will be given by the product between tangential forces and lever arm.

$$C_T = T_1 \cdot t_L = T_2 \cdot t_L \cong 295.5 \text{ Nm}$$

Having a look at the results, it is possible to see how the normal loads acting on the axles are no longer similar, but there is a major difference between the front and rear loads. In particular, the normal loads acting on the front axle are higher than the loads acting on the rear one due to the vehicle "diving" behaviour during braking operations. The opposite happens when the vehicle is accelerating, where the "squatting" behaviour provides a higher load on the rear axle.

During braking operations, the only loads higher than the ones during acceleration manoeuvres are the tangential ones, which are roughly doubled with respect to the previous ones. It is therefore possible to consider a load case merging the two behaviours, considering the worst case for normal loads taken from a maximum acceleration condition and the worst case for tangential loads taken from a braking in capsize limit condition.

For sake's of completeness, it is also necessary to consider an additional load that is provided to the rear frame by the presence of the rear electric driveline directly mounted on the subframe, accounting for about 95 kg due to the presence of rotor, stator, housing and differential, contributing to additional 932 N distributed on the central horizontal beam.

Once the vehicle longitudinal dynamics have been analysed, the next step before implementing all the load cases and the CAD model in Altair® Inspire environment is related to the evaluation of the vehicle dynamics during sharp cornering conditions and during the passage over a road bump.

5.3 Sharp Cornering

In order to properly evaluate all the loads acting on the rear subframe and to perform an accurate optimization process, it is necessary to consider the vehicle lateral dynamics in sharp cornering conditions, here intended as the limit scenario. In particular, the limit case has been set to make the vehicle perform a 80 meters radius curve at a speed of 100 km/h. In this way, by knowing the vehicle centripetal acceleration \ddot{x}_y it will be possible to calculate the lateral force acting on it and to consider the torsional moment resulting from the rolling of the chassis whenever a yaw moment is applied by means of the steering wheel. It has to be noted that the torsional moment, also called rolling moment, is no longer applied to the vehicle COG, but to the vehicle Roll Center (RC).

Taking into account the radius of curvature and the vehicle speed, the evaluation of the centripetal acceleration will be performed as follows:

$$\ddot{x}_y = \frac{v^2}{R} = \frac{\left(\frac{100}{3.6}\right)^2}{80} \cong 9.65 \text{ m/s}^2 \cong 0.98 \cdot g$$

The loads acting on the vehicle rear axle can be evaluated by considering also in this case a free-body diagram only taking into account the rear axle, meaning that the weight of the car can be halved.

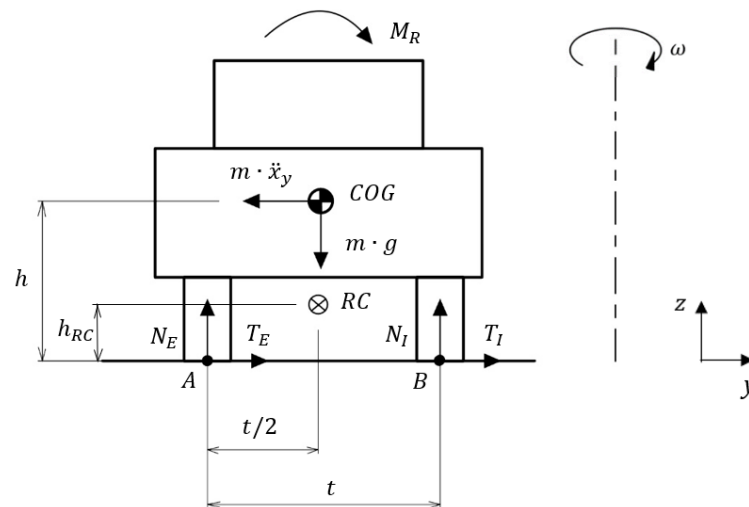


Figure 40. Vehicle Rear Free-Body Diagram

Where:

- $t = t_R = t_F = 1580 \text{ mm}$ (vehicle track)
- $h_{RC} = 100 \text{ mm}$ (roll center height)
- M_R = rolling moment (around RC)
- $\ddot{x}_y = 9.65 \text{ m/s}^2 = 0.98 \cdot g$ (centripetal acceleration)
- N_E, T_E = normal/tangential forces between tire and ground (external)
- N_I, T_I = normal/tangential forces between tire and ground (internal)

Due to the unavailability of information related to the experimental value for the roll center height, knowing that generally the rear RC height for an electric passenger car ranges between 50 ÷ 150 mm, an average value for h_{RC} has been considered and set to 100 mm.

In this specific case, the loads are belonging to the same axle and they are only distinguished in external (acting on the outer tire) and internal (acting on the inner wheel).

The equilibrium equations for the system are the following ones:

$$\uparrow) N_E + N_I = \frac{m}{2} \cdot g$$

$$\rightarrow) T_E + T_I = \frac{m}{2} \cdot \ddot{x}_y$$

$$RC) M_R + (N_E - N_I) \cdot \frac{t}{2} = \frac{m}{2} \cdot \ddot{x}_y \cdot (h - h_{RC})$$

In this case, the external and internal forces are not equal since they depend on the actual cornering stiffness of each tire that cause a load transfer between outer and inner wheels (+ for outer, - for inner tires). Since few data are available for what concerns the tires' cornering stiffness, as a first approximation and for sake's of simplicity, it is possible to consider the model as completely rigid and neglect the load transfer between inner and outer wheels. Thanks to this assumption, the values of forces are no longer $N_E > N_I$, but they become $N_E = N_I$.

In this way, the final values for the forces and moment present in the equilibrium equations will become:

$$N_E = N_I = \frac{m}{4} \cdot g \cong 5196.8 \text{ N}$$

$$T_E = T_I = \frac{m}{4} \cdot \ddot{x}_y \cong 5112.1 \text{ N}$$

$$M_R = T_E \cdot h = T_I \cdot h = \frac{m}{4} \cdot \ddot{x}_y \cdot (h - h_{RC}) \cong 511.2 \text{ Nm}$$

In this case, the worst case is given by the tangential forces (directed along the y-axis and applied to the rear subframe) and the rolling moment (causing a torsion of the subframe). The normal loads are not considered as worst cases since they are much lower with respect to the ones experienced by the rear subframe during maximum acceleration conditions.

Once the previous three limit cases have been evaluated and the different loads and moments acting on the rear subframe have been identified, it is possible to proceed to the last load case scenario that will be considered simultaneously to the other identified ones in order to evaluate the overall load condition and component's performances after the topology optimization and FEM analysis phases.

5.4 Passage Over a Road Bump

Another important source of excitation is given whenever the vehicle passes over a road bump at medium-high speeds. In particular, the forces acting on the rear subframe are related to the normal force established between the tire contact patch and the ground.

Moreover, every time the vehicle encounters an obstacle, other than a normal force causing a vertical displacement, it is also present a longitudinal force that is generated by the presence of the obstacle and that moves the tire in the opposite direction of motion. However, the latter longitudinal contribution can be neglected in this case since it will be negligible with respect to the normal contribution.

Considering the observed situation, it is possible to take into account the Tesla® Model 3 passing over a road bump having a radius of curvature of about 18.4 m with a speed of 40 km/h. From the vehicle free body diagram, it is possible to notice that the main forces that are acting on the rear axle are the normal force between tire and ground, the vehicle weight force and the centripetal force due to the acceleration generated as soon as the vehicle overcomes the bump. In particular, since the analysis is limited to the rear axle, the vehicle weight will be halved following the 50% - 50% weight distribution.

The rear axle free body diagram will be:

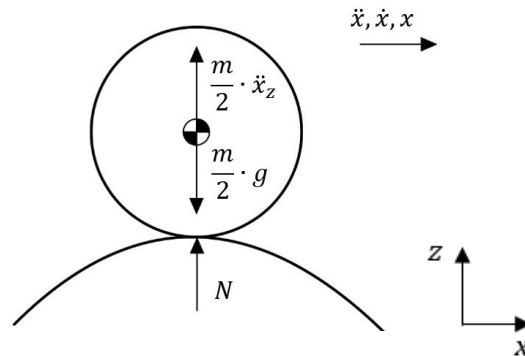


Figure 41. Rear Axle Free Body Diagram

And the calculations are the following ones:

$$\uparrow) \frac{m}{2} \cdot g = N + \frac{m}{2} \cdot \ddot{x}_z$$

$$N = \frac{m}{2} \cdot g - \frac{m}{2} \cdot \frac{v^2}{R} = 2931.4 \text{ N}$$

Considering all the values of forces previously identified and belonging to the maximum acceleration, braking in capsized limit and sharp cornering conditions, it is evident how the impact of the forces belonging to the case in which the vehicle is passing over a bump is minor with respect to all the other ones. In synthesis, the main contributions will be given by the three previously analysed cases, which will make it possible to proceed to the topology optimization of the rear subframe.

6. Topology Optimization

As already said, the topology optimization process is fundamental to establish the best possible material distribution in order to improve the component performances while decreasing its weight, providing material only where necessary.

The whole procedure is performed in Altair® Inspire environment, a software that allows to perform topology optimization processes starting from a defined 3D CAD model. In this particular case, the rear subframe model has been previously defined from different open source patents and technical drawings. The optimization process is an iterative procedure that allows to check the material disposition according to its properties and depending on the loads and torques applied to the component.

First of all, the 3D CAD model of the Tesla® Model 3 rear subframe has to be imported in the optimization software in order to be analysed. In this specific phase it is fundamental to check the component geometry to avoid the presence of voids or disconnected sections that can result in inconsistencies in the final results. Once this preliminary check is successful, it is possible to proceed to the evaluation of the different constraints, loads and torques to be applied to the original part.

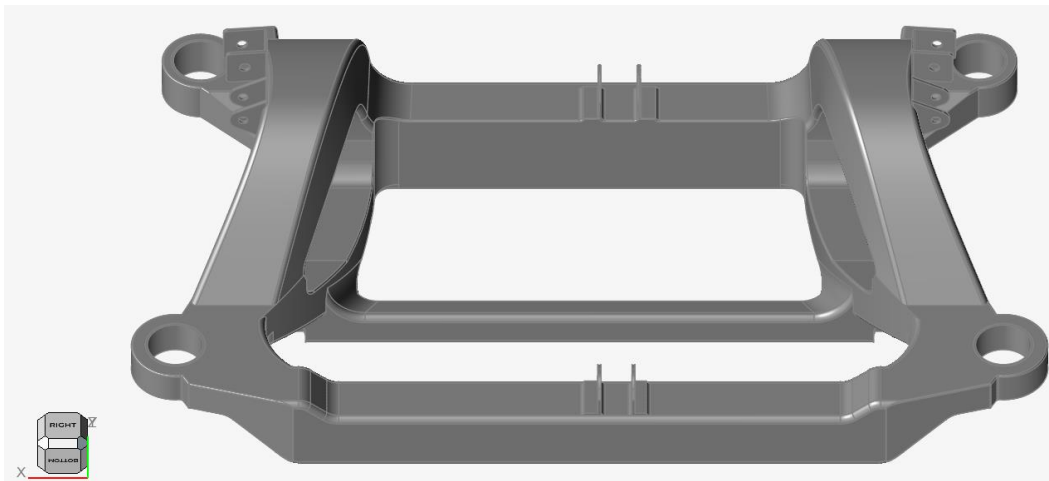


Figure 42. Rear Subframe 3D CAD Model on Altair® inspire

Considering the subframe geometry, it is evident how the main constraints can be placed on the four edges that provide the connection between the rear subframe and the vehicle underbody. To this extent, in order to effectively secure the part to the vehicle it is possible to use bolts and rubber joints to damp down any possible vibration coming from the electric motor and the road irregularities.

A practical way to represent the link between these elements in Altair® is given by using the *Partition* command applied to the connection holes and applying a constraint in each of them. Thanks to this command, it is possible to divide a region in design and non-design spaces, so that the prescribed geometry remains fixed and will not be affected by the optimization process. The parts fixed by the partition command can be easily detected since they are the ones remaining of a grey colour when the design space is created and defined by a brown colour, as it can be seen in the figure below.



Figure 43. Partition Areas in the Design Space

Once the main elements to be constrained have been defined, it is possible to apply to them the real constraints that will make it possible to fix them during the optimization process while the other loads are applied. In this case, as already said, the constraints will be applied to the four holes that have been previously partitioned since they are the only points of connection between the rear subframe and the vehicle underbody. The defined supports will be highlighted in red and they will be located in the middle of the holes.



Figure 44. Constraints Locations

Once the supports have been defined, it is possible to proceed to the definition of the different load cases according to the previously performed evaluation of the three different scenarios. In particular, there will be three main load cases, one given by the combination of acceleration and deceleration operations and the other two given by sharp cornering ones. Considering the main values found from the equilibrium equations, it is possible to define several types of loads, each one applied according to its specific direction.

The considered loads are the following ones:

- **Acceleration/Deceleration:**

$N_2 = 11185.3 \text{ N}$ (maximum normal load in acceleration, along the z-axis)

$T_2 = T_1 = 10277.2 \text{ N}$ (maximum tangential load in deceleration, along the x-axis)

$C_T = 295.5 \text{ Nm}$ (maximum tangential torque in deceleration, around the z-axis)

$P = 932 \text{ N}$ (motor weight force on the middle horizontal beam, along the z-axis)

- **Left/Right Sharp Cornering:**

$T_E = T_I = \pm 5112.1 \text{ N}$ (maximum lateral load in sharp cornering, along the y-axis)

$M_R = \pm 511.2 \text{ Nm}$ (rolling moment in sharp cornering, around the x-axis)

$P = 932 \text{ N}$ (motor weight force on the middle horizontal beam, along the z-axis)

As soon as the different forces and torques have been defined, it is possible to apply them to the subframe structure either directly or by means of connectors. In particular, connectors will be necessary for all the flanges hosting the multi-link suspension systems' rods, while the rolling torque and the electric motor weight force can be directly applied on the subframe horizontal beams. The connectors will be defined as can be seen in the figure below.

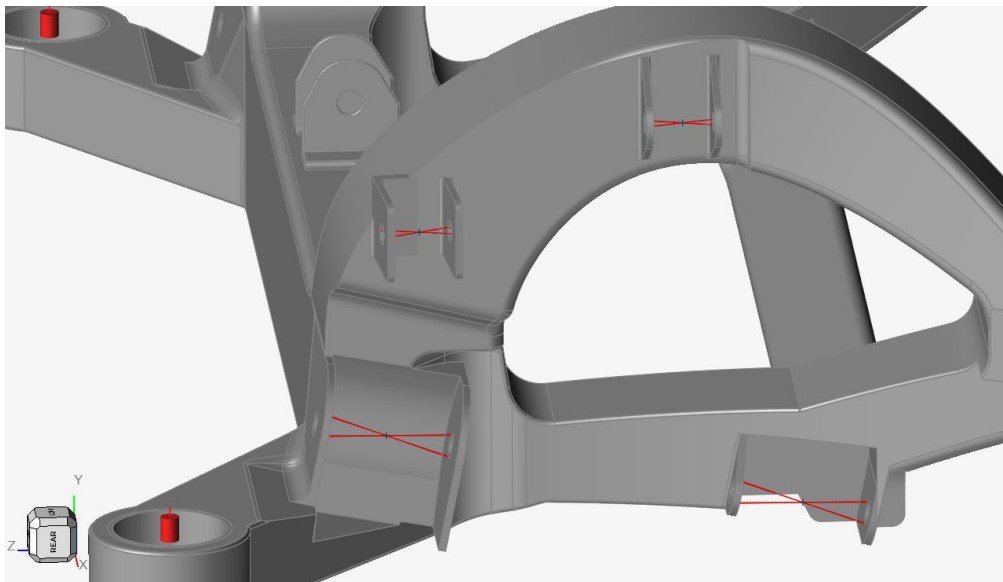


Figure 45. Connectors between Flanges

Considering the application of the loads belonging to the acceleration/deceleration load case, it is possible to define a total of four force vectors and four torques (for each side of the subframe) acting on the connectors between the four support brackets and an additional force vector applied as a distributed force all along the middle horizontal beam. The final configuration is the one represented in the following figure.

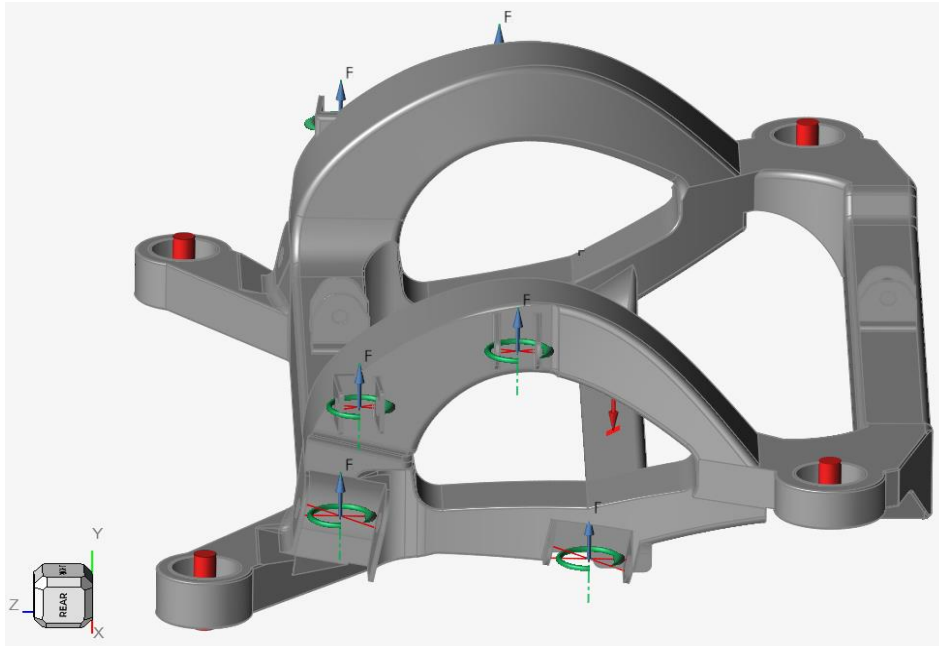


Figure 46. Force Distribution for the Acceleration/Deceleration Load Cases

In this case, the green vectors are representing the torques C_T established by the tangential forces T_2 experienced during maximum deceleration, the vertical blue vectors are representing the normal force N_2 experienced during maximum acceleration and the vertical red vector applied in the central horizontal beam represents the electric motor weight force.

The same operations can be made for the sharp cornering load case, where there will be a total of eight force vectors (for each side of the subframe) acting on the connectors, four rolling moments directly applied to the main horizontal beams and an additional force vector applied as a distributed force all along the middle horizontal beam. The forces and moments will be divided according to the cornering direction, so that there will be four forces applied for left corners, four forces for right corners and the torques that are following the same subdivision, so that there will be a couple of counter-rotating moments acting on the main horizontal beams according to the cornering directions.

From the figure below, it is possible to notice that the horizontal orange vectors are representing the tangential forces T_E (or T_1) experienced during right sharp cornering, the white horizontal vectors the tangential forces experienced during left sharp cornering, the vertical red vector applied in the central horizontal beam represents the electric motor weight force and the yellow and purple vectors represents the rolling moments that are directly transmitted to the main subframe horizontal beam during cornering operations due to torsions of the vehicle underbody.

In this case, we have to take into account the presence of two scenarios when dealing with sharp cornering, one for right corners and the other for left corners. The effects of the forces will be the same in both cases, but it will allow to have a more complete representation of the actual loading state. The main difference between the left and right corners will be the opposite direction of the tangential forces and the opposite sense of rotation of the moments applied on the subframe.

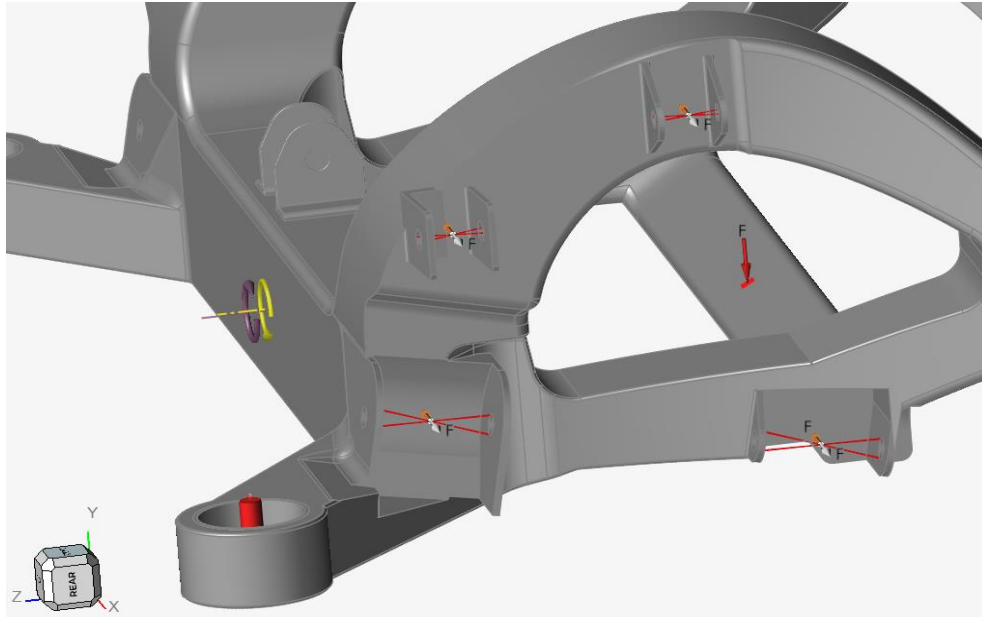


Figure 47. Force Distribution for the Left & Right Sharp Cornering Load Case

Considering all the loads and torques acting together, the final load scenario for the rear subframe will include the presence of twelve forces and four torques applied on the connectors between the flanges (for each side of the component), four counter-rotating torques applied to the main horizontal beams and a distributed weight force generated by the presence of the electric motor on the central beam.

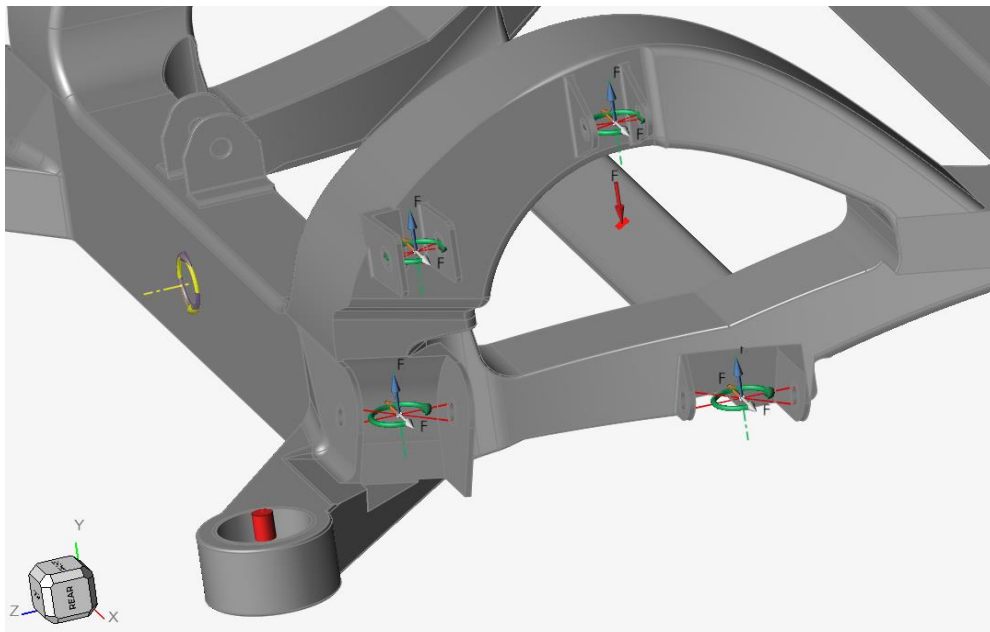


Figure 48. Final Load Scenario (All Load Cases Combined)

Once all the loads have been applied and the load cases have been defined, it is possible to proceed to the topology optimization considering the whole rear subframe as a single design space. The chosen materials for the design space considered for the main optimization are SS 316L, whose properties have been previously analysed, and Ti6Al4V.

In particular, TiAl64V is a Ti alloy used for structural purposes and for components that have to withstand high static and dynamic loads, other than being also resistant to medium-high temperature applications (400 °C). The main chemical properties for this Ti alloy are listed below:

Table 8. Ti6Al4V Chemical Composition

Element	Content [%]
Titanium (Ti)	90.0
Aluminium (Al)	5.5 ÷ 6.75
Vanadium (V)	3.5 ÷ 4.5
Iron (Fe)	≤ 0.30
Carbon (C)	≤ 0.10

The mechanical properties are:

Table 9. Ti6Al4V Mechanical Properties

Tensile Strength	1170 MPa
Yield Strength	827 MPa
Shear Modulus	45 GPa
Elastic Modulus	116.5 GPa
Poisson's Ratio	0.310
Density	4.429 g/cm ³
Elongation at Break	18.00 %
Thermal Expansion Coefficient (α)	8.82 $\mu\text{m}/\text{m}\cdot^{\circ}\text{C}$
Thermal Conductivity (λ)	6.7 W/m·K

Once the load cases, the design space and the materials have been identified, it is possible to proceed to the topology optimization directly starting the iterative simulation from the *Optimize* command on the Altair® toolbar. In this case, the main objective is to find a trade-off between stiffness maximization and mass minimization. To this extent, the mass targets have been set to reach around 40% of the design space volume and all the load cases (i.e. maximum acceleration, maximum deceleration and sharp cornering to the right/left) are simultaneously considered since they cannot be treated separately.

The considered condition includes the whole component as design space and all the loads acting together on the eight connection brackets.

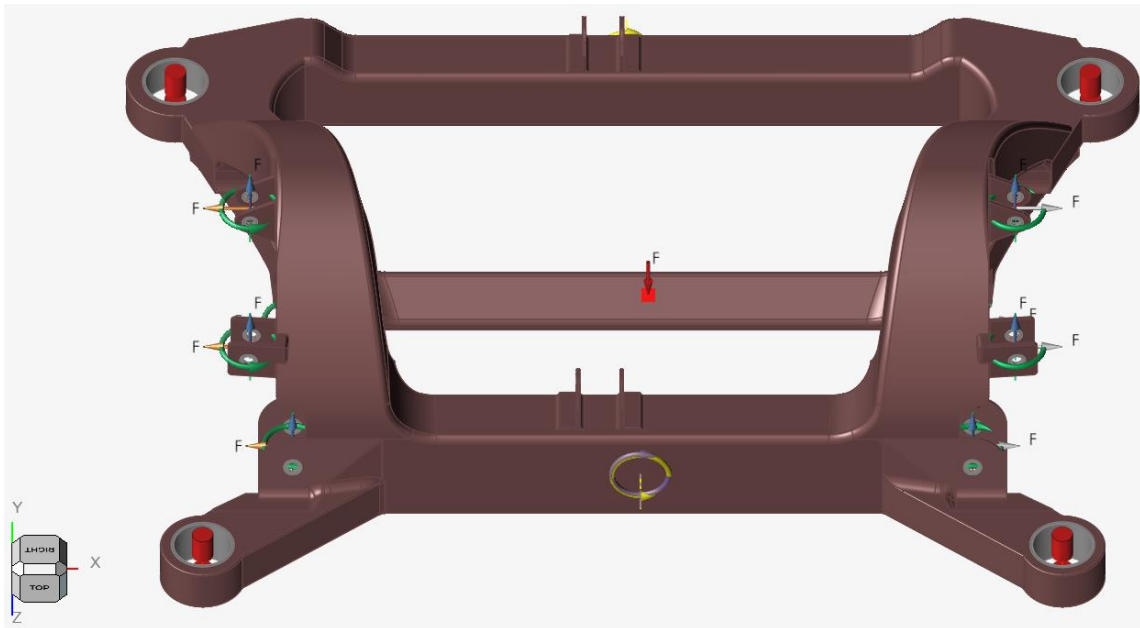


Figure 49. Subframe Design Space with Applied Loads

The final result with SS 316L material is represented below:

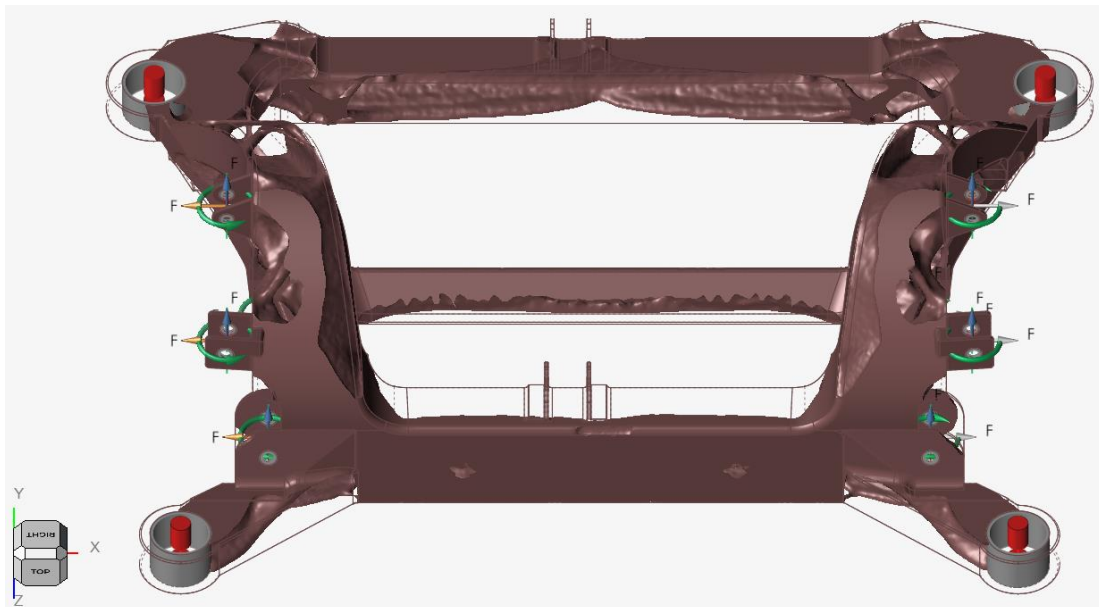


Figure 50. Rear Subframe Topology Optimization with SS 316L (Front View)

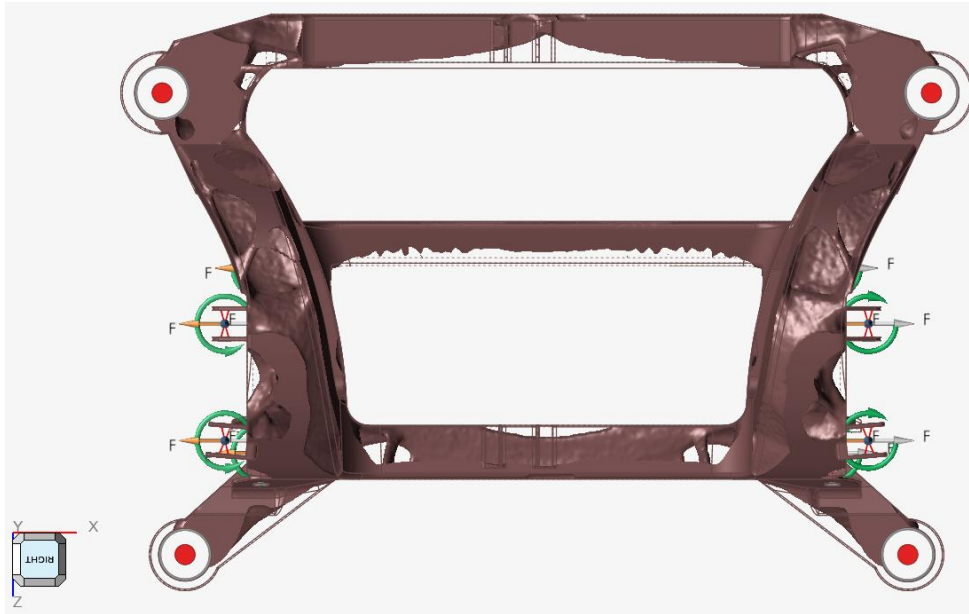


Figure 51. Rear Subframe Topology Optimization with SS 316L (Top View)

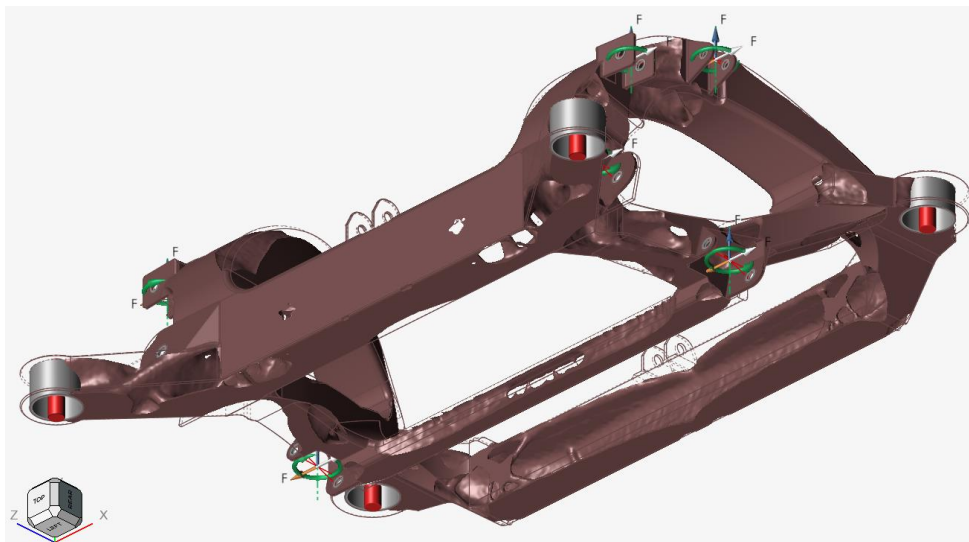


Figure 52. Rear Subframe Topology Optimization with SS 316L (Bottom View)

As the optimization is completed, it has to be noted that, according to the chosen material, the final component can be characterized by different shapes due to their different densities, yield strengths and elastic modules. So, for example, it is reasonable to assume that material characterized by high stiffness, such as Ti6Al4V, can provide optimizations with a lower amount of material and vice versa for materials with lower stiffness, such as SS 316L.

From the obtained results with SS 316L, it is possible to understand how the topology optimization allowed to improve the component performances by taking into account the prescribed load scenarios and applying material only where needed, switching from an initial volume of $3.054 \cdot 10^6 \text{ mm}^3$ to an optimized volume of $1.008 \cdot 10^6 \text{ mm}^3$, with a material saving of about 67% with respect to the original component. Consequently, since the material density remained the same, the weight before and after the optimization highlights a decreasing trend from 24 kg to 8.06 kg.

Once the final results with SS 316L is obtained, it is possible to fit the design space with the PolyNURBS curve that allows to obtain a smoother design and to proceed with the FEM analysis in order to evaluate the rear subframe mechanical stresses and displacements. The final component is obtained by selecting the *Fit* command in the *PolyNURBS* ribbon on the Altair® toolbar.

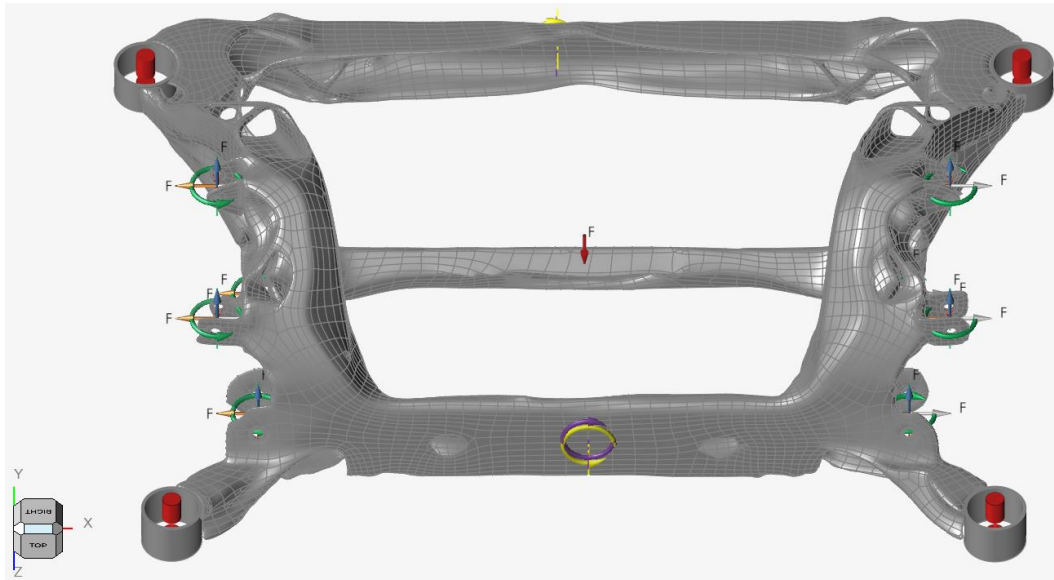


Figure 53. PolyNURBS Curve with SS 316L (Front View)

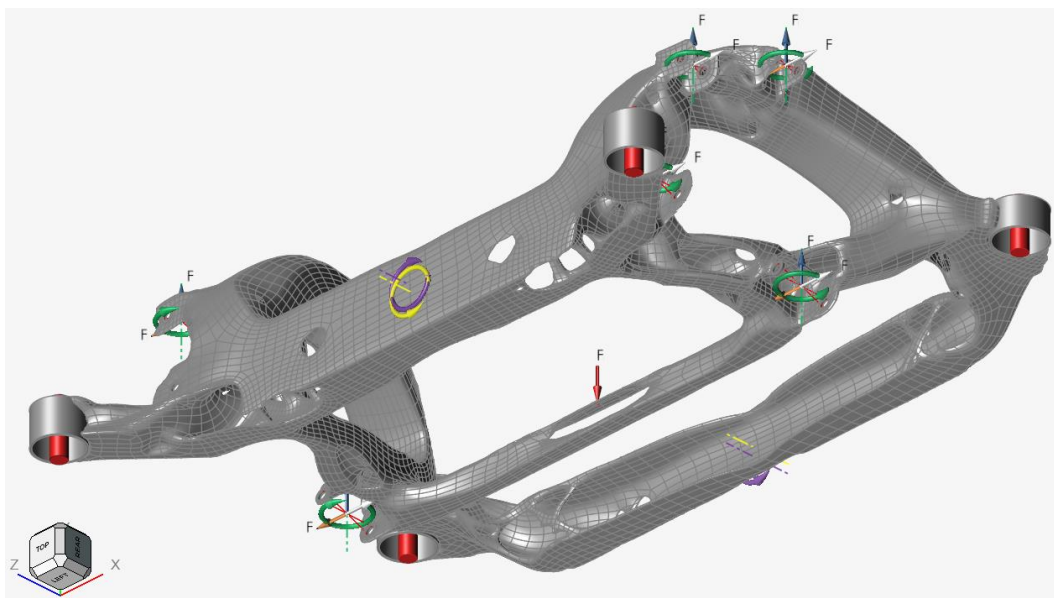


Figure 54. PolyNURBS Curve with SS 316L (Bottom View)

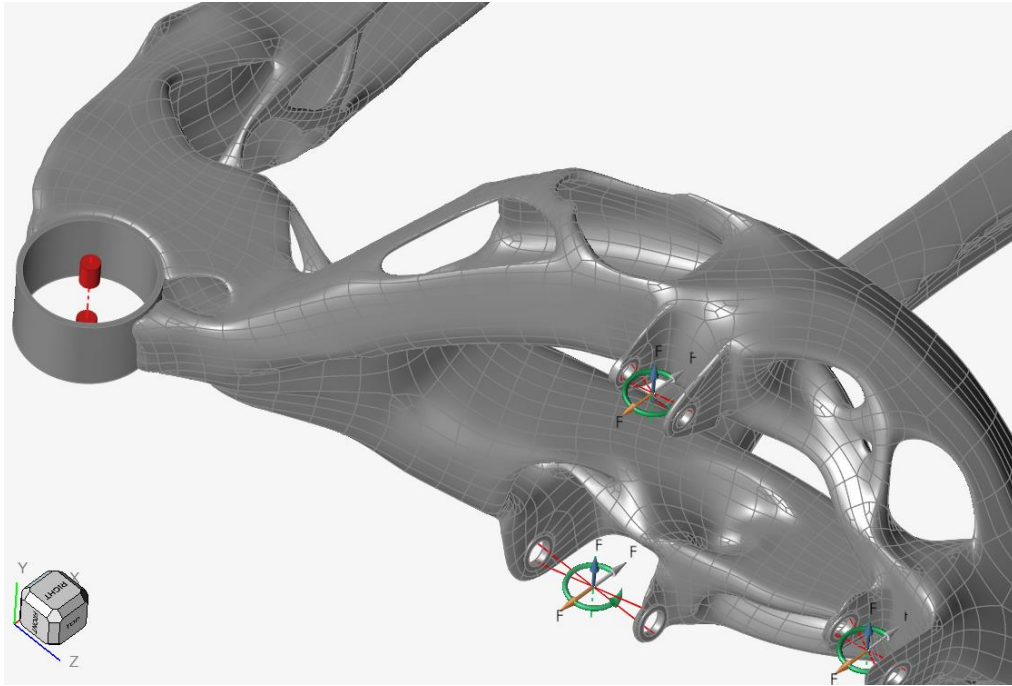


Figure 55. Detail of the Optimized Part with SS 316L (Top Side)

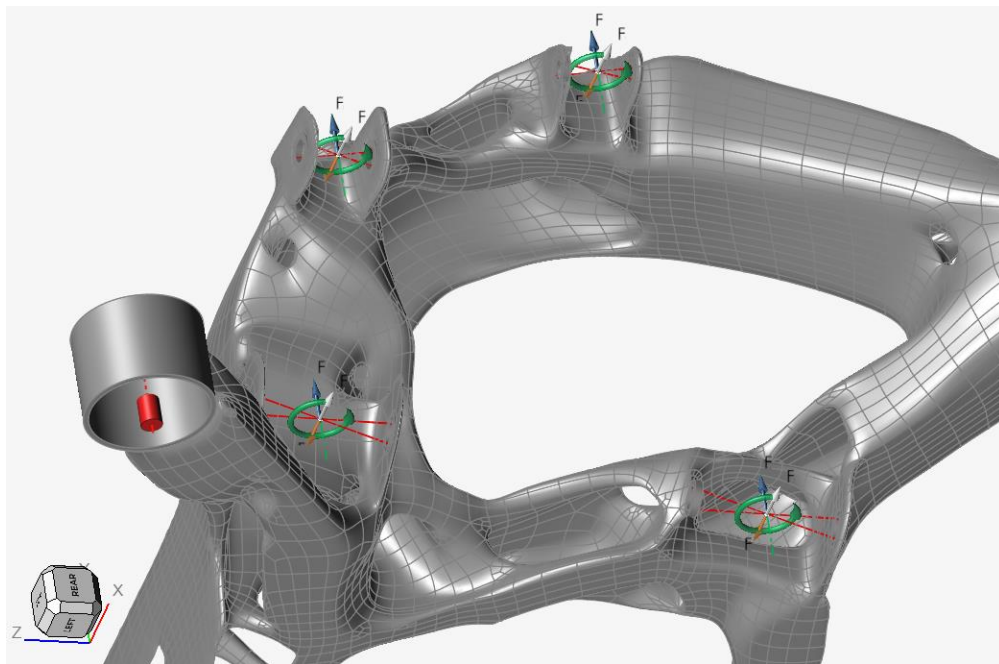


Figure 56. Detail of the Optimized Part with SS 316L (Bottom Side)

Considering now the obtained results with Ti6Al4V, it is possible to understand how the topology optimization allowed to further improve the component performances with respect to the ones obtained with SS 316L. In this specific case, by referring to the prescribed load scenarios and applying material only where needed, it has been possible to switch from an initial volume of $3.054 \cdot 10^6 \text{ mm}^3$ to an optimized volume of $4.397 \cdot 10^5 \text{ mm}^3$, with a material saving of about 74% with respect to the original component. Consequently, since the material density decreased to 4.429 g/cm^3 , the weight before and after the optimization highlights a decreasing trend from 13.53 kg to 3.48 kg.

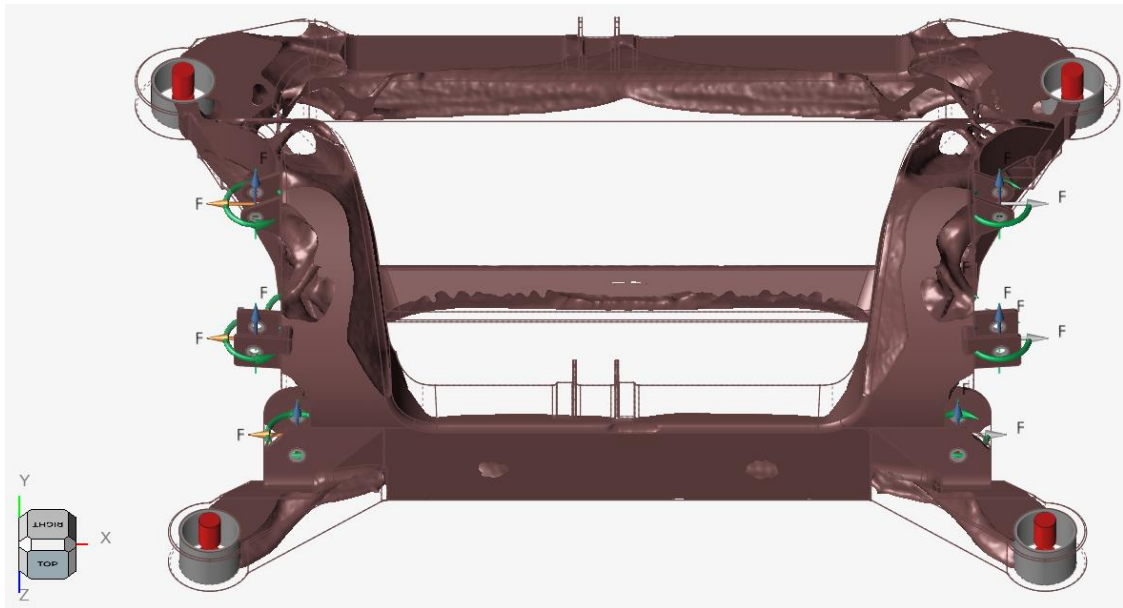


Figure 57. Rear Subframe Topology Optimization with Ti6Al4V (Front View)



Figure 58. Rear Subframe Topology Optimization with Ti6Al4V (Top View)

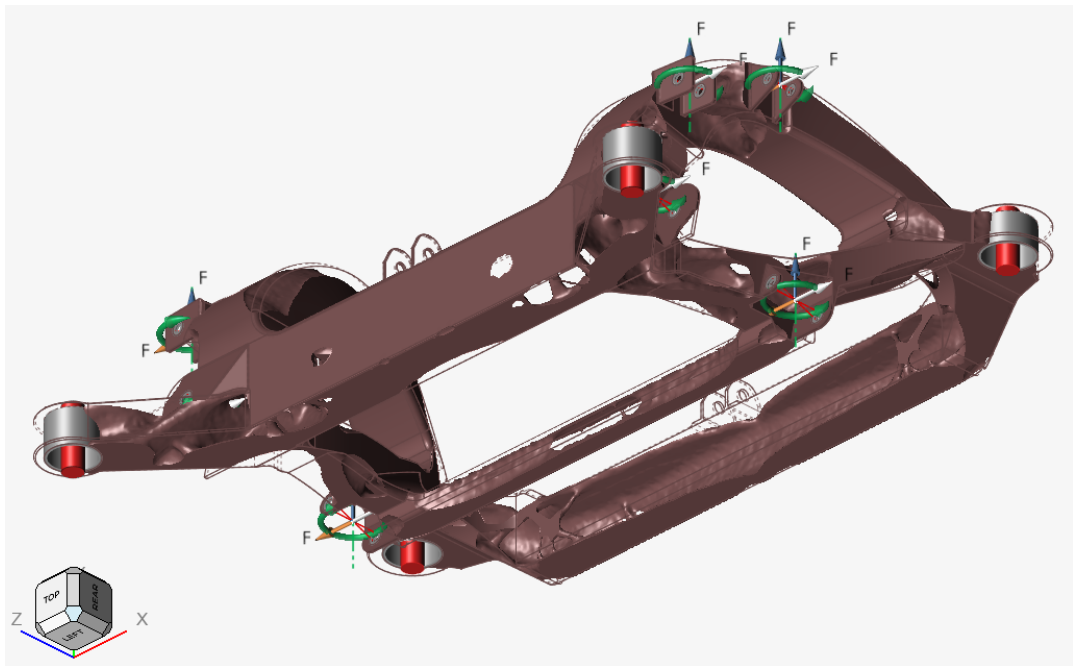


Figure 59. Rear Subframe Topology Optimization with Ti6Al4V (Bottom View)

Also in this case, once the final topology optimization results with Ti6Al4V are obtained, it is possible to fit the design space with the PolyNURBS curve by selecting the *Fit* command in the *PolyNURBS* ribbon on the Altair® toolbar.

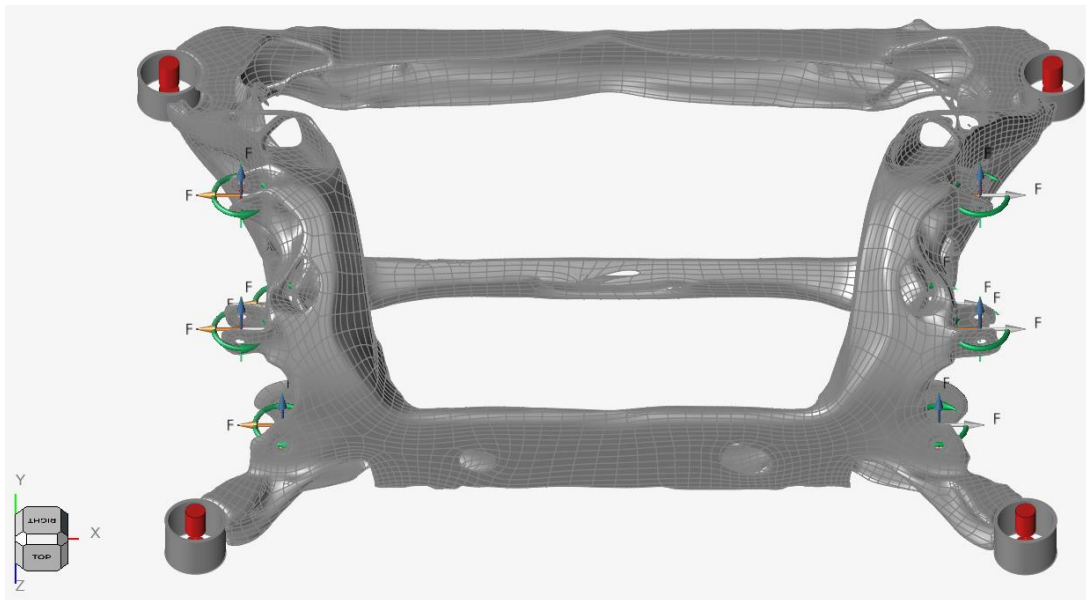


Figure 60. PolyNURBS Curve with Ti6Al4V (Front View)

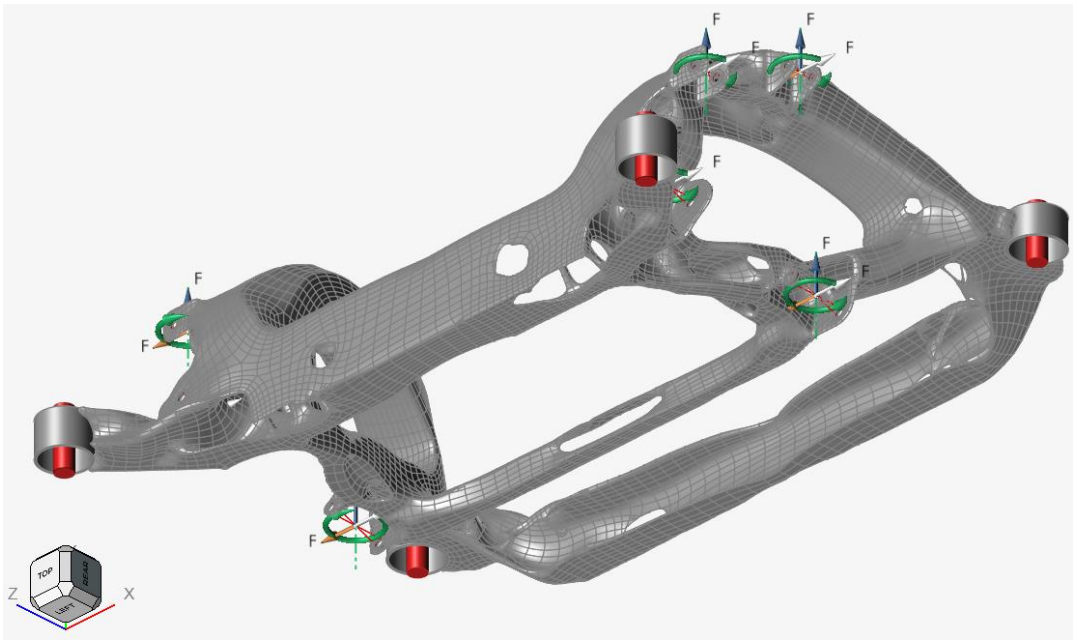


Figure 61. PolyNURBS Curve with Ti6Al4V (Bottom View)

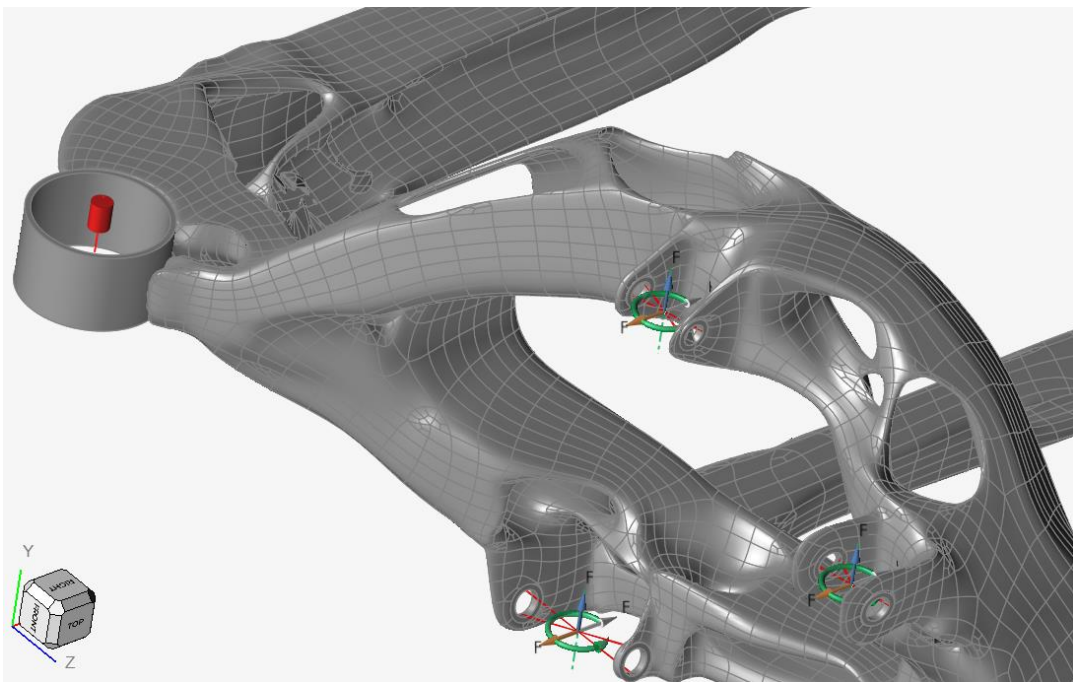


Figure 62. Detail of the Optimized Part with Ti6Al4V (Top Side)

7. FEM Analysis & Results

As the topology optimization of the Tesla® Model 3 rear subframe is completed and the component is fitted with the PolyNURBS curve, it is possible to move to the FEM analysis of the part in order to evaluate the mechanical stresses and displacements resulting from the applied load cases.

Before doing that however, it is necessary to evaluate the correct disposition of the mesh elements in the PolyNURBS curve, which can be easily evaluated by selecting the *Repair* command in Altair® in order to highlight the presence of voids or other anomalies in the mesh that could cause the surface to remain open and, therefore, to make the system consider the optimized component as if it had null volume.

Once all the different parameters and mesh characteristics for the optimized rear subframe have been set, it is possible to proceed to the FEM analysis taking into account the presence of all the main load cases simultaneously. From the performed evaluation, it is possible to consider the actual component's mechanical state. In particular, the analysed results will be focusing on the Von Mises stress distributions, on the displacements in each portion of the final part and on the safety Factor evaluation.

The results for the original component are shown in the figures below.

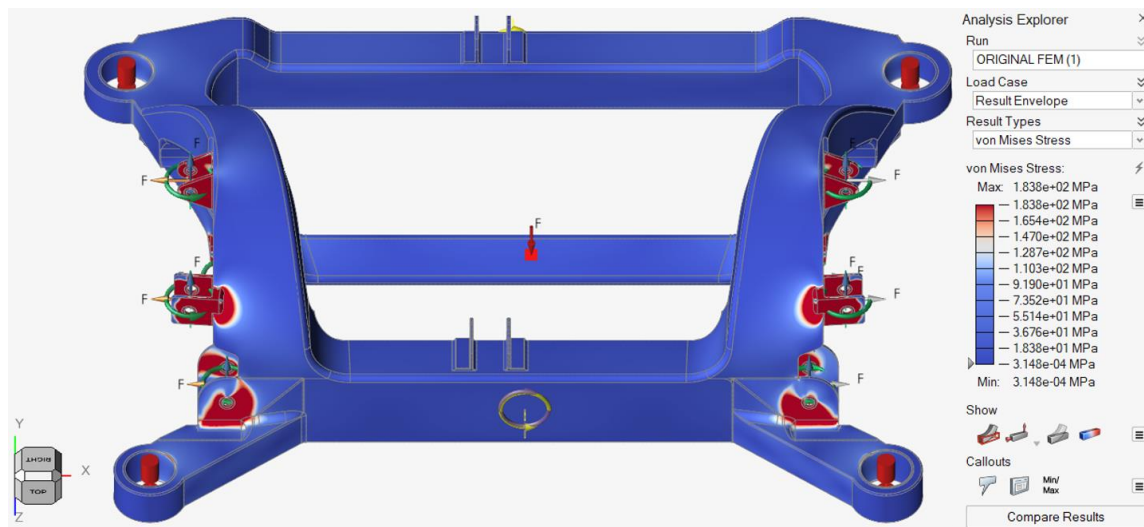


Figure 63. Von Mises Stress for the Result Envelope (Original Component)

From Figure 63 it is possible to see that the peak stresses are related to the brackets connecting the multi-link rods to the wheel hub. In particular, the areas characterized by highest stress values are the ones marked in red and they are subjected to loads that are in the range of 184 MPa, below the AISI 1025 yield strength (370 MPa). This means that the original component is verified for the considered load cases and it will be characterized by a safety factor (SF) that will be:

$$SF = \frac{\sigma_{RP,02}}{\sigma_{VM}} = \frac{370 \text{ MPa}}{184 \text{ MPa}} \cong 2.01$$

All the other areas characterized by a blue colour are subjected to much lower loads due to the presence of mechanical redundancies given by excessive amounts of material. In order to evaluate which are the effects of the other forces applied to the rear subframe and where they are acting, it is possible to decrease the top scale stress value so that it will be possible to better understand the mechanical state within the component. In particular, setting the top scale at 50 MPa, it is possible to analyse the following condition:

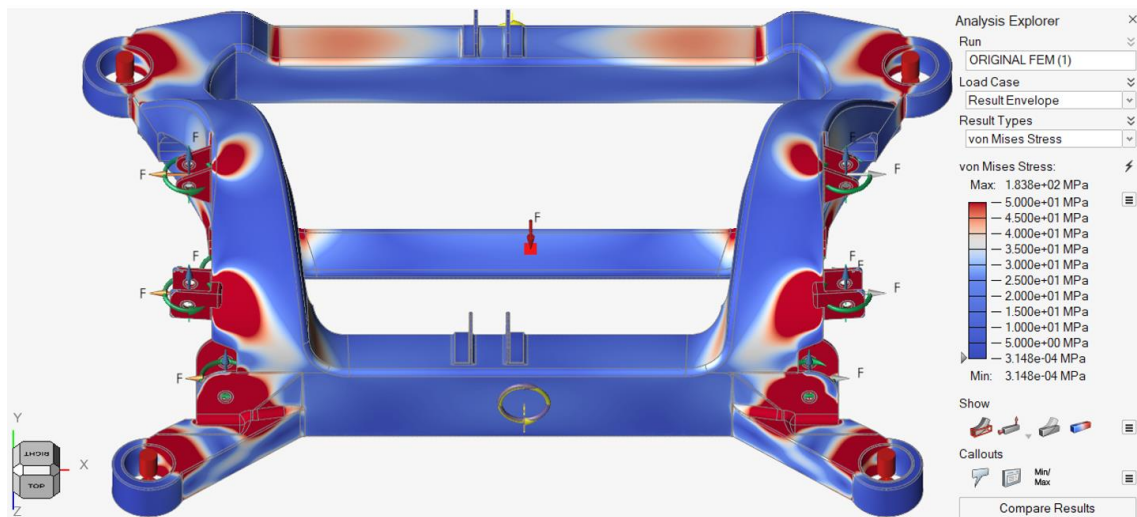


Figure 64. Original Result Envelope Von Mises Stress (Top Scale 50 MPa)

Following this evaluation, it is possible to see that the highest stresses are still located around the connection brackets, but they are also present in the areas where the horizontal beams are connected to the vertical arms of the rear subframe. It is also evident how that specific regions will be the main target for the topology optimization process, since they are subjected to the lowest stresses and, therefore, they can be characterized by the presence of a low amount of applied material. The areas underlined in this case will be characterized by a SF > 6.

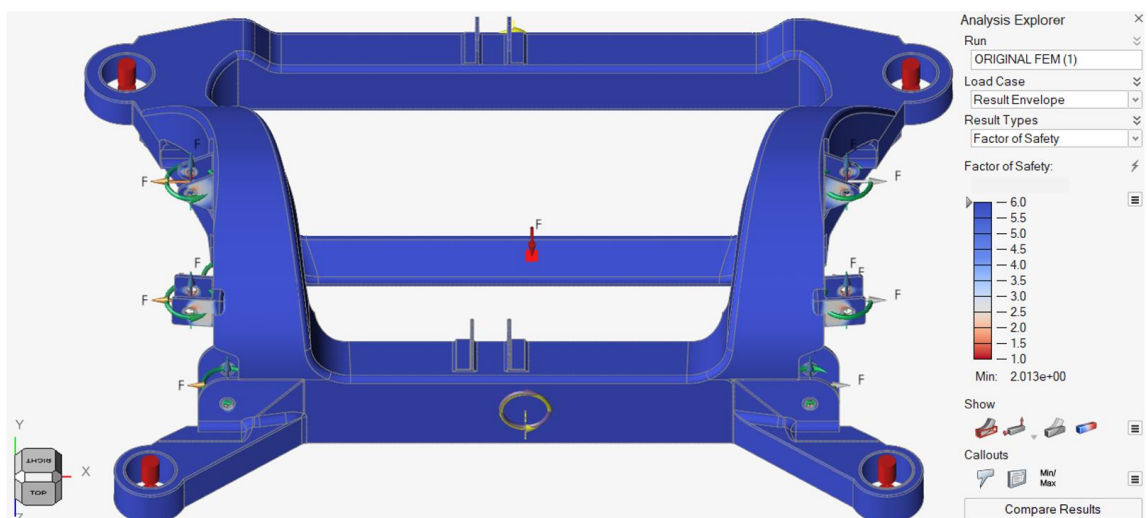


Figure 65. Safety Factor Distribution (Original Component)

Considering the displacements present in the original component, it is evident how the highest values will be present in the connection brackets. This is due to the presence of the highest stresses established in those regions, which will cause the portions of material to be characterized by the highest deformations. The displacements' field is represented in the figure below.

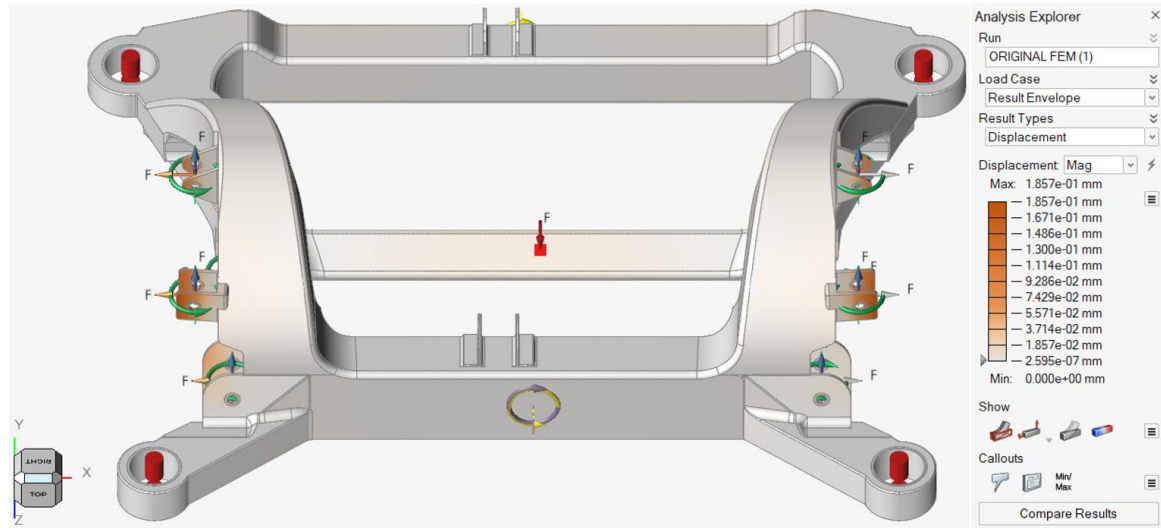


Figure 66. Displacements Distribution for the Result Envelope (Original Component)

From Figure 66 it is evident that what stated before is valid, in particular the maximum displacements present in the bracket areas are in the range of $1.857 \cdot 10^{-1}$ mm mostly along the direction of motion (x-axis), due to the fact that the highest excitations for the brackets are coming during accelerations and decelerations. It is possible to better understand the brackets behaviour by providing a graphical representation of the actual displacements with a magnified scale.

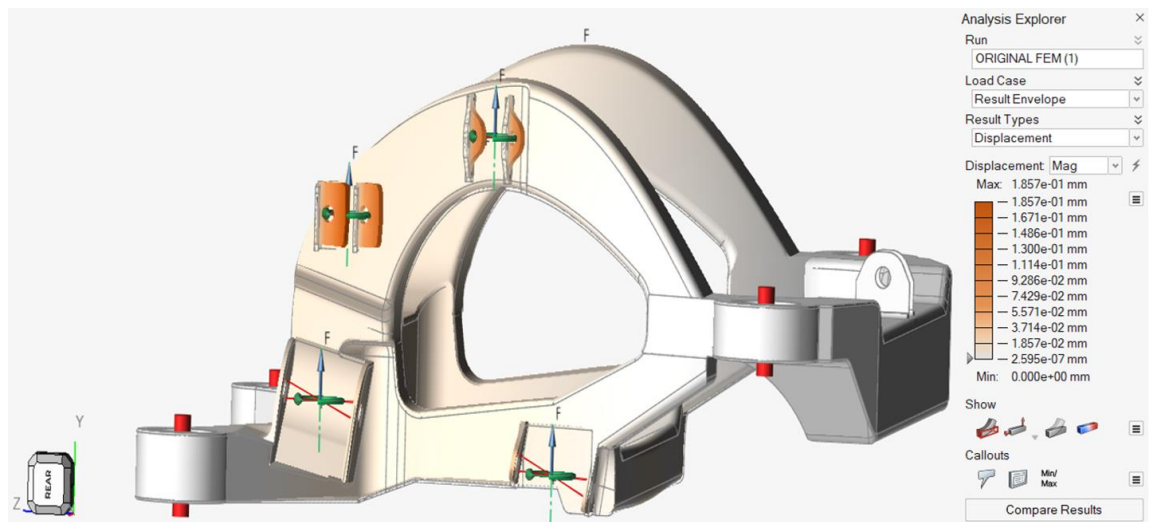


Figure 67. Displacement Direction in the Original Component (Magnified Scale)

The other forces and torques applied during the main driving operations considered so far contribute to a minor impact on the remaining central portions of the rear subframe. Also in this case it is possible to modify the top scale value in order to investigate their magnitude.

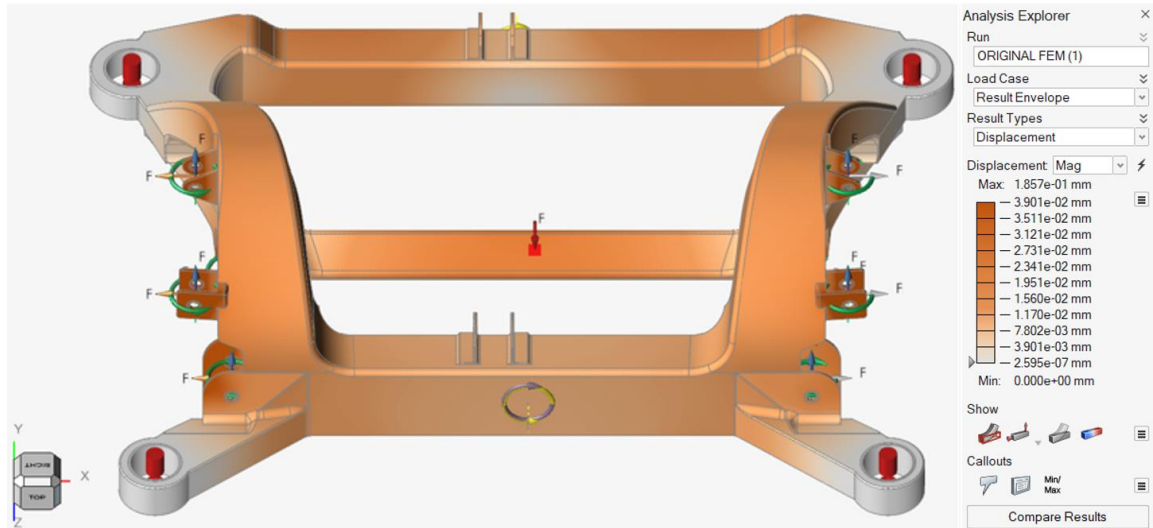


Figure 68. Original Result Envelope Displacements (Top Scale $3.901 \cdot 10^{-2}$ mm)

From the figure above, the top scale is adjusted to a value of $3.901 \cdot 10^{-2}$ mm which represents the maximum displacement for the regions in the middle of the bracket during sharp cornering conditions. The displacements in those areas are reasonably lower with respect to the ones experienced in the brackets mostly because, as already seen, the actual amount of Von Mises stresses and solicitations are much lower (about 1/7 of the maximum stresses). The only areas characterized by null displacements are the ones constrained at the beginning and corresponding to the attachment points of the rear subframe with the vehicle underfloor.

To sum up, the final results for the Von Mises stresses and for the displacements in the original component are listed in the table below.

Table 10. FEM Analysis Results (Original Component)

	Maximum Displacement	Maximum Stress
Acceleration/Deceleration	$1.857 \cdot 10^{-1}$ mm	184 MPa
Sharp Cornering (Right)	$3.901 \cdot 10^{-2}$ mm	28 MPa
Sharp Cornering (Left)	$3.901 \cdot 10^{-2}$ mm	28 MPa
Result Envelope	$1.857 \cdot 10^{-1}$ mm	184 MPa
Safety Factor	2.01	

Taking into account the final stresses and displacements obtained in the result envelope for the original component, it is also possible to try to predict an approximation for its fatigue life evaluation. In particular, since it is not possible to perform simulations related to fatigue evaluations in Altair® Inspire and, in general, these specific considerations are arising from experimental measurements, the followed approach is just an analytical one that provides approximate values for the fatigue life prediction, taking into account specific parameters, such as:

$$\sigma_{max} = 184 \text{ MPa (maximum tension)}$$

$$\sigma_{min} = 0 \text{ MPa (minimum tension)}$$

$$\sigma_m = \frac{\sigma_{max} + \sigma_{min}}{2} = 92 \text{ MPa (mean tension)}$$

$$\sigma_a = \frac{\sigma_{max} - \sigma_{min}}{2} = 92 \text{ MPa (alternate tension)}$$

$$\Delta\sigma_a = \sigma_{max} - \sigma_{min} = 2 \cdot \sigma_a = 184 \text{ MPa (tension field)}$$

$$R = \frac{\sigma_{min}}{\sigma_{max}} = 0 \text{ (tension ratio)}$$

Since $\sigma_{min} = 0$ and $R = 0$, it means that the considered cycles are repeated traction cycles. For stainless steels, the limit fatigue tension σ_D for a number of cycles $N = 10^6$, is given as follows:

$$\begin{cases} \sigma_D \approx 0.5 \cdot \sigma_R & \text{for } \sigma_R < 1400 \text{ MPa} \\ \sigma_D \approx 700 \text{ MPa} & \text{for } \sigma_R > 1400 \text{ MPa} \end{cases}$$

So, since the AISI 1025 steel has an ultimate tensile strength of 440 MPa, the final value for σ_D will be of 220 MPa. In order to design a component that is able to sustain a number of cycles ranging between $10^6 \div 10^8$, so that it can be considered as a Safe Life component (also referred as an infinite life component), it is possible to consider the fatigue safety factor S , that is:

$$S = \frac{\sigma_D}{\sigma_a} = \frac{220 \text{ MPa}}{92 \text{ MPa}} \cong 2.39$$

Since $S > 1$, it means that the original component is verified for an infinite life application, meaning that it can be considered as a Safe Life element.

Considering now the optimized component with SS 316L, it is possible to analyse the outcome of the FEM analysis and compare it to the one of the original one in order to better understand if the new design is feasible and if it provides an actual improvement of the performances of the part. In particular, the analysis will be focused on the Von Mises stresses, on the displacements and on the Safety Factor evaluation.



Figure 69. Von Mises Stress Distribution with SS 316L (Optimized Component)

From Figure 69 it is possible to see that, also in this case, the peak stresses are related to the brackets connecting the multi-link rods to the wheel hub. However, according to the optimization carried out so far, it is possible to see that due to the lower amount of material in the horizontal beams, there will be other mechanical stresses distributed in those regions.

From the FEM results however, it is possible to see that the stresses recorded inside the optimized component are above the material yield strength (205 MPa) and below the material yield strength after the L-PBF process (575 MPa). In particular, the areas characterized by the highest stress values are the ones marked in red in the legend and accounting for stresses around 467 MPa that are providing a component that will be verified ($SF > 1$).

It can be highlighted that the highest stresses are registered in the areas characterized by complex geometries that may be unsuccessfully approximated by the mesh elements, leaving sharp angles or too big elements unable to correctly cover the component's surface. It is then possible to create a more detailed mesh with more refined elements, that can further decrease the stress values.

It is then possible to proceed to the component validation, considering the real stresses as the ones directly measured by the software after completing the FEM analysis, meaning that the $SF > 1$ condition is respected. In particular, the safety factor will be:

$$SF = \frac{\sigma_{RP,02}}{\sigma_{VM}} = \frac{575 \text{ MPa}}{467 \text{ MPa}} \cong 1.23$$

It is possible to change the top scale value in order to evaluate which are the effects of the other forces applied to the rear subframe and where they are acting, providing a better representation and understanding of the mechanical state within the component. To perform a better comparison with the original component, also in this case the top scale has been set at 50 MPa.



Figure 70. Von Mises Stress Distribution with SS 316L (Top Scale 50 MPa)

From the previous figure, it is evident how the stress state is similar to the one present in the original component, with the majority of the stresses still located around the connecting brackets, but also distributed in correspondence of the middle areas of the horizontal beams. It is also important to notice that, differently from what happened before, the stresses in correspondence of the connection areas between vertical and horizontal beams are characterized by much lower stresses. Also in this case, the blue areas are characterized by $SF > 6$.



Figure 71. Safety Factor Distribution with SS 316L (Optimized Component)

Considering now the displacements in the optimized component, it is reasonable to assume that also in this case the highest values will be present in correspondence of the connecting brackets. This is partially true, since there are also other noticeable displacements present in the horizontal beams, especially in the middle areas, that are resulting from a decreased amount of material and a thinner component's section. The displacements' field is the following one:

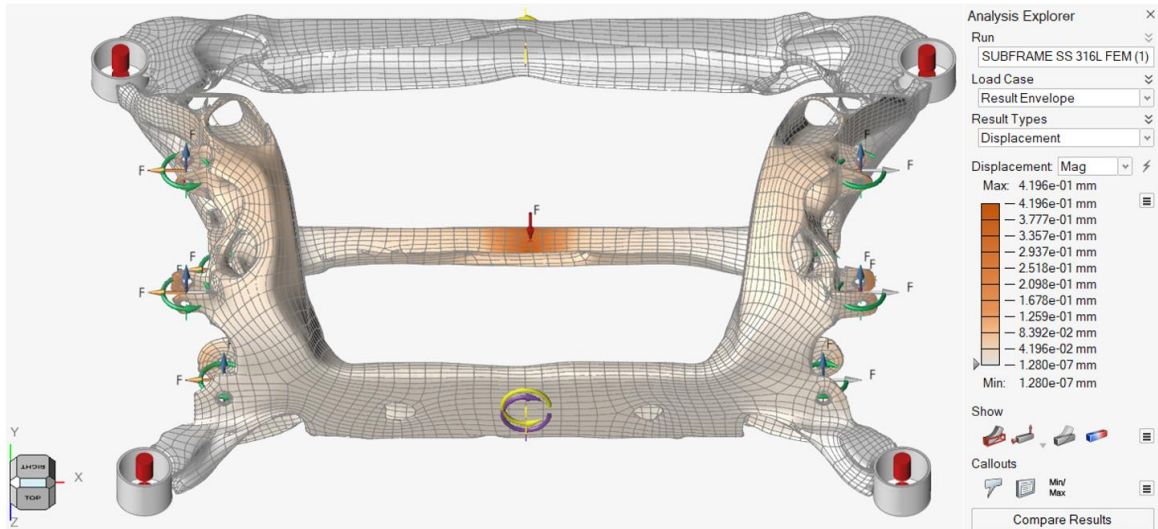


Figure 72. Displacement Distribution with SS 316L (Optimized Component)

From Figure 72 it is evident that what stated before is still valid, but what is interesting in this case is that the displacements present in correspondence of the connection brackets are similar to the ones in the middle of the beam. In particular, the values experienced in the connection brackets are in the range of $3.883 \cdot 10^{-1}$ mm and they are roughly coinciding with the ones present in the horizontal central beam ($4.196 \cdot 10^{-1}$ mm). Comparing the results obtained with the original component, the displacement values in the connection brackets experiences a 52% increase (from $1.857 \cdot 10^{-1}$ mm to $3.883 \cdot 10^{-1}$ mm).

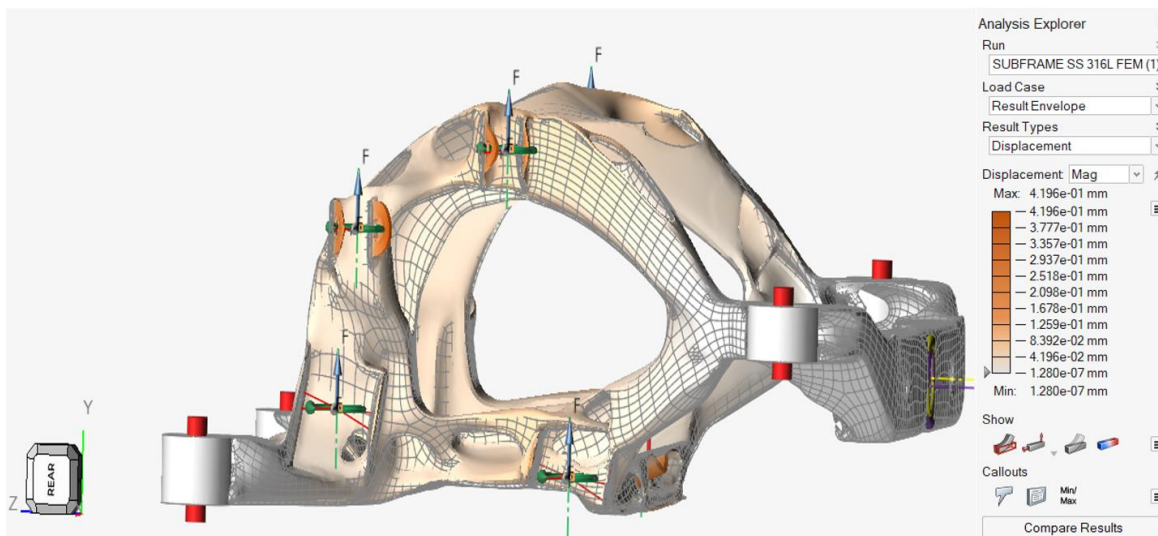


Figure 73. Displacement Direction with SS 316L (Magnified Scale)

From the graphical representation in a magnified scale, it can be noted that the highest displacements are mainly caused by emergency braking operations and by the weight force of the electric motor. This means that their directions will be along the x-axis and along the y-axis, respectively. The other forces and torques applied during the main driving operations considered so far contribute to a minor impact on the remaining central portions of the rear subframe. Also in this case it is possible to modify the top scale value in order to investigate their magnitude.

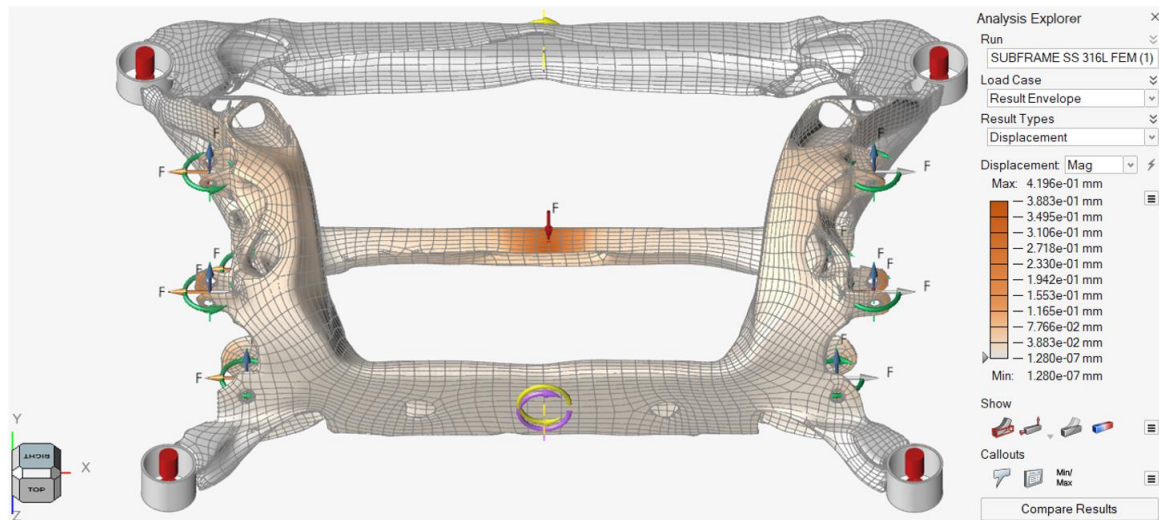


Figure 74. Displacement Distribution with SS 316L (Top Scale $3.883 \cdot 10^{-1}$ mm)

In this case, the top scale is adjusted to a value of $3.883 \cdot 10^{-1}$ mm which represents the maximum displacement for the regions in correspondence of the connection brackets during acceleration and deceleration conditions. The displacements in those areas are comparable to the ones experienced during sharp cornering phases since the actual amount of Von Mises stresses and solicitations present in the rear subframe in this condition is similar to the previous one. The only areas characterized by null displacements are the ones constrained at the beginning and corresponding to the attachment points of the rear subframe with the vehicle underfloor.

To sum up, the final results for the Von Mises stresses and for the displacements in the optimized component with SS 316L are listed in the table below.

Table 11. FEM Analysis Results with SS 316L (Optimized Component)

	Maximum Displacement	Maximum Stress
Acceleration/Deceleration	$3.883 \cdot 10^{-1}$ mm	467 MPa
Sharp Cornering (Right)	$4.196 \cdot 10^{-1}$ mm	187 MPa
Sharp Cornering (Left)	$4.196 \cdot 10^{-1}$ mm	187 MPa
Result Envelope	$4.196 \cdot 10^{-1}$ mm	467 MPa
Safety Factor	1.23	

Considering now the optimized component with Ti6Al4V, it is possible to perform the same FEM analysis as before, examining its results and comparing them to the original ones in order to better understand if the new design can be validated and if it provides an actual improvement of the performances of the part. Also in this case, the analysis will be focused on the Von Mises stresses, on the displacements and on the Safety Factor evaluation.



Figure 75. Von Mises Stress Distribution with Ti6Al4V (Optimized Component)

From Figure 75 it is possible to see that what stated before is still valid, with the peak stresses related to the brackets connecting the multi-link rods to the wheel hub. On the other hand, according to the optimization carried out so far, it is possible to see that differently from before, the stresses on the middle horizontal beam where the electric motor assembly is located are sensibly lower with respect to the SS 316L case.

The areas characterized by highest stress values are also in this case the ones marked in red and they are subjected to loads that are in the range of 502 MPa, that are higher of about 63% with respect to the ones acting on the original component, but that are far below the Ti6Al4V yield strength (827 MPa). This is due to the fact that thanks to the higher mechanical strength of the Ti alloy, it has been possible to noticeably decrease the amount of used material and the overall component thickness. Since the yield strength experienced during the application of the different load cases is lower than the limit one, this optimized component is still verified for the considered load cases and it will be characterized by a safety factor (SF) that will be:

$$SF = \frac{\sigma_{RP,02}}{\sigma_{VM}} = \frac{827 \text{ MPa}}{502 \text{ MPa}} \cong 1.65$$

As previously done, it is possible to change the top scale value in order to evaluate which are the effects of the other forces applied to the rear subframe and where they are acting, providing a better representation and understanding of the mechanical state within the component. To perform a better comparison with the original and the optimized components with SS 316L, also in this case the top scale has been set at 50 MPa.



Figure 76. Von Mises Stress Distribution with Ti6Al4V (Top Scale 50 MPa)

From the previous figure, it is evident how the stress state is similar to the all the other ones already analysed, with the majority of the stresses still located around the connecting brackets. The only difference, pointed out in the previous paragraph, is given by the lower amount of stresses present in the central horizontal beam. It is also important to notice that, similarly to what happened before, the stresses in correspondence of the connection areas between vertical and horizontal beams are characterized by much lower stresses with respect to the ones experienced in the original component. Also in this case, the blue areas are characterized by $SF > 6$.

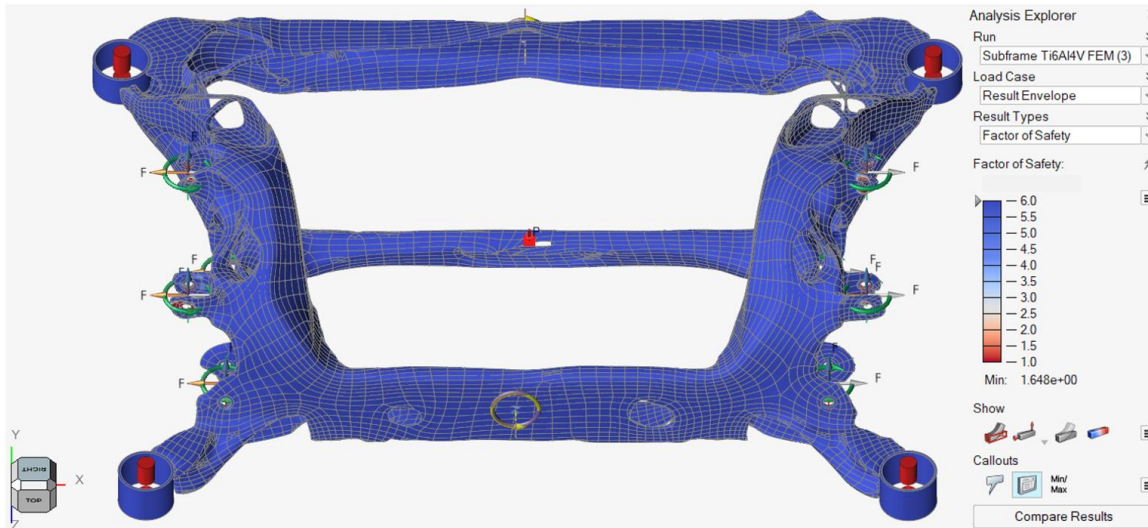


Figure 77. Safety Factor Distribution with Ti6Al4V (Optimized Component)

Considering now the displacements in the Ti6Al4V component, it is reasonable to assume that also in this case the highest values will be present in correspondence of the connecting brackets. The displacements' field is the following one:

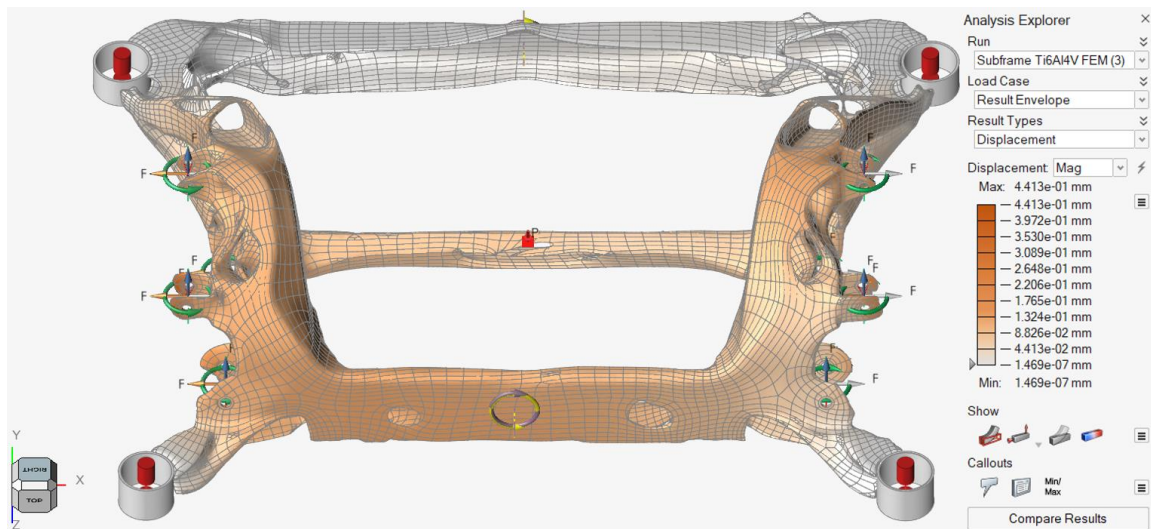


Figure 78. Displacement Distribution with Ti6Al4V (Optimized Component)

Similarly to the SS 316L case, the optimized component with Ti6Al4V shows similar values both in the connecting brackets and in the horizontal beams, with a more uniform displacement distribution. In particular, the peak values experienced in this condition are comparable to the ones present in the optimized component with SS 316L, with a maximum value of $4.413 \cdot 10^{-1}$ mm in acceleration and deceleration conditions and of $1.810 \cdot 10^{-1}$ mm in sharp cornering conditions.

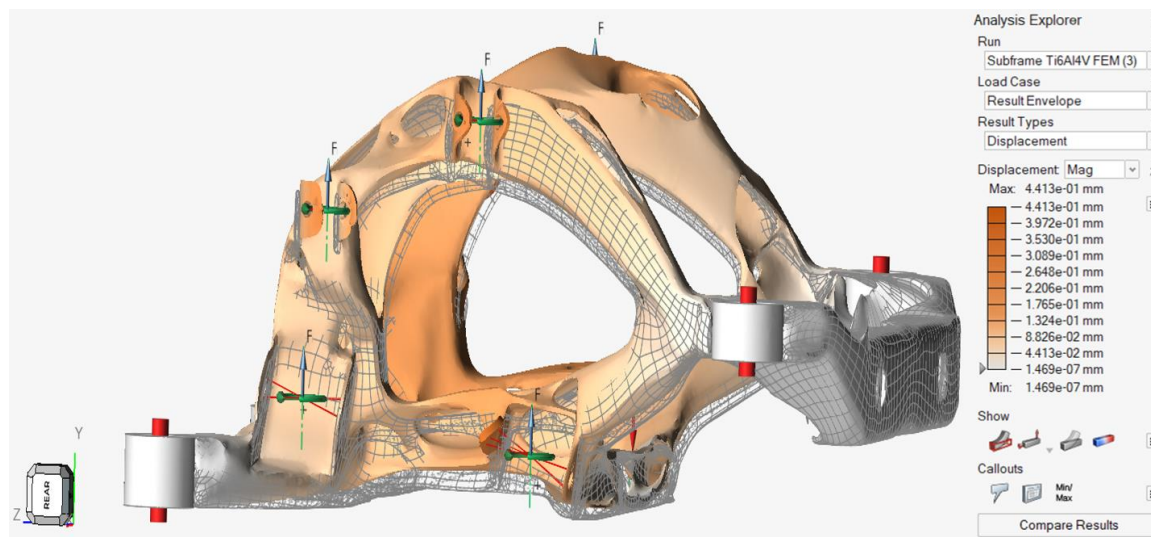


Figure 79. Displacement Direction with Ti6Al4V (Magnified Scale)

From the graphical representation in a magnified scale, it can be noted that the highest displacements are mainly caused by acceleration, emergency braking and sharp cornering conditions. This means that their directions will be along and around the x-axis, respectively. The only areas characterized by null displacements are the ones constrained at the beginning and corresponding to the attachment points of the rear subframe with the vehicle underfloor.

Also in this case it is possible to modify the top scale value to $1.810 \cdot 10^{-1}$ mm in order to investigate their magnitude during cornering operations, that are roughly the same values of the ones experienced during accelerations/decelerations in the original component.

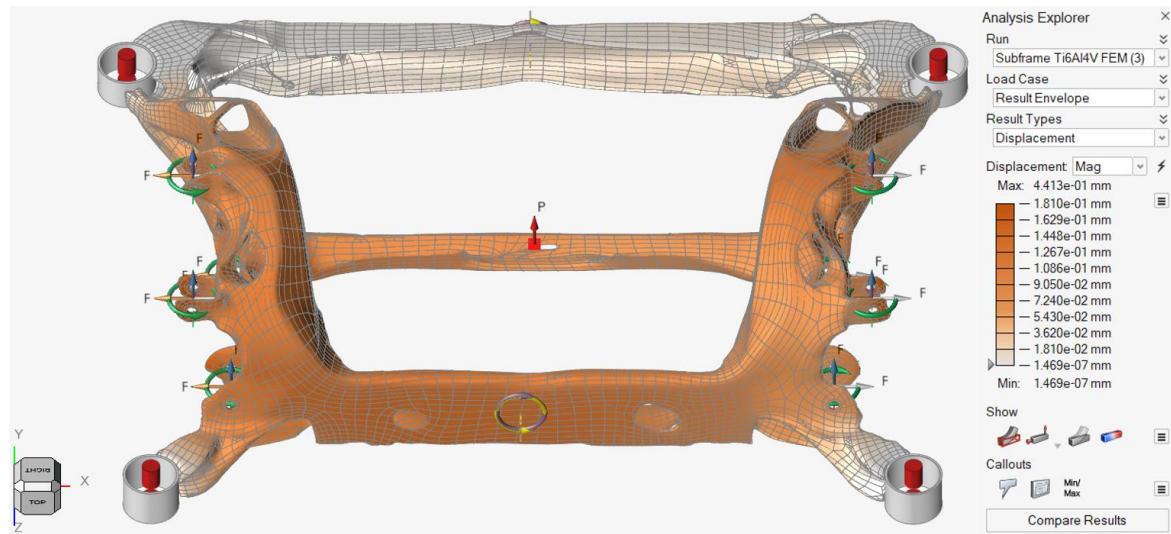


Figure 80. Displacement Distribution with Ti6Al4V (Top Scale $1.810 \cdot 10^{-1}$ mm)

To sum up, the final results for the Von Mises stresses and for the displacements in the optimized component with Ti6Al4V are listed in the table below.

Table 12. FEM Analysis Results with Ti6Al4V (Optimized Component)

	Maximum Displacement	Maximum Stress
Acceleration/Deceleration	$4.413 \cdot 10^{-1}$ mm	502 MPa
Sharp Cornering (Right)	$1.810 \cdot 10^{-1}$ mm	323 MPa
Sharp Cornering (Left)	$1.810 \cdot 10^{-1}$ mm	323 MPa
Result Envelope	$4.413 \cdot 10^{-1}$ mm	502 MPa
Safety Factor	1.65	

Taking into account the results obtained for the FEM analyses for the optimized components with SS 316L and Ti6Al4V, it is possible to underline that the final optimized subframes are verified in both the conditions ($SF > 1$). However, the obtained values can be further improved especially by managing the component geometry and mesh quality, for example providing smoother surfaces or increasing the number of mesh elements (to obtain a better surface approximation).

The chosen material to proceed with the L-PBF process is the SS 316L one since, other than being already prescribed for the chosen AM machine, it provides valid and acceptable results with better performances and lower weight with respect to the original component in AISI 1025.

Ti alloys can also be considered, especially because of their high mechanical strength and high weight reduction potential, even if the main drawback in this case is given by the high powder costs. However, considering the Tesla® Model 3 Dual Motor, since it belongs to a high segment, it has to be pointed out that the price for using Ti alloys instead of stainless steels is of lower impact in the final purchasing price.

In both the optimized cases, it is possible to perform the same fatigue life evaluations performed for the original component. In particular, it is possible to consider the SS 316L case since it will be the material that will be chosen for the L-PBF process, with final mechanical performances that will be affected by the applied AM technology, that can be considered as preliminary heat treatment.

Considering the final stresses and displacements obtained in the result envelope for the optimized component, it results that $\sigma_{\max} = 467$ MPa, $\sigma_{\min} = 0$ MPa, $\sigma_a = 234$ MPa and $R = 0$, meaning that the considered cycles are still repeated traction cycles. Taking into account the ultimate tensile strength for SS 316L processed with L-PBF, it is around 695 MPa, so also in this case it results that, for a number of cycles $N = 10^6$, $\sigma_D \approx 0.5 \cdot \sigma_R = 348$ MPa.

The final value for the SS 316L fatigue safety factor will be $S = 1.48$, meaning that also in this case the component can be considered as a Safe Life one ($S > 1$), ensuring the possibility to sustain a number of cycles between $10^6 \div 10^8$ (infinite life). Also in this case, the utilization of AM technologies provide an improvement of the final part performances, not only from a static point of view, but also from a fatigue life one, thanks to the presence of a verified part that is able to better distribute the applied loads with a lower material utilization, that is translated in noticeable weight savings.

8. AM Machine Choice & Building Process

Considering now the AM machine selection, particular attention should be kept on the optimized component dimensions. Specifically, due to the large dimensions of the final part, the choice is falling on a single machine, that is the Laser XLINE 2000R by General Electrics®. This device has been designed with the aim to manufacture large components with L-PBF technology and it is the only one that is able to properly host the rear subframe, even if it still has to be split into different smaller components that need to be welded together afterwards.

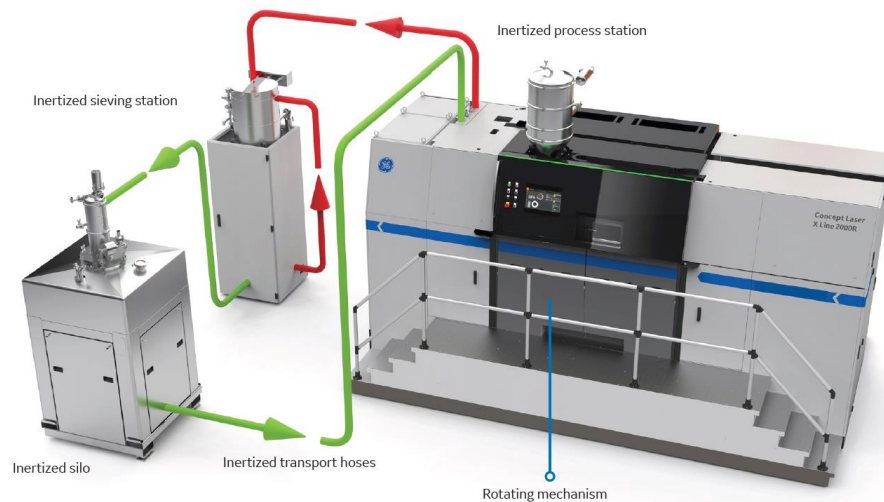


Figure 81. Laser XLINE 2000R Configuration (by General Electrics®)

From the manufacturer's brochure, it has been possible to better understand the main characteristics of this machine. In particular, the L-PBF process is performed inside an inert environment (N_2) to avoid melted material oxidation and the chamber provides an optimized upper and lower gas flow for better part quality and consistency. The main machine features are:

Table 13. Laser XLINE 2000R Features

Build Envelope	<i>800 x 400 x 500 mm (x, y, z)</i>
Layer Thickness	<i>30 ÷ 150 μm</i>
Production Speed	<i>up to 120 cm³/h</i>
Laser System	<i>2 fibre lasers (each 1000 W)</i>
Max Scanning Speed	<i>7 m/s</i>
Focus Diameter	<i>100 ÷ 150 μm</i>
Heating	<i>9 kW</i>
Inert Gas (N_2) Consumption	<i>17 ÷ 34 l/min</i>
Weight	<i>approx. 9500 kg</i>
Dimensions	<i>5235 x 3655 x 3604 mm (x, y, z)</i>

The powders that are used for XLINE 2000R applications are SS 316L, AlSi10Mg, Inconel® 718 and Ti6Al4V. In particular, considering what has been stated before during the topology optimization process and FEM analyses, SS 316L and Ti6Al4V, are the chosen ones mostly because they are able to provide high mechanical performances and resistances for the final application. Specifically, the one used for the building process simulation will be the SS 316L.

Once the machine and the materials have been chosen, it is possible to move towards the setting up of the building process. In particular, there can be different parts orientations to be considered that will provide different outcomes, both in terms of material usage, building time and final part strength. Moreover, since the considered process is L-PBF, it is also necessary to take into account the presence of supports used in order to sustain the component during the whole building process and that will have an impact on the used material, the total building time and the final cost, since they have to be removed following post processing operations.

First of all, it is necessary to set up the printing process directly in Altair® Inspire environment, splitting the lateral parts of the component from the horizontal central beams, selecting the component to be produced, the material and defining the building chamber characteristics. The component is then divided using the *Slice* command and the remaining sections are selected as parts to be printed.

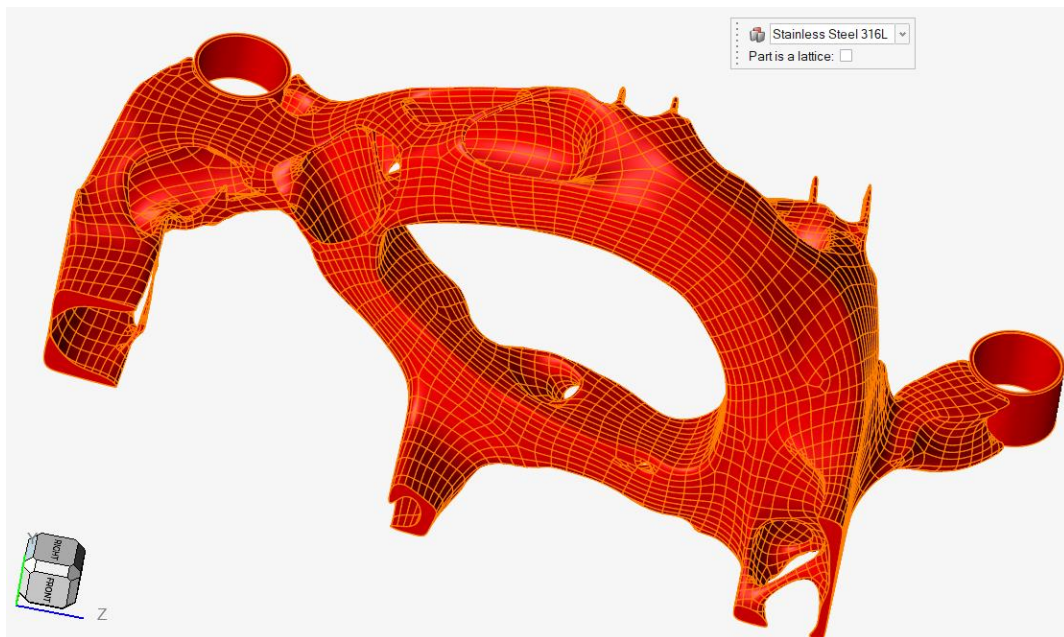


Figure 82. Lateral Subframe Section Selected for 3D Printing

Once this first step is done and the part and the material have been selected, it is possible to define the AM machine to be used for the process. In this particular case, since the previously selected machine is not present in the Altair® database, it is necessary to manage its dimensions so that the powder bed is able to host the component. To this extent, it is possible to select the *Printer* command in the Print3D toolbar and define a printer with dimensions 800 x 400 x 500 mm.

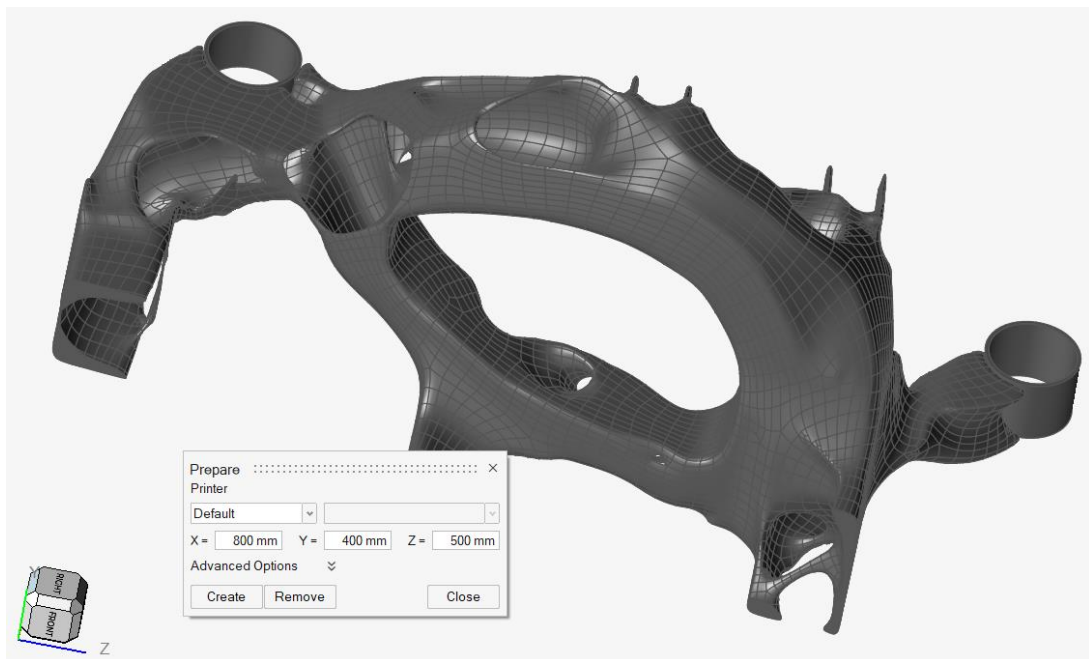


Figure 83. AM Machine Setting in Altair®

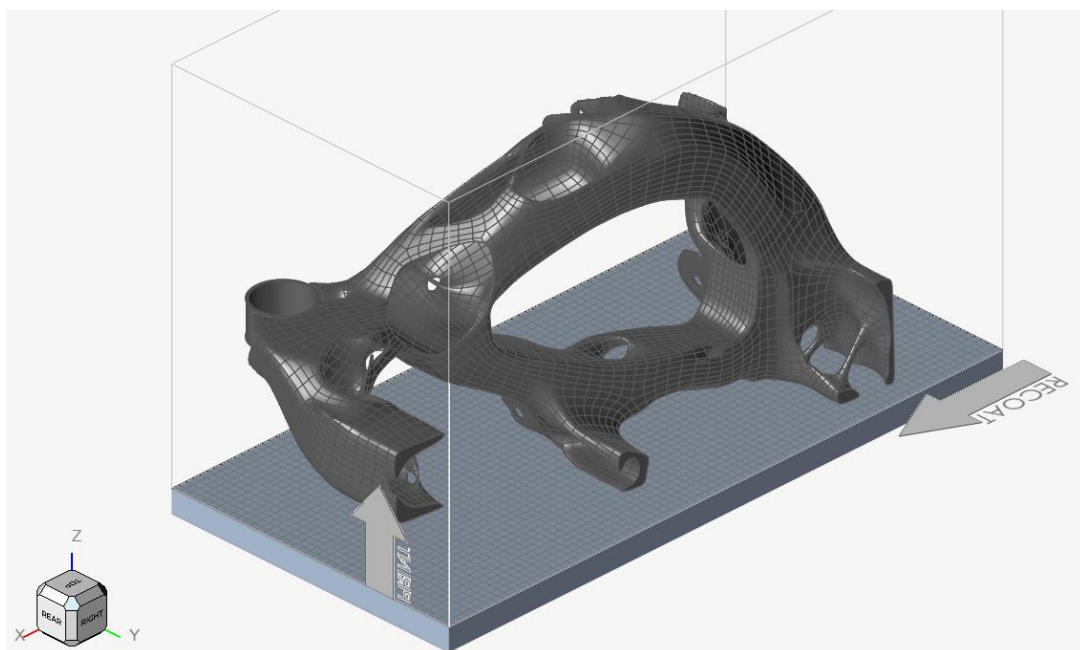


Figure 84. Part Positioning Inside the 3D Printer

It is now possible to proceed to the optimization of the part orientation inside the AM machine in order to provide an effective building process that is able to ensure a trade-off between number of supports and building time. In order to perform this operation, it is possible to consider the Optimize Orientation command and assign the highest weights to the time and support factors. The result of this operation provides an optimized configuration with $X = 90^\circ$ and $Y = 180^\circ$.

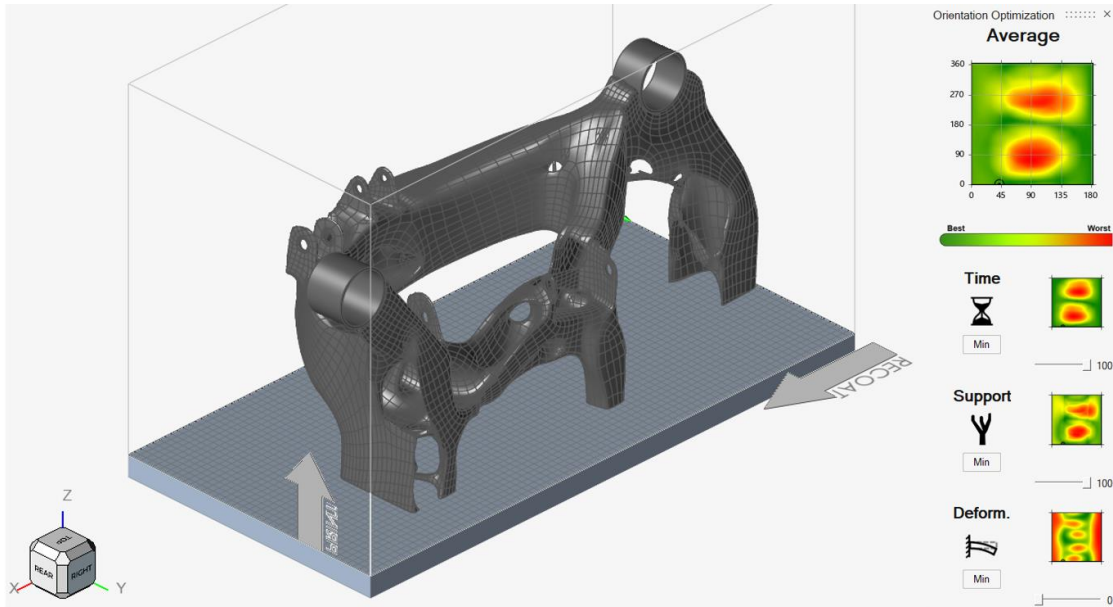


Figure 85. Component Orientation Optimization

Once the orientation of the component within the building envelope has been set, it is possible to define the presence of the supports and to take into account the possibility to use lighter structures, ensured by the presence of small holes throughout their whole surface (highlighted in yellow).

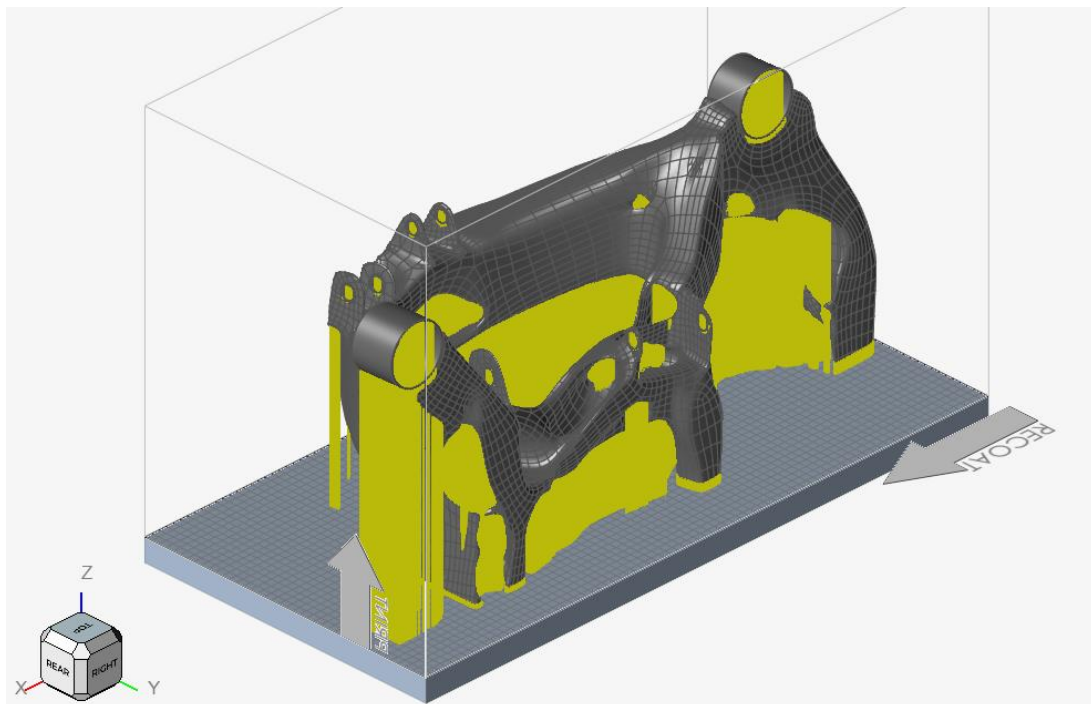


Figure 86. Light Support Structures for the Lateral Sections

Taking into account the orientation and the support structures defined in the previous figure, the result will provide a support volume of $5.135 \cdot 10^6 \text{ mm}^3$ and an overall printing time for the complete component of 64 hours and 9 minutes.

The final results for the FEM analysis carried out after the L-PBF process are represented in the following figures taking into account the Von Mises stresses and the displacement fields.

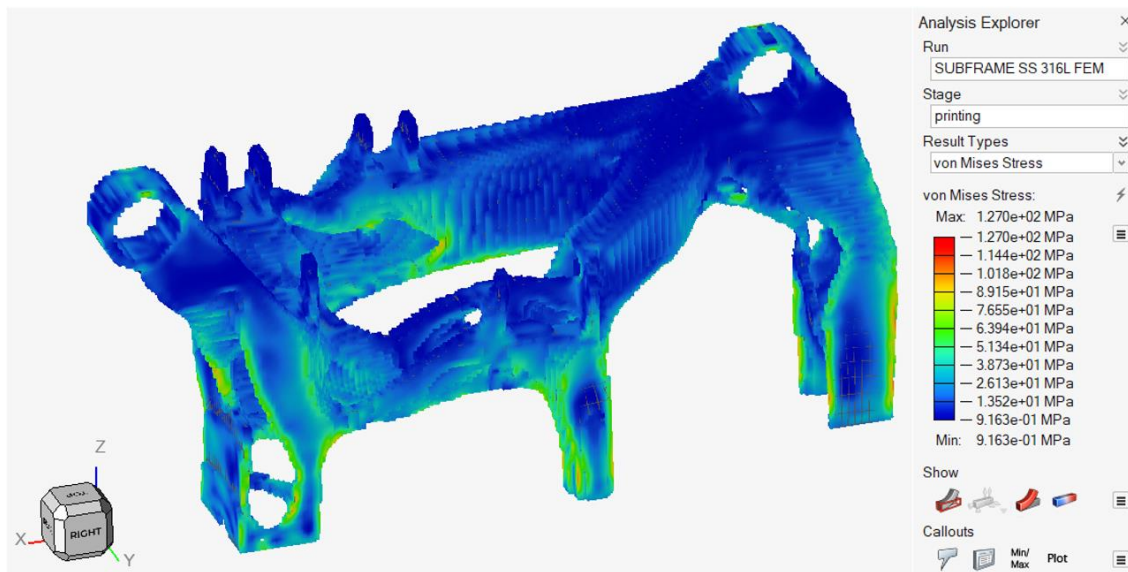


Figure 87. Von Mises Stresses in L-PBF (Lateral Section Right Side)

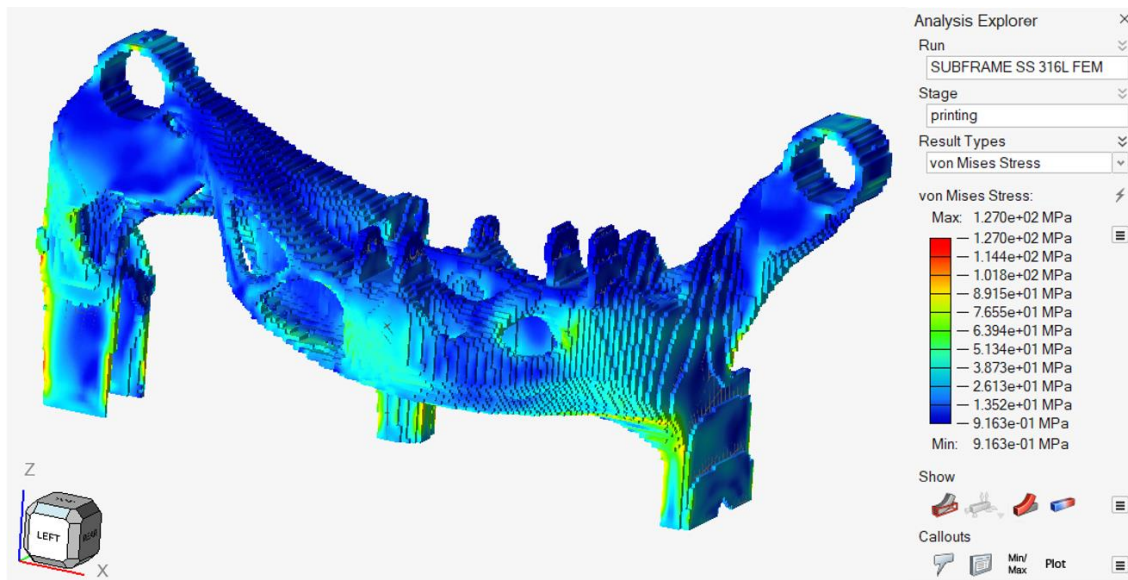


Figure 88. Von Mises Stresses in L-PBF (Lateral Section Left Side)

From figures above, it is possible to see how the component is made during the L-PBF following a layer-by-layer strategy with the presence of a step trend given by the actual layer thickness. The step trend, also called staircase effect, will be as marked as the layer thickness and mesh elements dimension increase. Moreover, it is possible to see that the Von Mises stresses reach peaks in the range of 127 MPa, that are still below the SS 316L yield strength when processed with L-PBF technology (575 MPa), meaning that the component is still verified for the considered process and it can be manufactured without failures.

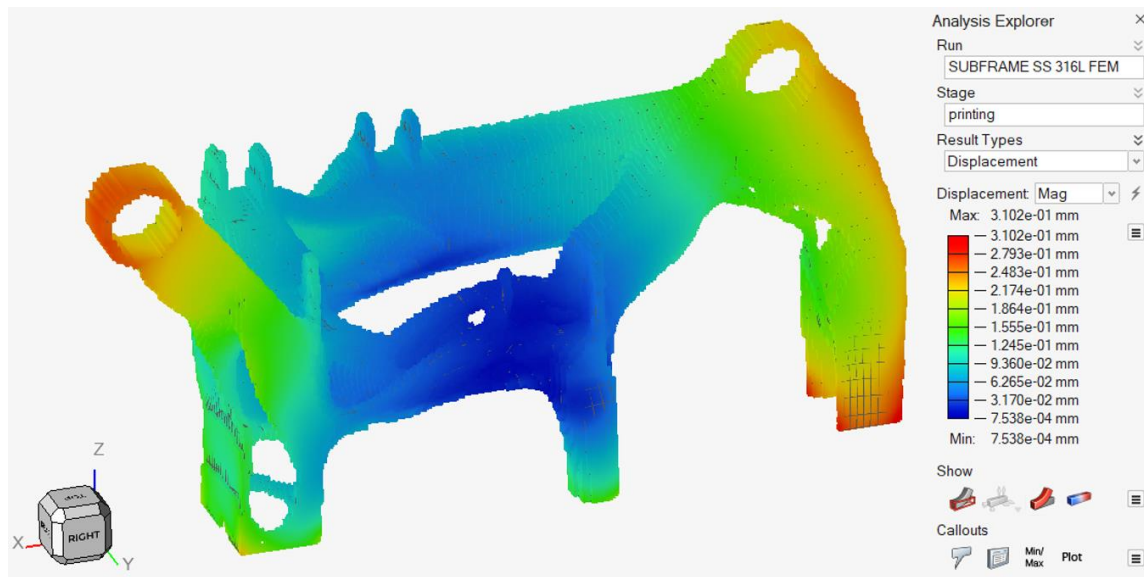


Figure 89. Displacements in L-PBF (Lateral Section Right Side)

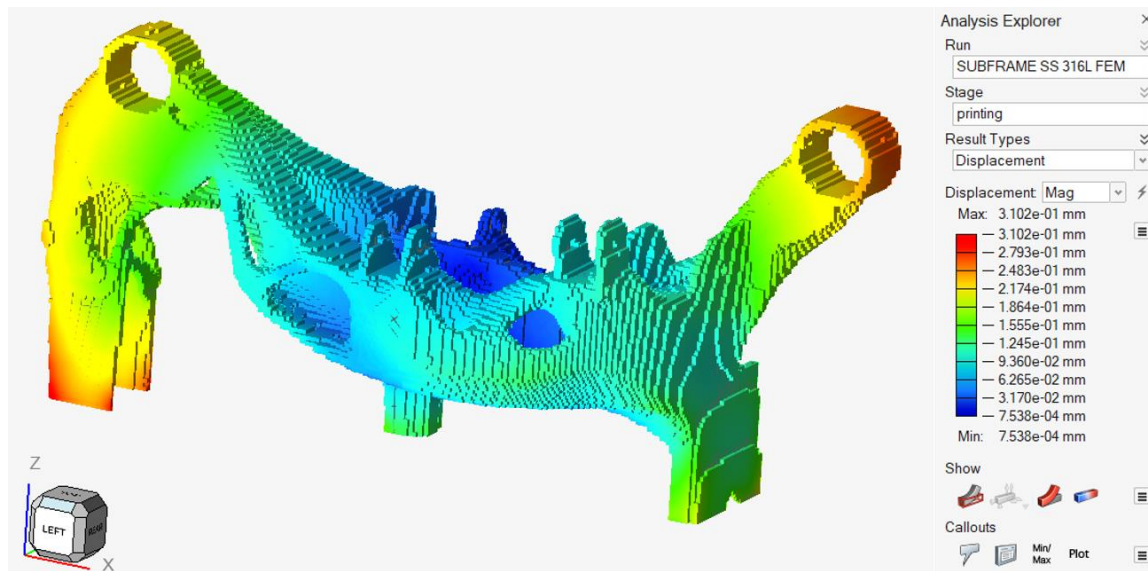


Figure 90. Displacements in L-PBF (Lateral Section Left Side)

Considering the displacements field, it is possible to see that they are characterized by peak values around $3.102 \cdot 10^{-1}$ mm in correspondence of the lateral extremities connecting the subframe to the vehicle underfloor, mostly raising from thermal gradients established between one layer and the other during the L-PBF process. This means that the final component will provide acceptable results both in terms of accuracy and integrity, since the actual deviations established during the printing process are so small that the component can still meet the established tolerances.

Part of these results can be also attributed to the supports that, other than sustaining the main component structure, also provide a thermal sink that is able to discharge part of the heat and the energy coming from the lasers melting the powder layers, making it possible to avoid too high stresses and displacements in the final component, even if they have to be removed with labour intensive processes (such as cutting) once the final part is ready.

When dealing with the AM process, the main cost is attributed to the manufacturing stage of the lateral sections, since the middle portions can be constituted by L-shaped, U-shaped and rectangular steel tubes, that are characterized by a negligible cost with respect to the final part one. However, it is fundamental to consider some specific technologies to join all the parts together, such as traditional mechanical or welding techniques, that require a specific part preparation, especially in the regions that will be joined together.

To this extent, it is possible to consider machining operations for the connection holes and for the areas directly involved in the joining of the different components. It is quite important that the connection holes and the whole part surface are characterized by the adequate geometrical tolerances, especially the connection areas that have to match with other external components. Moreover, other operations related to surface finishing have to be considered also for part preparation in order to perform the final parts' assembly and also to decrease the risk of notch effect caused by irregular surface areas.

The finishing operations of metal components produced with additive manufacturing can be distinguished in different categories, such as:

- Machining & Mechanical conversion → machining, shot peening, grinding
- Thermal processes → heat treatments, stress relieving
- Chemical & Electro-chemical processes → etching, electro-polishing

Other specific machining operations can be performed to mechanically link the different elements enabling the so-called hybrid manufacturing, which joins together the additive and the subtractive manufacturing processes. Generally, the additive process to consider in this case is DED (Direct Energy Deposition), that allows to repair or join together the different parts belonging to the same component, while the subtractive one is performed with 5-axis CNC machines that allow to obtain near net shapes with great accuracy, making it also possible to remove possible defects arising from the AM process.^[20]

When considering the welding process, it is necessary to properly set the whole process in order to consider the correct amount of heat to be applied to the part, according to the material thermal conductivity and specific heat coefficient, so that the cooling rate is adequate to provide solid-state transformations that are not negatively influencing the actual heat affected zones. It has to be pointed out, however, that whenever welding is considered, due to the high levels of localized heat that create extended melt pools, it is necessary to consider some specific operations, such as stress relieving or heat-treatments, in order to decrease the residual stresses induced by thermal gradients established during the process, to avoid distortions or deformations and to improve the mechanical performances of the joints.

All the portions that are of major interest in the welding process have to be properly prepared by means of grinding or surface finishing operations in order to avoid the presence of impurities or defects, such as porosities, that are undesirable and that can decrease the structural integrity of the component once the process is finished, causing the final component to fail under different conditions with respect to the ones previously analysed during the topology optimization process and FEM analyses.

9. Cost Evaluation

Considering a more detailed discussion on the material that have been selected to perform the rear subframe topology optimization, it is possible to perform a comparison between the SS 316L and the Ti6Al4V. The main chemical and mechanical characteristics for each material have been previously presented and, taking into account the volume of the final components and the actual market price for each powder taken from the www.3dpowderhub.com website, it is possible to evaluate the final component costs.

In particular, the SS 316L powder is providing good mechanical performances in terms of tensile and yield strength and it is characterized by quite higher weight than Ti alloys, with a density of 8 g/cm³. The cost for 10 kg of spherical particles powder is 430.99€ for a tap density of 5 g/cm³.

The Ti6Al4V powder is characterized by high performances in terms of tensile and yield strength and it is a very light-weight material with a density of 4.429 g/cm³. The cost for 10 kg of spherical particles powder is 2497.99€ for a very low tap density of 2.5 g/cm³.

The Ti alloy is the best one in terms of performances and weight reduction (-56% with respect to the component built with SS 316L) but the main drawback of this powder is related to the high costs. On the other hand, the SS 316L is the one with lower mechanical performances with respect to the Ti6Al4V but, as described in the validation of the optimized part, it is still acceptable to satisfy the load-torque requirements of the components.

Two part optimizations with the two different materials have been done in order to evaluate the amount of volume and weight for the optimized part:

- SS 316L Optimized Part Volume $\rightarrow 1.008 \cdot 10^6 \text{ mm}^3 \rightarrow 8.06 \text{ kg}$
- Ti6Al4V Optimized Part Volume $\rightarrow 4.397 \cdot 10^5 \text{ mm}^3 \rightarrow 3.48 \text{ kg}$

Some calculations can be made for the two materials in order to evaluate the total cost for the first powder order and for each produced rear subframe. First of all, it is necessary to calculate the building chamber volume occupied by the powder inside the AM machine and it can be considered as the product between the platform area and the height of the component inside the building chamber, and it corresponds to $1.184 \cdot 10^8 \text{ mm}^3$.

- SS 316L Powder Density $\rightarrow 5 \text{ g/cm}^3$
- Ti6Al4V Powder Density $\rightarrow 2.5 \text{ g/cm}^3$

$$\text{Powder(kg)} = \text{Powder Density} \cdot \text{Occupied Building Chamber Volume}$$

$$\text{First Order Cost(€)} = \text{Powder(kg)} \cdot \text{Powder Price(€/10kg)}$$

- SS 316L $\rightarrow 592 \text{ kg} \rightarrow 25'514.60 \text{ €}$
- Ti6Al4V $\rightarrow 296 \text{ kg} \rightarrow 73'940.50 \text{ €}$

As it is possible to see from the previous data, the volume of the part is way smaller than the chamber volume so a lot of unused powder is present after the AM process. Fortunately, almost all the unused powder can be re-used for the next process. The small amount of wasted powder accounts for approximately 1% of the unused one and, the cause of this loss, is due to the fact that the powder very close to the laser fused powder has been thermally affected and does not have the original properties anymore. After this assumption, the amount of powder to be refilled after each process and its relative cost are found as follows:

$$\begin{aligned} \text{Lasered Powder}(kg) \\ = (\text{Part Volume} \cdot \text{Powder Density}) + (\text{Support Volume} \cdot \text{Support Density}) \end{aligned}$$

The support volumes for the two materials have been found on Inspire® and are here reported. It is also possible to apply lightened-supports, that allow to consider a different density:

- Supports Density → 70% of the powder density
- SS 316L Support Volume → $5.248 \cdot 10^6 \text{ mm}^3$
- Ti6Al4V Support Volume → $4.976 \cdot 10^5 \text{ mm}^3$

Despite the optimized positioning of the part inside the building chamber, focusing on the support minimization it is possible to see that the volume occupied by supports is way larger than the volume of the part and so a large amount of lost material will be present.

$$\begin{aligned} \text{Refill Amount}(kg) \\ = \text{Lasered Powder}(kg) + 0,01 \cdot [\text{Powder}(kg) - \text{Lasered Powder}(kg)] \end{aligned}$$

The refill amounts for the two considered powders will be:

- SS 316L → 29.09 kg
- Ti6Al4V → 9.46 kg

$$\text{Cost}(\text{€}) = \text{Refill Amount}(kg) \cdot \text{Powder Price}(\text{€/}10kg)$$

The final cost for each optimized component produced with the two materials will be:

- SS 316L → 1253.75 €
- Ti6Al4V → 2362.21 €

From the obtained results it is possible to see that the SS 316L is the cheapest between the two and it can be selected as the final material, but if the main focus would be related to reliability and performances of the component, without taking into account the final purchasing price, the Ti6Al4V is a viable and valid choice. In particular, a consideration can be done on the Ti alloy since, even if its cost/kg is roughly six times higher than the SS 316L one, in the end thanks to the lower density and the less needed amount of supports, the component cost becomes only twice the SS 316L one.

Table 14. Optimized Parts Cost Comparison for each Material

Material	<i>SS 316L</i>	<i>Ti6Al4V</i>
Initial Volume [mm³]	$3.054 \cdot 10^6$	$3.054 \cdot 10^6$
Material Density [g/cm³]	8	4.429
Initial Weight [kg]	24	13.53
Powder Tap Density [g/cm³]	5	2.5
Optimized Volume [mm³]	$1.008 \cdot 10^6$	$4.397 \cdot 10^5$
Optimized Weight [kg]	8.06	3.48
Support Volume [mm³]	$5.248 \cdot 10^6$	$4.976 \cdot 10^5$
Support Density [g/cm³]	3.5	1.75
Powder Cost [€/10 kg]	430.99	2497.99
Powder in the Chamber [kg]	592	296
First Powder Order [€]	25514.60	73940.50
Refill Powder [kg]	29.09	9.46
Cost for Each Refill [€]	1253.75	2362.21
Weight Reduction	67%	74%

Even if the calculations are not taking into account the labour intensive activities needed to clean the final parts, they provide a clear representation of the costs to be sustained in order to produce the considered component using AM technologies. It is possible to see that, as already explained, the final choice will be pointing to SS 316L both because it provides reliable and verified components (with SF = 1.23) and because the final costs are roughly half the ones present when using Ti6Al4V powder. The main cost to be sustained for parts production, other than the one for the initial AM machine purchase, is related to the first powder order.

However, considering the selling volumes for the Tesla® Model 3, there are approximately 215000 units sold every year, with a trend that will further increase in the following years also thanks to an increasing interest towards electric cars. This makes the actual AM technologies still too expensive for high selling volumes and economies of scale.

In particular, if a traditional forming process for the rear subframe is considered, it is possible to see that, excluding the cost of the initial machine purchase, the major cost that has to be sustained is related to the fabrication of the dies (that is approximately around 40000€), that will be amortized as the production volumes increase. For what concerns the material to be purchased to produce the components, AISI 1025 can be found in the market in tubes or metal sheets, that cost approximately 5000€/ton due to the easier production process with respect to powders.

This means that, for economies of scale, at the actual state of the art, the final cost for components produced with traditional processes will be always lower than the one of parts produced with AM technologies. The condition where the trend is reversed is mostly related to small batch productions, where the cost for the fabrication of dies is not amortized, due to the too low production volumes.

It is possible to consider a graphical representation of the two different processes, providing a specific point, called Break-Even Point, that gives information on the threshold to respect to make AM technologies more convenient with respect to traditional processes. In particular, it is possible to consider the main manufacturing costs for both the production processes, listed in the table below.

Table 15. Forming vs. L-PBF Process

	Metal Forming	L-PBF
Raw Material [€/kg]	5	43.10
Component Mass [kg]	24	8.06
Supports [kg]	-	17.97
Over-material / Scraps [%]	30.00	1.00
Initial Investment [€]	40000.00	25514.60
Cost per Part [€/part]	156.18	1253.75

This means that the net final cost (without considering labour intensive activities) for a subframe developed in AM technology is roughly eight time higher than one produced with traditional processes. The difference becomes even higher if Ti alloys are considered, with a final price that is roughly fifteen times higher than the traditional one.

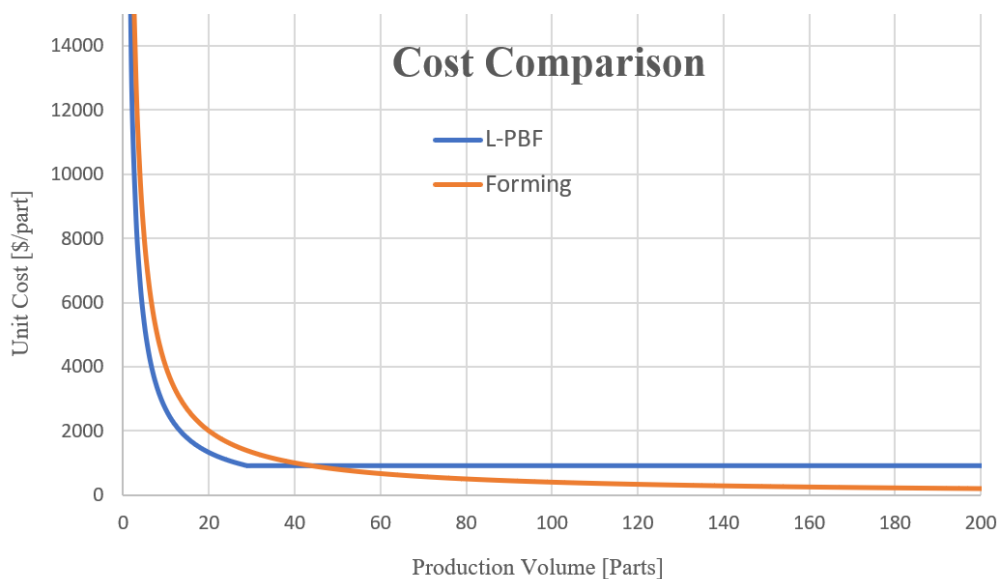


Figure 91. Cost Comparison (Forming vs. L-PBF)

From the graph, it is possible to set the Break-Even Point at around 50 units, meaning that if the production remains below that specific threshold, AM technologies are more advantageous in terms of costs, while if that threshold is overcome, traditional processes are preferable, mostly because in this case forming is able to better distribute the initial investment. Another important drawback of this specific component is also given by the fact that, due to its big dimensions, it is not possible to perform nesting operations, meaning that it will not be possible to build multiple parts at a time.

The cost breakdown analysis has been made only considering the manufacturing stage for both traditional and AM technologies without considering the labour intensive post-processing activities to be performed in the final parts, in order to provide just a rough estimation of the manufacturing costs of the single part only. In particular, the main post-processing operations to be carried out are different in the two cases.

For example, when dealing with the traditional process, it is necessary to consider hard cutting to eliminate the excessive material pinched in the blank-holder and subsequently to perform welding operations to join all the sections together. For what concerns the AM process, instead, other than the cutting operations to remove the supports, other operations in order to improve the component's surface have to be considered. Moreover, it is also possible to take into account other specific operations, such as shot peening or heat treatments, which allow to improve the mechanical performances of the final component by decreasing its residual stresses. It is evident that, in order to perform all the operations and to respect all the final geometrical tolerances and features, it is necessary to take into account the presence of a certain amount of over-material all around the part.

10. Discussion

The present work had the aim to study and evaluate the state of the art of AM technologies, applying the main DfAM and TO principles in order to check the application and the feasibility of additive manufacturing on a real component, that is the Tesla® Model 3 Dual Motor rear subframe.

The component itself had been developed in NX environment to initially build a 3D CAD model that could be imported in Altair® Inspire software to perform all the different evaluations in terms of acting loads, TO and FEM analyses both for original and optimized components. In order to consider an optimized subframe to be used in real driving scenarios, four different load cases have been analysed (i.e. acceleration, braking in capsized limits, sharp cornering and passage over a road bump).

The TO process is fundamental to additive manufacturing mostly because it allows to improve the material utilization and the performances of the components. In particular, by considering the whole subframe as a design space and applying to it all the different load cases simultaneously, it has been possible to reach an optimized configuration that allowed to eliminate all the mechanical redundancies present in the original component.

In order to perform a more complete analysis, different materials have been considered. In particular the focus fell over AISI 1025, SS 316L and Ti6Al4V, the first one used in the original component and the other two used in the optimized one. From the performed analyses, it has been possible to better evaluate the possible gains in terms of stiffness and weight reductions, with substantial differences between one material and the other. In particular, Ti6Al4V, being a lighter and stiffer material than SS 316L, provided a stiffer component characterized by a lower occupied volume and a higher weight reduction.

Going through with the FEM analyses, it has been possible to better understand where the main loads and the displacements were taking place. Specifically, since the major solicitations came from the interactions between road and ground, it was reasonable to assume that the highest stresses and displacements would have been experienced in the connection brackets between subframe and multi-link suspension rods. As a matter of fact, when analysing the results, it has been possible to see that the obtained results for each material followed an increasing trend as the stiffness increased.

In particular, the main Von Mises stresses and displacements registered in each component after each FEM analysis were all concentrated in almost the same areas, with all the parts that resulted verified:

- **AISI 1025** (Original) → $\sigma_{VM} = 184 \text{ MPa}$ → $\vartheta = 1.857 \cdot 10^{-1} \text{ mm}$ → SF = 2.01
- **SS 316L** (Optimized) → $\sigma_{VM} = 467 \text{ MPa}$ → $\vartheta = 4.196 \cdot 10^{-1} \text{ mm}$ → SF = 1.23
- **Ti6Al4V** (Optimized) → $\sigma_{VM} = 502 \text{ MPa}$ → $\vartheta = 4.413 \cdot 10^{-1} \text{ mm}$ → SF = 1.65

From what can be seen from the previously indicated results, it is possible to select the SS 316L material as the definitive one for the studied component. Specifically, the use of stainless steel applied to DfAM principles allowed to obtain an optimized component with improved performances and lower volume ($1.008 \cdot 10^6 \text{ mm}^3$), that also resulted in a 64% weight reduction with the final optimized component weighing 8.06 kg. Moreover, the FEM analysis results can be further improved by using finer meshes and the final components can be subjected to post-processing (heat treatments or shot-peening) to increase their mechanical strength.

Once all the TO and FEM analyses have been performed and the results are satisfactory, it is possible to proceed to the simulation for the 3D printing process, in this specific case conducted with L-PBF technology using SS 316L powder. The considered part has been initially sliced in three different regions, that are the ones related to the lateral arcs and the middle part made up of the horizontal beams, connecting the other two extremities. As the sliced sections have been defined, it is possible to proceed to the printer definition in Altair® environment, with the selected machine being the Laser XLINE 2000R by General Electrics® and a building envelope of dimensions 800 x 400 x 500 mm.

The orientation for the lateral sections inside the chamber is performed considering the specific *Optimize Orientation* tool present in the Altair® toolbar. The result of this operation provides an optimized configuration with $X = 90^\circ$ and $Y = 180^\circ$, with the component that will be sustained by lightened supports having a volume of $5.135 \cdot 10^6 \text{ mm}^3$, density equal to 70% to the powder one and a final printing time of 64 hours and 9 minutes.

As soon as the printing simulation is ended, it is possible to analyse the FEM results for the evolution of the thermal and mechanical stresses as the layers of material are deposited one over the other in order to build the final part. In particular, the final FEM results showed lateral component's sections that will be characterized by sufficient strength and accuracy, since they provide Von Mises stresses and displacements during the printing process that are in the range of 127 MPa and $3.102 \cdot 10^{-1} \text{ mm}$.

After successfully satisfying the mechanical and thermal requirements for the printing process, it is possible to check the actual process feasibility by performing a cost breakdown analysis for all the parts built following the studied AM technology and comparing it to traditional forming processes. In particular, from the performed calculations it can be highlighted that the highest cost is related to the first powder order, that is comparable to the purchasing cost for a specific die in a traditional processes (25514€ vs. 40000€). It has to be also remarked that all the calculations are not taking into account the initial machine investment and the labour intensive activities needed to remove the supports.

From the cost breakdown analysis it is possible to better understand the major constraint of AM technologies, that is the production cost. In particular, the final products in SS 316L and Ti6Al4V result roughly eight and fifteen times more expensive than the one produced with traditional processes, respectively. This is mainly due to the fact that traditional processes are able to sustain a much higher production rate, making it possible to decrease by far the cycle time for each component, making a higher number of components able to satisfy the actual selling demands (215000 units/year). The higher production rates, combined with a lower cost for the raw materials (AISI 1025 provided in tubes or sheets), allow to better amortize the machine and die purchasing cost.

As a consequence, the actual state of the art of AM technologies doesn't make them suitable for economies of scale, or at least for large production batches. As a matter of fact, these technologies are providing actual improvements only when applied to small production lots that can be related to on-demand components or niche markets, such as the supercar ones. Taking into account these specific sectors, AM is able to provide major advantages in terms of costs and performances thanks to an overall performance improvement (weight reductions), lower costs with respect to traditional processes (since the lower the number of produced parts and the worse the amortization of the initial machine investment) and lower lead times (virtual simulation that avoids the prototyping stage).

However, the obtained results are quite encouraging, mostly because of the high potential of AM processes in the future and because of the extremely high gains that can be found in the automotive industry. In particular, focusing on the presented work and extending it on other vehicles each one characterized by several structural components, it is possible to obtain sensible weight savings that can result in lower fuel consumptions, lower emissions and an overall improvement in the environmental impact of any vehicle.

In particular, the adoption of AM technologies can be considered in several structural components in order to have a better evaluation of what the main gains could be in terms of savings and vehicle autonomy. Considering, for example, the weight distribution of each specific family of components in a Tesla®, it is possible to highlight the actual percentage of structural components that can be manufactured following AM technologies and to evaluate the actual decrease in vehicle mass.

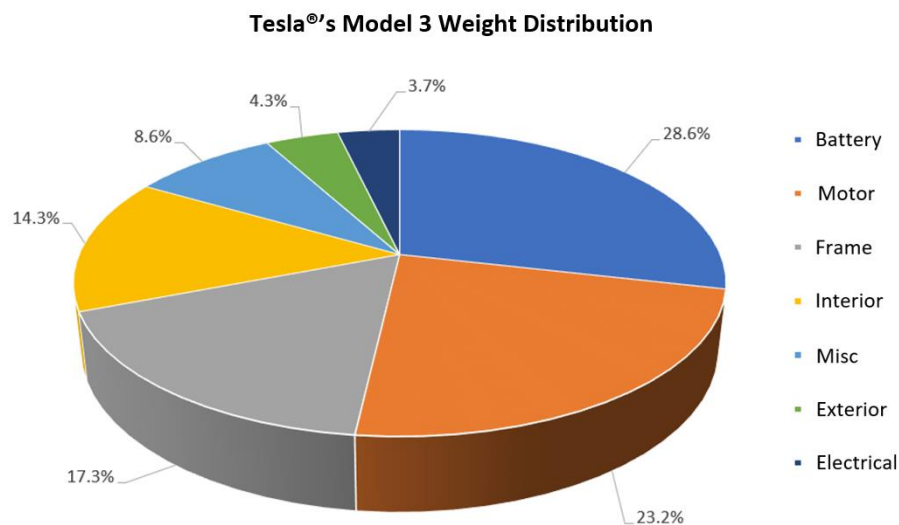


Figure 92. Tesla®'s Model 3 Dual Motor Weight Distribution

From the previous chart, it is possible to consider that, according to the proposed study, the main category subjected to AM processes could be the *Frame* one, that takes into account all the structural components placed in the vehicle underbody, from battery housings to subframes. This specific category is accounting for 17.3% of the overall car weight meaning that, if a similar approach to the rear subframe one is applied to each structural component (with a consequent weight reduction in the order of 67%), the final weight saving for the whole vehicle will be in the range of 12% that can be considered as a very satisfactory results.

In particular, this 12% weight reduction can be translated into a decrease in weight of about 220 kg, which can decrease the weight of the Model 3 from 1819 kg to around 1600 kg. This is a fundamental result because this weight reduction will make it possible to increase by far the vehicle autonomy, that nowadays is a major constraint for electric cars. Specifically, thanks to a lighter vehicle, the actual energy required to move the car itself will be lower and the battery pack will be subjected to a decreased energy demand, resulting in a longer covered distance. On the other hand, it will be also possible to consider a bigger battery pack with respect to the one actually implemented, so that the vehicle weight remains the same but the autonomy can be further increased. In either cases, the result will be the same and pointing towards an increased driving range.

Considering everything said before, it is evident that, for fixed battery pack dimensions, if the vehicle is lighter and the driving range is higher, the amount of energy required to charge the vehicle remains the same, but the actual interval of time between each charging operation increases, decreasing the overall number of needed recharges over the year. From Tesla®'s specifications, the battery pack is able to guarantee a driving autonomy of 524 km and it has to be substituted after 800'000 km, meaning that it is able to sustain around 1500 complete charge-discharge cycles over its operating life. The considered weight reduction will make it possible to have an increase in the driving range of about 8.5%, meaning that the vehicle will be able to cover a distance of about 578 km, decreasing the actual amount of charging operations down to 1300 complete charge-discharge cycles over the 800'000 km threshold, with a 15% decrease in recharging operations.

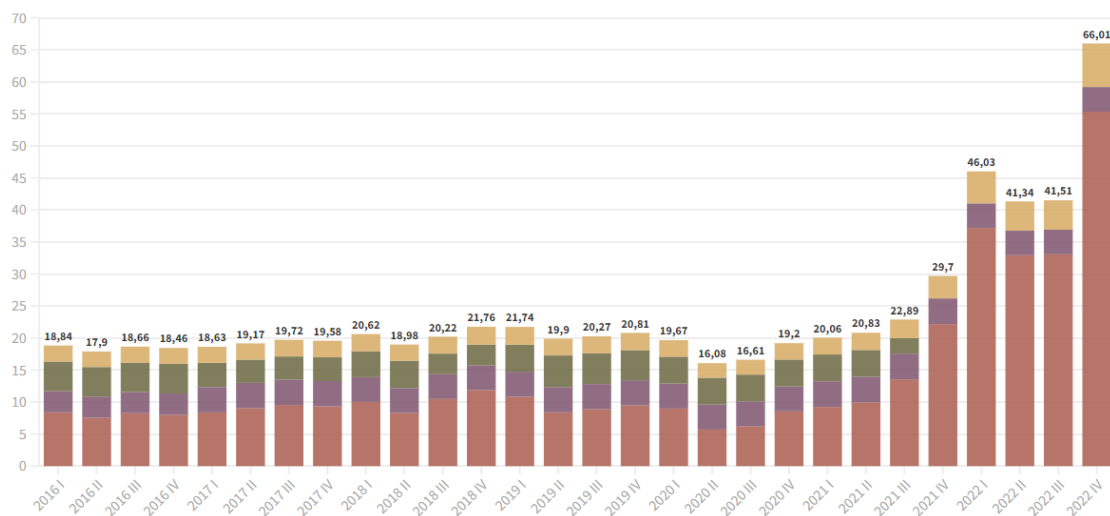


Figure 93. Energy Cost Variation (2016 - 2022)^[21]

All these data will be translated into savings not only from a weight point of view, but also from an economic point of view, especially for the end user. In particular, considering the average energy costs to recharge a vehicle from the public grid in the last seven years, they are around 0.24 €/kWh with an overall expense of about 19.5€ to completely charge the Model 3, meaning that the actual expense over the whole battery pack operating life (800'000 km) is of about 29'250€. Considering the new vehicle, for a fixed energy cost and a fixed battery pack, the final recharge expense over its whole operating life (800'000 km) would be in the range of 25'350 €, with a 13% cost saving, corresponding roughly to 4000€.

It has also to be noticed that, considering the optimized vehicle, the amount of recharging operations will be highly decreased, while the consumed amounts of energy for each recharge do not evidently separate from the ones sustained with the actual vehicle. This means that, considering any energy provider, it will be possible to decrease the amount of produced energy thanks to a decreased demand in terms of recharging operations. This trend will then have also beneficial impacts in terms of carbon footprint and LCA for any electric vehicle, not from a TTW (Tank-To-Wheel) point of view, but from a WTT (Well-To-Tank) one. Moreover, the actual decrease of used material will make it also possible to decrease the amount of scraps.

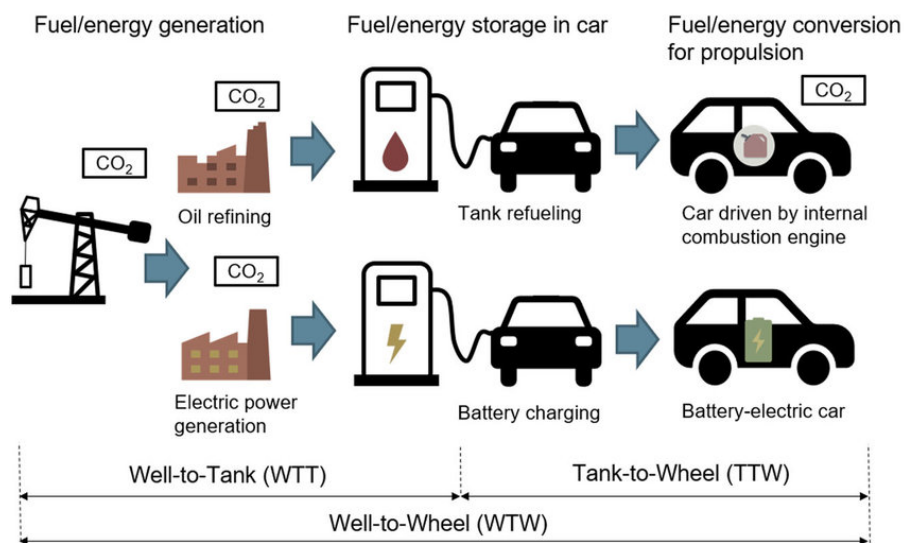


Figure 94. WTT & TTW Emissions

Further studies and developments to this project can be related to the evaluation of the NVH (Noise, Vibration, Harshness) performances of the vehicle, that could be improved thanks to part consolidation that can decrease the actual part count. This aspect, combined to the possibility to have more robust joints between one part and the other, can decrease the actual vibrations transmitted to the vehicle chassis and improve the vehicle riding comfort thanks to a more solid and stiffer frame.

All this considerations, will make it evident that the actual costs for the AM technology deployment are still high, but the gains and the potential savings in terms of weight, scraps and money can become one of the main drivers for the adoption of this technology, with the benefits that can overcome by far the main disadvantages, especially if new studies can be performed in the future that will make it possible to use AM technologies for economies of scale, allowing to better amortize the machine and the raw material costs. The gains related to AM processes in terms of productivity and costs will be even higher if the actual materials implemented in these processes would have had a final purchasing price comparable to the ones used in traditional processes.

Bibliography

- [1] Thompson, M. K., Moroni, G., Vaneker, T., Fadel, G., Campbell, R. I., Gibson, I., ... & Martina, F. (2016). *Design for Additive Manufacturing: Trends, opportunities, considerations, and constraints*. *CIRP annals*, 65(2), 737-760.
- [2] Wiberg, A., Persson, J., & Ölvander, J. (2019). *Design for additive manufacturing a review of available design methods and software*. *Rapid Prototyping Journal*.
- [3] Selvaraj, P., Radhakrishnan, P., & Adithan, M. (2009). *An integrated approach to design for manufacturing and assembly based on reduction of product development time and cost*. *The International Journal of Advanced Manufacturing Technology*, 42(1), 13-29.
- [4] Krish, S. (2011). *A practical generative design method*. *Computer-Aided Design*, 43(1), 88-100.
- [5] Briard, T., Segonds, F., & Zamariola, N. (2020). *G-DfAM: a methodological proposal of generative design for additive manufacturing in the automotive industry*. *International Journal on Interactive Design and Manufacturing (IJIDeM)*, 14(3), 875-886.
- [6] Sigmund, O., & Maute, K. (2013). *Topology optimization approaches*. *Structural and Multidisciplinary Optimization*, 48(6), 1031-1055.
- [7] Atzeni, E., & Salmi, A. (2021). *Lecture 04-Design for AM*, 26-38.
- [8] Nie, Z., Jung, S., Kara, L. B., & Whitefoot, K. S. (2020). *Optimization of part consolidation for minimum production costs and time using additive manufacturing*. *Journal of Mechanical Design*, 142(7).
- [9] Yang, S., Tang, Y., & Zhao, Y. F. (2015). *A new part consolidation method to embrace the design freedom of additive manufacturing*. *Journal of Manufacturing Processes*, 20, 444-449.
- [10] Schmelzle, J., Kline, E. V., Dickman, C. J., Reutzel, E. W., Jones, G., & Simpson, T. W. (2015). *(Re)Designing for part consolidation: understanding the challenges of metal additive manufacturing*. *Journal of Mechanical Design*, 137(11).
- [11] Giffi, C. A., Gangula, B., & Illinda, P. (2014). *3D opportunity in the automotive industry. Additive manufacturing hits the road: Deloitte University Press*, 24.
- [12] Leal, R., Barreiros, F. M., Alves, L., Romeiro, F., Vasco, J. C., Santos, M., & Marto, C. (2017). *Additive manufacturing tooling for the automotive industry*. *The International Journal of Advanced Manufacturing Technology*, 92(5), 1671-1676.

- [13] Böckin, D., & Tillman, A. M. (2019). *Environmental assessment of additive manufacturing in the automotive industry*. *Journal of Cleaner Production*, 226, 977-987.
- [14] Vasco, J. C. (2021). *Additive manufacturing for the automotive industry*. In *Additive Manufacturing* (pp. 505-530). Elsevier.
- [15] Dalpadulo, E., Pini, F., & Leali, F. (2020). *Integrated CAD platform approach for Design for Additive Manufacturing of high performance automotive components*. *International Journal on Interactive Design and Manufacturing (IJIDeM)*, 14(3), 899-909.
- [16] Sarvankar, S. G., & Yewale, S. N. (2019). *Additive manufacturing in automobile industry*. *Int. J. Res. Aeronaut. Mech. Eng*, 7(4), 1-10.
- [17] <https://www.makepartsfast.com/the-advantages-of-additive-manufacturing-in-the-automotive-industry/>
- [18] <https://www.unleashedsoftware.com/blog/12-benefits-of-additive-manufacturing-and-5-disadvantages>
- [19] Rawlinson, P. D., & Gadhiya, H. L. (2013). U.S. Patent No. 8,424,960. Washington, DC: U.S. Patent and Trademark Office.
- [20] Flynn, J. M., Shokrani, A., Newman, S. T., & Dhokia, V. (2016). *Hybrid additive and subtractive machine tools—Research and industrial developments*. *International Journal of Machine Tools and Manufacture*, 101, 79-101.
- [21] <https://www.arera.it/it/dati/eep35.htm>